CORA Cork Open Research Archive
Cartlann Taighde Oscailte Chorcaí

Title	Correlations in low dimensional quantum systems
Authors	Fogarty, Thomás
Publication date	2013
Original Citation	Fogarty, T. 2013. Correlations in low dimensional quantum systems. PhD Thesis, University College Cork.
Type of publication	Doctoral thesis
Rights	© 2013, Thomás Fogarty - http://creativecommons.org/licenses/by-nc-nd/3.0/
Download date	2026-11-06 08:00:09
Item downloaded from	https://hdl.handle.net/10468/1293



UCC
University College Cork, Ireland
Coláiste na hOllscoile Corcaigh

UNIVERSITY COLLEGE CORK

Correlations in Low Dimensional Quantum Systems

by

Thomás Fogarty

A thesis submitted in partial fulfillment for the
degree of Doctor of Philosophy

in the
Faculty of Science
Department of Physics

August 2013

Declaration of Authorship

I, Thomás Fogarty, declare that this thesis titled, 'Correlations in Low Dimensional Quantum Systems', and the work presented in it are my own. I confirm that:

- This work was done wholly or mainly while in candidature for a research degree at this University.
- Where any part of this thesis has previously been submitted for a degree or any other qualification at this University or any other institution, this has been clearly stated.
- Where I have consulted the published work of others, this is always clearly attributed.
- Where I have quoted from the work of others, the source is always given. With the exception of such quotations, this thesis is entirely my own work.
- I have acknowledged all main sources of help.
- Where the thesis is based on work done by myself jointly with others, I have made clear exactly what was done by others and what I have contributed myself.

Signed: _____

Date: _____

External Examiner
Dr. Anna Minguzzi - Université Grenoble-Alpes and CNRS, France

Internal Examiner
Prof. Eoin O'Reilly - University College Cork, Ireland

Principle Supervisor
Prof. Thomas Busch - Okinawa Institute of Science and Technology, Japan

Secondary Supervisor
Dr. Andreas Ruschhaupt - University College Cork, Ireland

Without tooting my own horn - I think it's a masterpiece.

Nicolas Cage

UNIVERSITY COLLEGE CORK

Abstract

Faculty of Science
Department of Physics

Doctor of Philosophy

by Thomás Fogarty

In this thesis I present the work done during my PhD in the area of low dimensional quantum gases. The chapters of this thesis are self contained and represent individual projects which have been peer reviewed and accepted for publication in respected international journals. Various systems are considered, the first of which is a two particle model which possesses an exact analytical solution. I investigate the non-classical correlations that exist between the particles as a function of the tunable properties of the system. In the second work I consider the coherences and out of equilibrium dynamics of a one-dimensional Tonks-Girardeau gas. I show how the coherence of the gas can be inferred from various properties of the reduced state and how this may be observed in experiments. I then present a model which can be used to probe a one-dimensional Fermi gas by performing a measurement on an impurity which interacts with the gas. I show how this system can be used to observe the so-called orthogonality catastrophe using modern interferometry techniques. In the next chapter I present a simple scheme to create superposition states of particles with special emphasis on the NOON state. I explore the effect of inter-particle interactions in the process and then characterise the usefulness of these states for interferometry. Finally I present my contribution to a project on long distance entanglement generation in ion chains. I show how carefully tuning the environment can create *decoherence-free subspaces* which allows one to create and preserve entanglement.

Acknowledgements

Firstly I would like to thank my parents, Madge and Joe, for all their support during my lengthy education. I was told by a wise man that the title of 'Dr' means the most to your mother, so now I hope she is happy and has some idea of what I was doing during my PhD. Thanks also to my brother Shane for his encouragement and being the practical one in our family.

I would like to thank everyone who graced the hallowed desks of room 202 in the Kane building over the years including Suzanne McEndoo, Brian O'Sullivan, Tara Hennessy, Nicola Lo Gullo, Jérémie Gillet, Gianluca Giorgi, Miguel Angel García-March, Ricard Menchón, Chandrashekar Madaiah, Ciaran Phelan, Carlo Di Franco, Bryan Dalton, Mark Kennedy and Anthony Kiely. Many scones were eaten and coffees drank, and some physics was done too.

I sincerely thank John Goold for his help and advice during my PhD and for all the work we did together. He possesses an almost boundless optimism and love for physics which set the basis for productive arguments which really helped me become the researcher I am today. Thanks to Dave Rea who taught me a lot through his enthusiasm and passion for physics, his presence in the office always put a smile on my face in the corner of room 202.

I want to thank some of my closest friends in office over the years, Tadhg Morgan, Lee O'Riordan and Steve Campbell. Tadhg, we started our PhDs together and I like to think we drove each other to become better scientists over long discussions and Nic Cage movies. Lee, your mantra of "Ah sure it'll be grand" kept me calm through this process and I hope the next time we meet you will still have functioning feet. Steve, you were my coach both in terms of academia and fitness, your advice and friendship were indispensable in and out of the office. The temple is still in progress.

Thanks to my close friends and former housemates Padraic Morrissey, Dave O'Brien and Pádraig Brick whose friendship have been invaluable over the last few years. We started out together eight years ago in G7 and you were always there for pints at the end of long days and at the beginning of long nights.

I would especially like to thank my non-physics friends who I could count on to help me relax and forget about my PhD in their company. Katie O'Sullivan, Alan Corbett, Whiney, Colm Ryan, Liam Heneghan, Paul Horan and Aisling Moore thanks for the banter and happy memories. Also I would like to express the deepest appreciation to Peter Hession for the ritual act of dancey dancey.

For making my stay in Saarbrucken a joyful experience I would like to thank Bruno Taketani, Endre Kajari, Mauricio Torres, Oxanna Mishina, Cecilia Cormick and Jose Brito.

I was greatly appreciative of my time in Okinawa and there are many people I will miss there. Special thanks to Sawako Koki for keeping my mind off work and always being available for cups of tea.

I would like to thank all my collaborators especially Mauro Paternostro and Giovanna Morigi for their help and the time they spent on our work together.

Most importantly I would like to thank Thomas Busch, who has expertly guided my academic career for the last four years. Due to his legendary attention to detail and his skills at "massaging" the text, the work you see in this thesis could not have been accomplished. I could only ever wish that I would someday match his passion and dedication to research and I will forever be grateful to him.

Finally I would like to thank the Irish Research Council for funding through the Embark Initiative under grant RS/2009/1082 and the Okinawa Institute for Science and Technology Graduate University for their support.

Contents

Declaration of Authorship i

Abstract iii

Acknowledgements iv

1 Introduction 1
- 1.1 Ultracold gases . . . 3
  - 1.1.1 Indistinguishable Particles . . . 3
  - 1.1.2 Fermions . . . 4
  - 1.1.3 Bosons . . . 4
- 1.2 Optical Trapping . . . 5
  - 1.2.1 Optical Lattices . . . 6
  - 1.2.2 Low Dimensional Quantum Gases . . . 6
  - 1.2.3 Point-like Interactions . . . 7
- 1.3 Degenerate Fermi Gas . . . 8
- 1.4 The Tonks-Girardeau Gas . . . 9
  - 1.4.1 First Experimental Observation . . . 10
- 1.5 Reduced single particle density matrix . . . 11
- 1.6 Summary of work done in the thesis . . . 13
  - 1.6.1 Chapter 2 . . . 13
  - 1.6.2 Chapter 3 . . . 13
  - 1.6.3 Chapter 4 . . . 14
  - 1.6.4 Chapter 5 . . . 14
  - 1.6.5 Chapter 6 . . . 15

2 Entanglement and non-locality between two interacting atoms 16
- 2.1 Introduction . . . 16
  - 2.1.1 Shannon Entropy . . . 17
  - 2.1.2 Von Neumann Entropy . . . 17
  - 2.1.3 Non-locality and the CHSH inequality . . . 19
- 2.2 Model Hamiltonian . . . 21
- 2.3 Entanglement . . . 25
- 2.4 Calculation of the Wigner function and assessment of its negativity . . . 27

2.4.1 Negative volume of the Wigner function . . . 31
2.5 Testing non-locality in phase space . . . 32
2.5.1 Finite Temperature . . . 33
2.5.2 Detection Scheme . . . 34
2.6 Effects of dissipation . . . 35
2.7 Conclusions . . . 37
2.8 Outlook . . . 38

3 Coherence and dynamics of a Tonks-Girardeau gas 39
3.1 Introduction . . . 39
3.2 The Tonks-Girardeau gas . . . 40
3.2.1 Single particle solutions . . . 41
3.3 Static and Dynamic Properties . . . 43
3.3.1 Single Particle Density Profile . . . 43
3.3.2 Energy profile . . . 46
3.3.3 Reduced single particle density matrix . . . 47
3.3.4 Natural orbitals . . . 49
3.3.5 Momentum distribution . . . 50
3.4 Free expansion . . . 53
3.5 Conclusions . . . 53
3.6 Outlook . . . 54

4 The orthogonality catastrophe in a Fermi gas 55
4.1 Introduction . . . 55
4.1.1 Orthogonality Catastrophe . . . 56
4.1.1.1 Time independent case . . . 56
4.1.1.2 Time dependent case . . . 58
4.2 Loschmidt Echo . . . 59
4.3 Impurity in an Harmonic Trap . . . 60
4.3.1 Finite sized impurity . . . 63
4.4 System and Environment Model . . . 65
4.5 Entanglement . . . 67
4.6 Detection . . . 68
4.7 Finite Temperature . . . 70
4.8 Conclusions . . . 73
4.9 Outlook . . . 73

5 Effect of interparticle interaction in a free-oscillation atomic interferometer 74
5.1 Introduction . . . 74
5.1.1 Quantum Fisher Information . . . 75
5.1.2 Von Neumann Entropy . . . 78
5.2 Preliminaries . . . 78
5.2.1 The Model . . . 78
5.2.2 Discrete Variable Representation (DVR) . . . 81
5.2.3 Time Evolution . . . 82
5.3 Analysis of different interaction regimes . . . 83

5.3.1 Attractive Interactions . . . 83
5.3.1.1 Scattering A . . . 83
5.3.1.2 Scattering B . . . 84
5.3.2 Repulsive Interactions . . . 87
5.3.2.1 Scattering A . . . 87
5.3.2.2 Scattering B . . . 87
5.3.3 Case $\epsilon = 1$ . . . 88
5.4 Experimental Realization . . . 90
5.5 Conclusions . . . 90
5.6 Outlook . . . 91

6 Long distance entanglement in a linear ion chain 92
6.1 Introduction . . . 92
6.2 Model . . . 94
6.2.1 Initial state preparation . . . 97
6.2.2 Coupling of transverse and axial directions . . . 99
6.2.3 Dynamics . . . 100
6.2.4 Spectral Density . . . 100
6.3 Entanglement generation in a short ion chain . . . 103
6.4 Entanglement generation in a long ion chain . . . 104
6.5 Conclusions . . . 106
6.6 Outlook . . . 107

7 Conclusions and Outlook 108
7.1 Entanglement and non-locality between two interacting atoms . . . 108
7.2 Coherence and dynamics of a Tonks-Girardeau gas . . . 109
7.3 The orthogonality catastrophe in a Fermi gas . . . 110
7.4 Effect of interparticle interaction in a free-oscillation atomic interferometer 111
7.5 Long distance entanglement in a linear ion chain . . . 111

Bibliography 113

Chapter 1

Introduction

As the length scales we explore stretch from to the stars to atomic particles the different worlds we encounter are as varied and exciting as anything imagined through science fiction. The journey to the microscopic realm has especially brought new insights into the building blocks of nature through our encounters with the intriguing phenomena which exist at small length scales. This *quantum* world has as much an attraction to the public as it does to physicists, due to its strange dichotomies which speak of a fascinating land, that exists but is imperceptible in our macro-world. It raises the question of reality, not only physically but also philosophically, and has enthralled and confused in equal measure.

It was Albert Einstein's seminal work in 1905 on the photoelectric effect that introduced this radical new perception of nature [1]. Einstein said that a light wave of frequency ν could be described as a localised packet, or *quantum*, of energy E through the simple relation

$$E = h\nu \ , \tag{1.1}$$

in essence a wave can act like a particle. Named after Max Planck, the constant h is the *quantum* of action and has the very small value of 6.626×10^{-34} J·s [2]. Its existence is profound and means that physical action cannot take on any indiscriminate value but instead must be a multiple of Planck's constant.

If light waves could be described as particles with a well defined energy could matter be described as a wave? This question was answered in 1924 by Louis de Broglie, who defined the eponymous wavelength of a particle as

$$\lambda_{dB} = \frac{h}{p}. \tag{1.2}$$

De Broglie's wavelength depends on the momentum of the particles p, which if very large leads to a vanishingly small wavelength and the reason why the wave-nature of particles is not seen in our macroscopic world [3]. Reducing the momentum of a gas will increase its average de Broglie wavelength which can be defined in terms of the mean velocity of the particles in the gas

$$\langle \lambda_{dB} \rangle = \sqrt{\frac{h^2}{2\pi m k_B T}} \,, \tag{1.3}$$

where T is its temperature and k_B is Boltzmann's constant. Therefore as the gas approaches absolute zero the de Broglie wavelengths of the individual particles increase. If these wavelengths become larger than the average interparticle distance and begin to overlap, individual particles cannot be told apart. In this domain the classical description of the gas fails and one must treat it as a quantum object which can exhibit different wave phenomena.

An exciting world lay just out of reach as different laboratories around the world improved confining and laser cooling of atomic gases as the trapping and manipulation of cold gases offers great flexibility in creating new quantum states. Atoms can be trapped using magnetic fields which exploit the Zeeman splitting of their energy levels and by using optical fields which induce a dipole moment on the atoms to create a non-zero force. In recent years the state of the art in atom trapping allows one to localise small ensembles of particles in single traps or optical lattices [4, 5]. It is no surprise that this ability to create clean periodic systems, devoid of defects or thermal phonons, has generated a lot of interest in simulating condensed matter phenomena [6]. Reducing the dimensionality of these systems can lead to the creation of strongly correlated gases, such as the Tonks-Girardeau gas of hard core bosons [7, 8, 10]. These lower dimensional systems have manifestly different physics than their three dimensional counterparts and provide an exciting testbed for strongly interacting many-body physics. The ability to isolate single particles [11, 12] which can be manipulated with an incredible degree of control has afforded us the possibility to accurately study fundamental quantum correlations. These ideal systems allow one to explore concepts in quantum information theory such as entanglement and non-locality which have long been heralded as resources for future quantum technologies [13, 14].

The recent experimental advances mentioned above have taken the quantum world from theory to practicality in what is an exciting time to be in this field. As current technologies strive to reach smaller and smaller length scales the need for truly quantum technologies will become essential, the most high profile being the quantum computer[15–17]. However I feel this should not overshadow the work that is being done which explores fundamental physics, as the ability is now available to truly probe and understand the quantum world and all its *spooky* origins.

In the rest of this chapter I will introduce some core concepts of ultracold physics that will be assumed throughout this thesis, and then I will discuss some recent experiments which make low-dimensional physics accessible.

1.1 Ultracold gases

1.1.1 Indistinguishable Particles

In classical physics identical and individual particles can be easily labelled and distinguished, however this is not the case with quantum particles. At low temperatures when the wavefunctions of the particles spread out and overlap an exchange of particles cannot be detected, as the individual ones are identical and nothing sets them apart. This is because in quantum mechanics particles only have a finite set of properties, and if they are the same for all the particles in question there is no way to label and distinguish them.

Lets us consider a state of two indistinguishable particles, $\psi_1(x)$ and $\psi_2(y)$. The density of their two-body state $|\Psi(x,y)|^2 = |\Psi(y,x)|^2$ must stay the same under particle exchange. The way to achieve this is through a *symmetric* or *antisymmetric* permutation over all combinations of the single particle states, in this way $\Psi(x,y)$ is written as

$$\Psi(x,y) = \sum_{x,y} A(x,y)\psi_1(x)\psi_2(y) \ , \tag{1.4}$$

where $A(x,y)$ is the permutation operator. If the wavefunction is *symmetric* under particle exchange, $A(x,y) = A(y,x)$, the two-body wavefunction is

$$\Psi(x,y) = \frac{1}{\sqrt{2}} \left(\psi_1(x)\psi_2(y) + \psi_1(y)\psi_2(x)\right) \ , \tag{1.5}$$

and if the wavefunction is *antisymmetric* under particle exchange, $A(x,y) = -A(y,x)$, the two-body wavefunction is

$$\Psi(x,y) = \frac{1}{\sqrt{2}} \left(\psi_1(x)\psi_2(y) - \psi_1(y)\psi_2(x)\right) \ . \tag{1.6}$$

This means every time we exchange particles located at x and y the sign of the wavefunction changes, $\Psi(x,y) = -\Psi(y,x)$.

The spin-statistics theorem relates the exchange symmetry of identical particles to their spin, or intrinsic angular momentum. It states that *fermions* possess *antisymmetric* wavefunctions and have half-integer spin, while *bosons* possess *symmetric* wavefunctions and have integer spin [18].

1.1.2 Fermions

Fermions, named after Enrico Fermi, are particles such as electrons or quarks, or composite particles such as Lithium-6, with half integer spin. It is easy to see that the antisymmetric wavefunction Eq. (1.6) vanishes when two indistinguishable particles are in the same state at the same time. This is known as Pauli's exclusion principle. Based on this principle Fermi-Dirac statistics was formulated which describes the statistical behaviour of a gas of identical non-interacting fermions where the average number of fermions in a single particle state of energy ϵ_i is given by

$$\bar{n}_i = \frac{1}{e^{\frac{\epsilon_i - \mu}{k_B T}} + 1}\,, \tag{1.7}$$

where T is the temperature, k_B is Boltzmann's constant and μ is the chemical potential [19, 20]. Due to Pauli's exclusion principle only a maximum of one identical fermion can occupy each energy level so $0 \leq \bar{n}_i \leq 1$. At sufficiently low temperatures every energy state is occupied by one non-interacting fermion up to the Fermi level which is the energy of the highest excited occupied state. This is known as the Fermi sea. The Fermi-Dirac statistics helps us describe everything from electrons in metals to the collapse of stars.

1.1.3 Bosons

Bosons have integer spin and multiple bosons are allowed to occupy the same state at the same time. Bosons obey Bose-Einstein statistics which was first derived by Satyendra Nath Bose in 1924, who sought to describe the statistics of light quanta, and was later generalised by Albert Einstein to describe atoms. The Bose-Einstein distribution is given by

$$\bar{n}_i = \frac{1}{e^{\frac{\epsilon_i - \mu}{k_B T}} - 1}\,, \tag{1.8}$$

and one of its predictions is that non-interacting bosons will undergo a phase transition at finite temperature and macroscopically occupy their ground state. This *condensation* of the bosons into a common ground state is know as Bose-Einstein condensation and the resulting state as a Bose-Einstein condensate (BEC). To achieve a BEC a gas of bosons must be sufficiently cold so that the associated thermal de Broglie wavelength of the particles Eq.(1.3) becomes larger than the average interparticle distance. At this point the individual particle wavefunctions begin to overlap and it is not possible to distinguish individual particles. A condensate is a truly macroscopic quantum state consisting of degenerate single particle states.

The first BECs were experimentally created in 1995 by the groups of E. Cornell and C. Wieman at NIST and W. Ketterle in MIT [21, 22]. Both teams used alkali atoms of ^{87}Rb and ^{23}Na respectively and cooled them to around 170nK. Since then many other species have been condensed [23] and a large amount of fundamental physics has been explored (wave-particle duality, superfluidity, quantized vortices, matter-wave solitons, slow light to name only a few) [24–29] and connections to many other areas of physics have been found (simulation of condensed matter phenomena, Mott insulator and other phase transitions, frustrated magnets, measuring gravitational waves and modelling black holes) [5, 30–34].

1.2 Optical Trapping

When a neutral atom is under the influence of an external electric field it acquires an electric dipole. This allows the atom to interact with the field and its interaction can be described in the dipole approximation by

$$U(x,t) = -\mu \mathbf{E}(x,t) \,, \tag{1.9}$$

where μ is the dipole moment operator of the atom and $\mathbf{E}(x,t)$ is the electric field of the laser [35]. In the case of an off-resonant laser beam the interaction produces a shift in energy which is referred to as the AC Stark shift. This forms a conservative potential acting on the atom which depends on the laser intensity and is given by

$$V(x) = -\frac{1}{2}\alpha(\omega)|\overline{\mathbf{E}(x,t)}|^2 \,, \tag{1.10}$$

where $\overline{\mathbf{E}(x,t)}$ is the time average of the electric field and $\alpha(\omega)$ is the second order contribution to the dipole moment.

An advantage of optical trapping over magnetic trapping is that the potential experienced by the atoms in their ground state is independent of its magnetic component and this can allow trapping of atoms with different magnetic states in the same trap. Due to the high level of versatility that laser sources exhibit today a variety of different trap geometries can be created, including tightly confined pancake and cigar shaped traps [36, 37].

The optical trap also allows the ability to add an external magnetic field which can be used to tune the interaction between atoms. This relies on the existence of Feshbach resonances which occur when the energy of a bound state of an interatomic potential is equal to the kinetic energy of a colliding pair of atoms, causing an avoided crossing in

the scattering spectrum [38] . As the scattering length between two atoms is energy dependent different interaction regimes can be explored from attractive dimers to strongly repulsive particles.

1.2.1 Optical Lattices

Optical lattices are created from two counter-propagating laser beams described by their electric field components $\mathbf{E}(x,t) = E_0 e^{\pm i k_x x}$, where E_0 is the amplitude and k_x is the associated wavevector [5, 39]. The two beams interfere and create an optical potential of the form $V(x) = V_x \cos^2(k_x x)$, and by adding two extra pair of beams in the y and z direction a three dimensional periodic potential can be created of the form

$$V(x,y,z) = V_x \cos^2(k_x x) + V_y \cos^2(k_y y) + V_z \cos^2(k_z z)\,. \tag{1.11}$$

These different beams in the x, y and z directions must be distinguishable (e.g. different polarisations or slightly different wavelengths) in order to prevent interference between them. Such a potential is periodic in space and is capable of trapping atoms at the nodes or antinodes depending on the sign of the detuning. If the light is red detuned (its frequency is smaller than the atomic transition frequency) then the atoms will be trapped at the maxima of the optical lattice, if it is blue detuned (its frequency is larger than the atomic transition frequency) then the atoms will be trapped at the minima.

Optical lattices are periodic potentials which can trap single atoms in large arrays and are used as simulators for condensed matter models. This is due to the ability to manipulate the periodicity by adjusting the angle at which the laser beams meet, and dimensionality of the system by tuning the depth of the lattice wells through the individual laser intensities [40]. It is in this way that low dimensional quantum gases can be realised.

1.2.2 Low Dimensional Quantum Gases

To restrict atoms to propagate along one spatial direction only, control over the external degrees of freedom of cold gases is needed. This allows us to create trapping geometries to explore phenomena in a system which is quite different from the three dimensional case [41, 42]. Let us consider atoms of mass m trapped in three spatial directions in a harmonic potential given by

$$V(x,y,z) = \frac{1}{2} m \left(\omega_x^2 x^2 + \omega_y^2 y^2 + \omega_z^2 z^2\right)\,, \tag{1.12}$$

If we choose the x-axis as the axial direction ($\omega_A = \omega_x$) that will define our new one-dimensional geometry, we want to freeze out oscillations in the transverse directions ($\omega_T = \omega_y, \omega_z$). To ensure this we must tighten the trap along the transverse directions so that $\omega_A \ll \omega_T$. This ensures that the transverse energy level spacing $\hbar\omega_T$ increases which makes it more difficult for the atoms to gain enough energy to occupy any higher energy states in these directions. As long as $k_B T \ll \hbar\omega_T - \mu$ the atoms will stay in the ground state in the transverse directions. The axial trap in this case is shallower, $\omega_A \ll \omega_T$, offering higher order states for the gas to occupy while still populating the ground state in the transverse directions. This situation necessitates that the atoms can only freely move in the axial direction and thus form a quasi one-dimensional gas.

These one-dimensional geometries can be created by exploiting the versatility of the optical lattice potential in Eq.(1.11). A quasi one-dimensional regime can be reached by increasing the lattice depth in two directions (y and z) by increasing the laser intensity. Along the third direction (x) the laser intensity is decreased so that the atoms can move freely and this forms an array of one-dimensional tubes of atoms. By further increasing the lattice depth in the y and z directions tunneling between adjacent tubes is restricted ensuring a number of independent systems.

To characterise the different regimes of one-dimensional Bose gases we introduce the Lieb-Liniger parameter, $\gamma = I/K$, which is the ratio of the interaction energy to the kinetic energy of the particles [43]. For a homogeneous gas $I = g_{1D}n$ and $K = \hbar^2 n^2/m$, and γ can be expressed as

$$\gamma = \frac{m g_{1D}}{\hbar^2 n} \,, \tag{1.13}$$

where g_{1D} is the one-dimensional interaction strength, m is the mass of a single atom and n is the density of the gas. When $\gamma \ll 1$ the interactions between the particles are in the mean field limit and the gas acts like a 1D fluid. As γ is increased the atoms start to fermionize (see below), and when $\gamma \gg 1$ the gas enters the so-called Tonks-Girardeau regime. To induce this strongly interacting regime one must find ways to reduce the kinetic energy of the gas.

1.2.3 Point-like Interactions

At low temperatures the de Broglie wavelengths of the particles become larger than the inter-atomic spacing and are large compared to the range of the interaction potential between two interacting particles. In this low energy regime the scattering between two atoms may be assumed to be s-wave (angular momentum $l = 0$) as higher partial waves do not have enough energy to exceed the centrifugal barrier and enter the scattering region. The atoms are mostly unaffected by the long range form of the interaction

potential and only feel the short range part, which may be approximated by a delta function pseudo-potential [44],

$$g_{3D}V(|\mathbf{r}_1 - \mathbf{r}_2|) \approx g_{3D}\delta(|\mathbf{r}_1 - \mathbf{r}_2|) \; . \tag{1.14}$$

Restricting our system to one dimension not only eases calculating the solutions to the system's Hamiltonian but also offers very different physics to that seen in three dimensions. This is due, in large part, to the particles interaction strength, g_{3D}, which is dependent on the atom's scattering length, a_{3D}, and in three dimensions the two are proportional $g_{3D} \propto a_{3D}$. However in 1D this is not the case, the scattering length and interaction strength are inversely proportional to each other

$$g_{1D} = -2\hbar^2/m_r a_{1D} \; , \tag{1.15}$$

where m_r=$m_1 m_2/(m_1$+$m_2)$ is the reduced atomic mass of the two scattering particles. The one-dimensional scattering length a_{1D} is related to the actual three-dimensional one via a_{1D}=$-\,a_\perp^2/2a_{3D}(1 - Ca_{3D}/a_\perp)$. Here $a_\perp$ is the size of the single-atom ground state wavefunction in the transversal direction and $C \simeq 1.4603\ldots$ is a constant [45]. Eq.(1.15) can then be rewritten as

$$g_{1D} = \frac{4\hbar^2 a_{3D}}{m_r a_\perp^2} \frac{1}{1 - \frac{Ca_{3D}}{a_\perp}} \; . \tag{1.16}$$

As stated previously interactions can be tuned in atomic ensembles by driving Feshbach resonances using external magnetic fields [38] and for one-dimensional configurations, interactions can also be significantly enhanced through so-called confinement-induced resonances [45].

1.3 Degenerate Fermi Gas

Fermions have been trapped and confined to lower dimensions in two and one dimensional traps [46, 47], typically containing $N \approx 10^6$ atoms. However recent progress in small Fermi systems has lead to unprecidented control over the number of fermions which can be trapped in 1D. In the group of S. Jochim at the University of Heidelberg, ground-states of one to ten atoms are prepared with fidelities of $\sim 90\%$ by using a small volume optical trap with large level spacing [4]. The trap has axial and radial trapping frequencies $(\omega_R, \omega_A) = 2\pi \times (14.0 \pm 0.1, 1.487 \pm 0.010)$kHz and is loaded with a two component mixture of about 600 ^{6}Li atoms. A linear potential is added in the axial direction by applying a magnetic field gradient which allows higher energy fermions in the Fermi gas to tunnel from the trap. If the resulting system has ten atoms or less it is

essentially one-dimensional and one atom of each spin occupies each energy level. The number of fermions left in the trap can then be measured by recording their flouresence. This ability to accurately prepare few-body states can lead to experiments exploring Andersons orthogonality catastrophe in small Fermi gases which will be discussed in Chapter 4, and also investigating entangled bi-partite states which will be discussed in Chapter 2.

1.4 The Tonks-Girardeau Gas

The Tonks-Girardeau (TG) gas is a one-dimensional system composed of infinitely repulsive bosons which are commonly refered to as *hard-core* bosons. Let us consider a gas of N bosons trapped in a tight atomic trap that restricts the dynamics of the gas in the transversal directions and can be described as quasi one-dimensional as discussed previously. The Hamiltonian can be written as

$$\mathcal{H}(x_1, \ldots, x_N) = \sum_{n=1}^{N} \left[-\frac{\hbar^2}{2m} \frac{\partial^2}{\partial x_n^2} + V_{ext}(x_n) \right] + g_{1D} \sum_{i<j} \delta(|x_i - x_j|) \; . \tag{1.17}$$

In the limit of infinitely strong repulsion, $g_{1D} \to \infty$, each boson can be thought of as a hard sphere such that no two particles in the TG gas can occupy the same place at the same time [48, 49]. This constraint on the allowed wavefunctions of the TG gas is a bosonic analogy of Pauli's exclusion principle for fermions, which states that no two fermions which possess the same spin can occupy the same quantum state simultaneously. As a result of this, a gas of spinless fermions at $T = 0$ will singly occupy every energy level in an external potential up to the Fermi energy, forming the so-called *Fermi sea*. This strange equivalence is due solely to the dimensionality of the system - as the repulsive interactions become stronger, the particles are no longer free to overlap, thus mimicking the Pauli-exclusion principle in configuration space. To further relate the bosonic and fermionic systems, M. Girardeau showed how one can mathematically map the strongly interacting bosons onto a state of ideal fermions, which allows us to describe the full many-body state of the TG gas [7]. This procedure is known as the Fermi-Bose mapping theorem and it can be used to show that the *local* density and correlation functions of this *strongly correlated* system are equivalent to the corresponding quantities of a *non-interacting* spin polarized Fermi gas. In this mapping the infinite interaction between the bosons is replaced by a boundary condition on the allowed bosonic wave-function

$$\Psi_B(x_1, x_2, \ldots, x_n) = 0 \quad \text{if} \quad |x_i - x_j| = 0 \; , \tag{1.18}$$

for $i \neq j$ and $1 \leq i \leq \ j \leq N$. This is simply the hard core constraint which says that no probability exists for two particles to be at the same point in space, and results in the following Hamiltonian for a gas of ideal particles

$$\mathcal{H} = \sum_{n=1}^{N} \left[-\frac{\hbar^2}{2m} \frac{\partial^2}{\partial x_n^2} + V_{ext}(x_n) \right] . \tag{1.19}$$

For this fermionic system the many-body wave-function can be calculated using a Slater determinant

$$\Psi_F(x_1, x_2, \ldots, x_N) = \frac{1}{\sqrt{N!}} \det_{(n,j)=(0,1)}^{(N-1,N)} \psi_n(x_j) , \tag{1.20}$$

where the ψ_n are the single particle eigenstates of the system. This, however, leads to a fermionic rather than bosonic symmetry, which can be corrected by a multiplication with the appropriate unit antisymmetric function

$$A(x_1, x_2, \ldots, x_N) = \prod_{1 \leq i < j \leq N} \mathrm{sgn}(x_i - x_j) , \tag{1.21}$$

to give the many-body Tonks-Girardeau state

$$\Psi_B(x_1, x_2, \ldots, x_N) = A(x_1, x_2, \ldots, x_N) \Psi_F(x_1, x_2, \ldots, x_N) . \tag{1.22}$$

The bosonic ground state is always positive and this means the the unit antisymmetric function $A(x_1, ..., x_N)$ must have the same sign as Ψ_F for all x_n, which results in

$$\Psi_B(x_1, x_2, \ldots, x_N) = |\Psi_F(x_1, x_2, \ldots, x_N)|. \tag{1.23}$$

This implies that local properties of the TG gas are the same as a non-interacting Fermi gas, such as the probability density, $|\Psi_B|^2 = |\Psi_F|^2$. However the corresponding correlation functions and momentum distributions differ.

Experiments to create and control the TG gas have seen some exciting breakthroughs in the past few years and here we will briefly introduce some of the progress in this field.

1.4.1 First Experimental Observation

In 2004 the first TG gas was created by the group of I. Bloch in Mainz, Germany [8]. A 2D optical lattice was formed by superposing two orthogonal standing waves with a wavelength of 823nm onto a BEC containing approximately 3×10^4 ^{87}Rb atoms. As the optical lattice only traps the atoms in the y-z plane, 1D tubes are created. The number of atoms in each tube was dependent on the position of the tube in the lattice; if it is

near the edges the atom number was found to be smaller than if it was positioned near the centre. The maximum number of particles in the centre of the lattice was $N \approx 20$. The depth of this 2D lattice was $27E_r$, where E_r is the recoil energy $\hbar^2k^2/2m$ with k being the wavevector of the lattice laser. This large lattice depth ensured that there was no tunneling between adjacent tubes. Along the axial direction the atoms were trapped in a weak harmonic potential of frequency $\omega_a \approx 2\pi \times 60Hz$.

To increase γ a periodic potential along the axial direction was applied where the interaction energy of the particles is $I = U\nu$ and the kinetic energy is $K = J\nu$, leading to a Lieb-Liniger parameter $\gamma = U/J$. Here ν is the filling factor of the lattice, U is the on-site energy and J is the tunneling amplitude. By reducing the tunneling between the sites, γ can be increased to approach the TG regime. This was achieved by increasing the depth of the periodic potential and by using a laser of wavelength 854nm the lattice depth was slowly increased until a maximum trap depth of $18.5E_r$ was reached. The momentum distribution of the gas was then measured by removing all trapping potentials and imaging the gas after it expands, which allowed for comparison of the momentum profile versus theory. The work confirmed the existence of a TG gas in the region $\gamma \approx 5 - 200$. For finite γ in this range the existence of the TG gas can be verified by measuring the dynamic structure factor which becomes a step function in the TG limit $\gamma^{-1} = 0$ [9].

A TG gas can also be created without an additional lattice potential but rather by reducing the density of the gas along the axial direction of the tube. This was achieved by the group of D. S. Weiss in the Pennsylvania State University when they observed the creation of a TG gas also in 2004 [10]. Having created a Bose gas in a lattice of 1D tubes the transverse trapping frequencies were increased forcing the gas to spread out along the axial direction. Consequently this reduced the density until the single particle wavefunctions became localised and a maximum $\gamma = 5.5$ was reached. Once deep in the TG regime any further squeezing of the trap geometry has no effect on the resulting state which is fully described by an effective 1D Hamiltonian.

1.5 Reduced single particle density matrix

Throughout this thesis the most important tool which will be used is the reduced single particle density matrix (RSPDM) [50]. The RSPDM is an important quantity when investigating ultracold gases as many one-particle observables can be derived from it. Its importance will be discussed separately for two interacting particles in Chapter 2 and Chapter 5 and for the TG gas in Chapter 3 when quantifying entanglement, superpositions and coherence. The RSPDM is the kernel of the density operator in configuration

space and for pure states is defined as

$$\rho^1(x,x') = N\int_{-\infty}^{\infty}\Psi_B^*(x,x_2,\ldots,x_N)\Psi_B(x',x_2,\ldots,x_N)dx_2\ldots dx_N\ , \tag{1.24}$$

where $\Psi(x,x_2,\ldots,x_N)$ is a many body wavefunction. The RSPDM is normalised to N and its trace is given by $\mathrm{Tr}(\rho^1) = \int\rho^1(x,x)dx = N$. Once the RSPDM is calculated one can extract important single particle information from it such as the single particle density which is simply the principle diagonal of the RSPDM $\rho(x) = \rho^1(x,x)$.

A representation that will be explored continuously in this thesis are the natural orbitals of the many-body system. The natural orbitals are eigenfunctions of the RSPDM and are obtained by solving the following integral equation [51]

$$\int dx\rho^1(x,x')\phi_i(x) = \lambda_i\phi_i(x')\ , \tag{1.25}$$

where λ_i are the corresponding eigenvalues and $\sum_i\lambda_i = N$. The RSPDM can therefore be written in the basis of the natural orbitals as

$$\rho^1(x,x') = \sum_i\lambda_i\phi_i^*(x)\phi_i(x'). \tag{1.26}$$

The natural orbitals can be thought of as effective single particle states which are occupied by the bosons with λ_i being the occupancy of each orbital. For the case of a BEC the lowest orbital is macroscopically occupied $\lambda_0 = N_0 \sim N$ and all other orbitals have only microscopic occupation. As the BEC is a coherent matter wave with macroscopic occupation of the ground state an argument can be made which relates the size λ_0 to the coherence of the gas. For a TG gas there is no condensate and the occupation of the ground state scales with $\lambda_0 \propto \sqrt{N}$ [52]. The behaviour of λ_0 and its connection to coherence will be explored in detail in Chapter 3.

The momentum distribution of the gas is an important tool which can be routinely measured in cold atom experiments and can also be calculated from the RSPDM through a Fourier transform

$$n(k) = \frac{1}{2\pi\hbar}\int\int\rho^1(x,x')e^{\frac{ik(x-x')}{\hbar}}dx\,dx'. \tag{1.27}$$

By taking the Fourier transform of the natural orbitals $\tilde{\phi}(k)$ one may also write the momentum distibution as $n(k) = \sum_i\lambda_i\tilde{\phi}_i(k)^*\tilde{\phi}_i(k)$.

1.6 Summary of work done in the thesis

1.6.1 Chapter 2

A system of two interacting atoms is investigated where the atoms are confined to individual harmonic traps which are separated by a distance d. The structure of the Hamiltonian allows one to separate the problem into the centre of mass and relative coordinate systems. The centre of mass Hamiltonian is that of a single atom in a harmonic potential and is readily solved analytically. The relative coordinate system takes the form of a single atom in a harmonic trap which is punctuated by a delta function potential at a distance d from the centre of the trap. The height of the delta function relates to the strength of the interaction between the two particles. This Hamiltonian is also exactly analytically solvable through the use of parabolic cylinder functions. With the complete many-body wavefunction solved, a thorough analysis of the correlations between the two atoms is undertaken. The entanglement of the atoms is calculated from the von Neumann entropy which shows the existence of trap induced shape resonances. The non-local behaviour of the continuous variable state is investigated by calculating the two-mode Wigner distribution of the two particle state. If the Wigner function is negative there is an indication of the non-classicality of the state which can be quantified through the violation of a Clauser-Horne-Shimony-Holt inequality even at finite temperature. Finally with a suitable choice of entanglement witnesses we show how inefficient detectors can affect the measured outcome.

Non-locality of two ultracold trapped atoms
T. Fogarty, Th. Busch, J. Goold and M. Paternostro
New Journal of Physics **13** (2), 023016 (2011)

1.6.2 Chapter 3

The problem of a Tonks-Girardeau gas in an asymmetrically split harmonic oscillator is solved. The trap is split by a δ-function of variable height that can be positioned at any point along the trap axis. The density and total energy of the gas is investigated as a function of the position of the δ-function and the coherence of the gas is examined. This is assessed by calculating the reduced single particle density matrix which contains information about the coherence of the gas in the populations of the natural orbitals. The height of the central peak of the momentum distribution can also be used as an indication of the coherence of the gas. The dynamics of the gas after sudden removal of the delta function potential is investigated which leads to

comparisons to the Talbot effect in optics and Friedel oscillations of electrons in metals.

An eccentrically perturbed Tonks-Girardeau gas
J. Goold, M. Krych, Z. Idziaszek, T. Fogarty and Th. Busch
New Journal of Physics **12** (9), 093041 (2010)

1.6.3 Chapter 4

The orthogonality catastrophe (OC) is a phenomenon common in solid state physics where the overlap between two many-body states, which differ through the presence of an impurity, quickly become orthogonal as the size of the system is increased. P.W. Anderson's original work on the OC is discussed along with the time-dependent appearance of OC in X-ray absorption experiments. The OC is investigated in a non-interacting gas of fermions after being perturbed by a localised impurity taking the form of a δ-function or Gaussian potential. As a measure of the irreversibility of a state the Loschmidt echo is calculated as a function of time after the impurity is suddenly immersed in the Fermi gas, the effect of the OC can then be explored in a dynamical process. The potential experimental observation of OC by using Ramsey interferometry, by which one can measure the single particle spectrum is also discussed.

Orthogonality catastrophe as a consequence of qubit embedding in an ultracold Fermi gas
J. Goold, T. Fogarty, N. LoGullo, M. Paternostro and Th. Busch
Physical Review A **84** (6), 063632 (2011)

1.6.4 Chapter 5

The creation of superposition states is investigated using the free oscillation atom interferometer with emphasis on creating a macroscopic superposition state called the NOON state. The oscillatory motion of two displaced interacting atoms in a harmonic trap are used as the driving mechanism of the interferometer. Superposition states are created after the atoms scatter repeatedly off a centrally situated δ-function which acts as a beam-splitter. The time evolution of the two-body state is exactly calculated for different interaction regimes. The usefulness of the state for quantum metrology is assessed by calculating the quantum Fisher information of the evolving state. The quantum Fisher information can quantify if a state exceeds the standard quantum limit, which limits classical

interferometers, or if it can reach the Heisenberg limit which is the upper bound for quantum interferometers. At the Heisenberg limit the quantum Fisher information is maximum and the state is in a spatially maximally entangled state, the so-called NOON state. Finally we propose a way to detect the creation of a NOON state in this setup through expansion of the de-localised state and measurement of the ensuing interference pattern.

Effect of interparticle interaction in a free-oscillation atomic interferometer
T. Fogarty, A. Kiely, S. Campbell and Th. Busch
Physical Review A **87**, 043630 (2013)

1.6.5 Chapter 6

The growth of entanglement mediated by a linear ion chain is considered as a viable system to create long distance correlations. The ion chain contains two impurity ions of a different atomic species which are positioned symmetrically around the centre of the chain and are separated by bath ions. Initially the impurities are prepared in a squeezed state and the bath is at a finite temperature. Entanglement is generated between the transverse modes of the impurites which are coupled to the axial modes of the bath ions by means of an external laser. Bath mediated entanglement is observed and a decoherence-free subspace is found to exist if the frequencies of the impurities are carefully tuned to conincide with nodes of the collective dynamics of the bath.

Entangling two defects via the surrounding crystal
T. Fogarty, E. Kajari, B.G. Taketani, A. Wolf, Th. Busch and G. Morigi
Phys. Rev. A **87**, 050304(R) (2013)

Chapter 2

Entanglement and non-locality between two interacting atoms

2.1 Introduction

Quantum correlations are an important resource in quantum information and a lot of work has been done in the last two decades exploring correlations in simple systems such as qubits [53–55]. A qubit is a state with a two dimensional Hilbert space (horizontal and vertical polarisations of a photon, spin 1/2 systems, two outputs of a beamsplitter to name but a few) and can also be thought of as an approximation of the physical properties of a quantum system such as two hyperfine levels in an atom [56, 57], two different spatial modes in a double well potential [58, 59] or two different vibrational states of a micromechanical oscillator [60, 61]. Approximating complex systems as simpler two-level models can be beneficial as it can lead to analytic models for entanglement generation between two qubits in a variety of environments and configurations. Even though qubit systems offer a simplified view of physicial processes they can describe the basic effects of quantum systems and are convenient to explore new concepts and ideas. However by taking a simplified view of a particle one can miss out on the interesting physics which exists by considering unavoidable interactions in atomic ensembles. For this reason it is rewarding to investigate continuous variable (CV) correlations between a particle's conjugate position and momentum coordinates.

I would like to acknowledge the contribution of Dr. Paternostro, who proposed the detection scheme outlined in Section 2.5.2 and who formulated the dissipation process in Section 2.6.

In this Chapter we will describe the quantum correlations for the fundamental system of two atoms interacting with a point-like potential. The atoms are confined to individual harmonic traps which are separated by a finite distance. For mathematical simplicity the atoms motion is confined to only one dimension which is achieved by tightening the confining potential in the other two directions. The model is solvable thanks to the ability to separate the two-body Hamiltonian into two separate single particle Hamiltonians consisting of the centre of mass and relative motions of the atoms. The centre of mass motion is that of a single atom in a harmonic trap which can be solved analytically using Hermite polynomials. The relative motion is more complicated and involves an atom in a harmonic trap which is perturbed by a δ-function potential. Below we show that the δ-function's position is related to the distance between the two traps and its height is related to the interaction strength between the atoms. This single particle Hamiltonian is also solvable by using parabolic cylinder functions which will be explored in Section 2.2.

The correlations in this system will be focused on two properties: entanglement and non-locality. For this we we will briefly introduce ideas from classical information theory, notably the Shannon entropy and its quantum mechanical analogue, the von Neumann entropy, non-locality and the CHSH inequality.

2.1.1 Shannon Entropy

In classical information theory if a system A is known to be in one of the following states $a_1, a_2, ..., a_n$ with corresponding probabilities $p_1, p_2, ..., p_n$ then the Shannon entropy [62] quantifies the amount of information gained in identifying the state

$$H(p_1, p_2, .., p_n) = -\sum_{i=1}^{n} p_i \log_2 p_i. \tag{2.1}$$

Consequently H also quantifies the amount of uncertainty in the state before it is identified. As an example, if $p_j = 1$ and $p_i = 0$ for all $i \neq j$, then $H = 0$ because there is zero uncertainty in the state. Conversely the maximum information gained in identifying the state is obtained when the probabilities are all equal, ie. $p_j = 1/n$ for all j which results in $H = \log_2 n$.

2.1.2 Von Neumann Entropy

The quantum analogue of Shannon entropy is the von Neumann entropy [63]. As the Shannon entropy dealt with uncertainty in a classical probability function, the von

Neumann entropy deals with the uncertainty in the density matrix

$$\hat{\rho} = \sum_{i=1}^{n} p_i \hat{\rho}_i = \sum_{i}^{n} p_i |\psi_i\rangle\langle\psi_i|. \tag{2.2}$$

As the probabilities must sum to unity, $\sum_i^n p_i = 1$, any density matrix has the property that $\mathrm{Tr}(\hat{\rho}) = 1$. By performing measurements on the unknown state $\hat{\rho}$ we can then gain information about the state which is quantified by the von Neumann entropy as

$$S(\hat{\rho}) = -\mathrm{Tr}(\hat{\rho}\log_2\hat{\rho}). \tag{2.3}$$

If we label the eigenvalues of $\hat{\rho}$ as λ_i this can be rewritten as

$$S(\hat{\rho}) = -\sum_{i}^{n} \lambda_i \log_2 \lambda_i \ , \tag{2.4}$$

[64–67] where $0\log_2 0 = 0$ which is supported by the fact that $\lim_{x\to 0} x\log_2 x = 0$. For pure product states $\hat{\rho} = \hat{\rho}_A \otimes \hat{\rho}_B$ the von Neumann entropy is zero and there is no shared information between the states A and B. For a pure state the von Neumann entropy is a good measure of entanglement and is therefore very powerful [68]. However it is difficult to measure in a laboratory as it requires full reconstruction of the state and is sensitive to fluctuations due to the dependence on the logarithm. For mixed states the von Neumann entropy is not an indication of the entanglement of the state but rather a measure of the mixedness of the state. This can be understood by realising that for pure states the von Neumann entropy is calculated from the reduced state of the the two particle system which involves tracing out one subsystem. If the state is not entangled the von Neumann entropy is zero, as the resulting state is pure and no mutual information has been lost from tracing out one of the subsystems. However if the state is entangled the act of tracing out one subsystem discards information that each subsystem shares, and the reduced state becomes mixed, which is indicated by a non-zero von Neumann entropy. So if we were to calculate the von Neumann entropy for a mixed state, the reduced state will have a mixedness both attributed to the mixed full state and also any entanglement between the subsystems. As one cannot be isolated from the other a different measure for quantum correlations must be used. For this reason we will now discuss calculating the non-locality of the state. The set of non-local states is a subset of the set of entangled states, and therefore non-locality ensures entanglement [69].

2.1.3 Non-locality and the CHSH inequality

Non-classicality can be evaluated by means of a Bell test which was first postulated by John Bell in 1964 [70]. Bell's theorem states that no physical theory of local hidden variables can ever produce all of the predictions of quantum mechanics. The idea of a Bell test is to show that physics should possess *local realism*: Reality - Microscopic objects have real properties associated with them that determine the outcome of quantum mechanical experiments, regardless of whether an observer makes a measurement or not; Locality - that the real properties in one location are not influenced non-relativistically by measurements performed simultaneously at a distant location [71]. However quantum mechanics can be shown to violate a Bell test and thus disobey local-realism. In this work we will show how a certain Bell test, the CHSH inequality named after J. Clauser, M. Horne, A. Shimony and R. A. Holt [72], is violated by two interacting atoms.

Imagine two particles are prepared and are given to two experimentalists, Alice and Bob. Once Alice receives her particle she performs randomly one of two different measurements on her particle, which tell her about two physical properties P_a and $P_{a'}$. Once the measurement is done Alice has a value a or a' for property P_a or $P_{a'}$. Bob can also carry out two measurements to measure b or b' of P_b or $P_{b'}$. For simplicity we will assume that the outcomes of a, a', b and b' can only take the values $+1$ or -1. We also assume that Alice and Bob carry out their measurements at the same time, so that Alice's measurement cannot disturb Bob's and vice versa since super luminal communication is prohibited.

Let us consider the expression

$$AB + A'B + A'B' - AB' \tag{2.5}$$

which contains all the possible outcomes from the simultaneous measurements. By noticing that

$$AB + A'B + A'B' - AB' = B(A + A') + B'(A' - A) \tag{2.6}$$

we find that either $B(A + A') = 0$ or $B'(A' - A) = 0$ because $A, A' = \pm 1$. This means that $AB + A'B + A'B' - AB' = \pm 2$, which is easy to see. Let us suppose now that before the measurements are performed the system is in a state $A = a$, $A' = a'$, $B = b$ and $B' = b'$ with probability $p(a, a', b, b')$. If we calculate the average value of this expression

we find

$$\begin{aligned} E(AB + A'B + A'B' - AB') &= \sum_{a,a',b,b'} p(a,a',b,b')(ab + a'b + a'b' - ab') \\ &\leq \sum_{a,a',b,b'} p(a,a',b,b') \times 2 \\ &= 2 \end{aligned} \tag{2.7}$$

where $\sum_{a,a',b,b'} p(a,a',b,b') = 1$. We can also rewrite this expression as

$$\begin{aligned} E(AB + A'B + A'B' - AB') = &\sum_{a,a',b,b'} p(a,a',b,b')ab + \sum_{a,a',b,b'} p(a,a',b,b')a'b \\ &+ \sum_{a,a',b,b'} p(a,a',b,b')a'b' - \sum_{a,a',b,b'} p(a,a',b,b')ab' \\ &= E(ab) + E(a'b) + E(a'b') - E(ab'). \end{aligned} \tag{2.8}$$

Combining the last two expressions gives us the CHSH inequality

$$\mathcal{B} = E(ab) + E(a'b) + E(a'b') - E(ab') \leq 2. \tag{2.9}$$

This inequality has to be fulfilled if Alice and Bob carry out the experiment many times and average over the different pairs of measurement results. It is a consequence of local-realism and therefore has to be fulfilled by all theories including hidden variables.

Let us now consider the situation using quantum mechanical states. For simplicity we assume that the particles are qubits prepared in the initial state

$$|\Psi^-\rangle = \frac{|01\rangle - |10\rangle}{\sqrt{2}} \, . \tag{2.10}$$

The first qubit is given to Alice and the second qubit to Bob and they perform measurements of the following observables

$$\begin{aligned} A = Z_A \quad & B = \tfrac{-Z_B - X_B}{\sqrt{2}} \\ A' = X_A \quad & B' = \tfrac{Z_B - X_B}{\sqrt{2}} \, , \end{aligned} \tag{2.11}$$

where X and Z are the Pauli operators. The expectation values of the observables can be easily calculated as $\langle AB\rangle = 1/\sqrt{2}$, $\langle A'B\rangle = 1/\sqrt{2}$, $\langle A'B'\rangle = 1/\sqrt{2}$ and $\langle AB'\rangle = -1/\sqrt{2}$, which results in $\mathcal{B} = 2\sqrt{2}$. This violates the inequality in Eq.(2.9), and therefore shows that quantum mechanics does not obey *local realism*. In fact here we have used the maximally entangled state $|\Psi^-\rangle$, which is one of the Bell states that are known to maximally violate Bell's inequality. The CHSH inequality is therefore a good test for

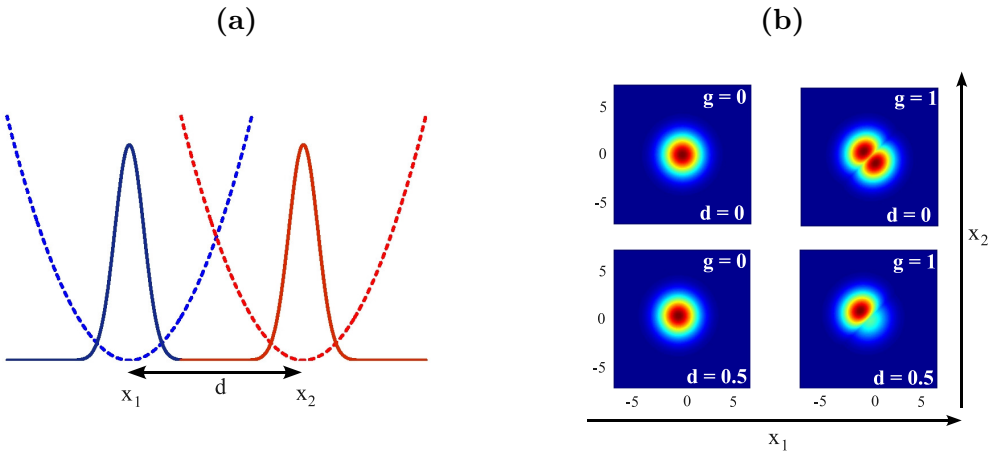


FIGURE 2.1: Panel **(a)** shows a schematic representation of the system at hand [see the Hamiltonian model in Eq. (2.12). Panel **(b)** shows the two-particle probability density for two different distances d between the traps and two distinct values of the scaled interaction strength g. The axes are scaled in terms of a as defined in the text.

quantum correlations. Performing Bell tests are a mainstay in quantum optics experiments to test non-locality[73–77], even though loopholes to the test still persist [78–80], the experimental feasibility will be discussed in Section 2.5.2.

2.2 Model Hamiltonian

We consider two bosonic atoms confined along the x axis (the *axial direction*) in two separate, but overlapping harmonic potentials, as shown in Fig. 2.1**(a)**. The atoms are tightly confined along directions perpendicular to x (*the transverse directions*) by high-frequency harmonic trapping potentials. As a result of the large energy level separation associated with the transverse confinement, at low temperature the transverse motion is restricted to the lowest mode and the system can be described by the quasi one-dimensional Hamiltonian

$$\hat{H} = -\frac{\hbar^2}{2m_1}\nabla_1^2 - \frac{\hbar^2}{2m_2}\nabla_2^2 + \frac{m_1}{2}\omega^2(x_1 - d_1)^2 + \frac{m_2}{2}\omega^2(x_2 - d_2)^2 + g_{1D}\delta(x_1 - x_2), \quad (2.12)$$

where m_1 and m_2 are the masses of the two atoms and x_1 and x_2 are their respective spatial coordinates. We assume both traps to have the same frequency ω and be displaced by the distances d_1 and d_2 from the origin of the coordinate system. By introducing the centre of mass coordinate $X = (x_1 + x_2)/2$ and the relative coordinate $x = (x_1 - x_2)/2$, the two-atom wavefunction can be factorised into $\phi(X)\psi(x)$ with $\phi(X)$ being the wavefunction for the centre-of-mass dynamics and $\psi(x)$ being the wavefunction of the relative

motion. In these new variables, the Schrödinger equation decouples as

$$\left(-\frac{\hbar^2}{2M}\frac{\partial^2}{\partial X^2}+\frac{1}{2}M\omega^2X^2\right)\phi(X) \quad = \hbar\omega\left(n+\tfrac{1}{2}\right)\phi(X)\,, \tag{2.13}$$

$$\left(-\frac{\hbar^2}{2m_r}\frac{\partial^2}{\partial x^2}+\frac{1}{2}m_r\omega^2(x-d)^2+g_{1D}\delta(x)\right)\psi(x) \quad = \hbar\omega\left(\nu+\tfrac{1}{2}\right)\psi(x)\,, \tag{2.14}$$

where we have taken m_1=m_2=m for simplicity, and defined $d = d_1 - d_2$, $M = 2m$ and $m_r = m/2$. The centre-of-mass dynamics has the form of simple harmonic motion which has the following solution:

$$\phi_n(X) = \frac{1}{\sqrt{2^n n!}}\left(\frac{M\omega}{\pi\hbar^2}\right)^{\frac{1}{4}} e^{-\frac{M\omega X^2}{2\hbar}} H_n\left(\sqrt{\frac{M\omega}{\hbar}}X\right) \tag{2.15}$$

where H_n are Hermite polynomials and $n = 0, 1, 2...$

The Hamiltonian for the relative coordinate consists of a displaced harmonic oscillator subjected to a point-like disturbance at the origin of the coordinate system which is also analytically solvable [81, 82]. For simplicity of notation we first scale all the lengths in units of $a = \sqrt{\hbar/m\omega}$, which is the width of the ground state wavefunction for a single unperturbed particle of mass m along the axial direction of one of the harmonic traps, and all energies in units of $\hbar\omega$.

Eq. (2.14) thus becomes (for $x \neq 0$)

$$\frac{d^2\psi(\xi)}{d\xi^2}+\left(\nu+\frac{1}{2}-\frac{\xi^2}{4}-g\,\delta(\xi+d)\right)\psi(\xi)=0\,, \tag{2.16}$$

where $g = g_{1D}a/(\hbar\omega)$ is the renormalised strength of the δ-barrier, and $\xi = (x - d)$ is a shifted spatial coordinate which lets us interpret the system as a harmonic oscillator with an off-centre δ-function. On either side of the δ-function the solutions of the differential equation Eq. (2.16) are parabolic cylinder functions $D_\nu(\xi)$, which vanish for $\xi \to \infty$, but diverge for $\xi \to -\infty$, Fig. 2.2. We can therefore write the solution piecewise as

$$\psi(\xi) = \psi_l(\xi)\theta(d-\xi) + \psi_r(\xi)\theta(\xi-d)\,, \tag{2.17}$$

with

$$\psi_l(\xi) = N_- D_\nu(-\xi) \quad \text{and} \quad \psi_r(\xi) = N_+ D_\nu(\xi)\,, \tag{2.18}$$

and $\theta(\xi)$ being the Heaviside function. The condition of continuity of these solutions at the position of the δ-function

$$N_+ D_\nu(-d) = N_- D_\nu(d)\,, \tag{2.19}$$

together with the solution of the Schrödinger equation

$$-\int_{d-\epsilon}^{d+\epsilon}\psi^{''}(\xi)d\xi+\int_{d-\epsilon}^{d+\epsilon}V(\xi)\psi(\xi)d\xi=\epsilon_\nu\int_{d-\epsilon}^{d+\epsilon}\psi(\xi)d\xi\ , \tag{2.20}$$

with

$$V(x)=\frac{1}{4}\xi^2+g\delta(\xi+d)\ , \tag{2.21}$$

leads to a transcendental equation which determines the energy eigenvalues as a function of both, g and d

$$N_+D'_\nu(-d)+N_-D'_\nu(d)-2gN_+D_\nu(-d)=0\ . \tag{2.22}$$

The required derivatives of the parabolic cylinder functions can be calculated using the recurrence relation [83]

$$D'_\nu(z)=\nu D_{\nu-1}(z)-\frac{1}{2}zD_\nu(z)\ , \tag{2.23}$$

and for $D_\nu(d)\neq 0$ we find from Eq. (2.19) the relation $N_-=N_+D_\nu(-d)/D_\nu(d)$. Substituting these into Eq. (2.22) we therefore get

$$\nu\Big[D_{\nu-1}(-d)D_\nu(d)+D_{\nu-1}(d)D_\nu(-d)\Big]=2gD_\nu(-d)D_\nu(d)\ . \tag{2.24}$$

This equation determines the eigenenergies for the solutions that are nonzero at the position of the δ-function potential. To find the ones for which $D_\nu(d)=0$ we can see from Eq. (2.19) that $D_\nu(-d)=0$, provided that $N_+\neq 0$ and $N_-\neq 0$. Then Eq. (2.22) reduces to

$$N_+\nu D_{\nu-1}(-d)+N_-\nu D_{\nu-1}(d)=0, \tag{2.25}$$

where the derivatives have been determined using Eq. (2.23). The above equation together with the normalization of the total wave function determines N_+ and N_- for the solutions that vanish at the position of the δ-function potential. These solutions are independent of g, and they correspond to the harmonic oscillator wave functions that have a node at $x=d$.

The energy spectrum of the system exhibits trap-induced shape resonances due to energy-level repulsion and is shown in Fig. 2.3 [81, 82]. Shape resonances occur when a molecular bound state becomes resonant with higher order trap states at which points avoided crossings occur. In this case the resonance is a consequence of the δ-function interaction potential in the relative coordinate around which the relative motion of the atoms form a nearly stable bound state. This is illustrated in Fig. 2.4 where the relative wavefunction of the third excited state is plotted against d in the left panel and the corresponding relative energy is plotted in the centre panel. The wavefunction at the positions of the resonances are also plotted in the right most panel. Here the δ-function is positioned at $x=0$ and the harmonic trap is centered at $x=d$. Initially at small d

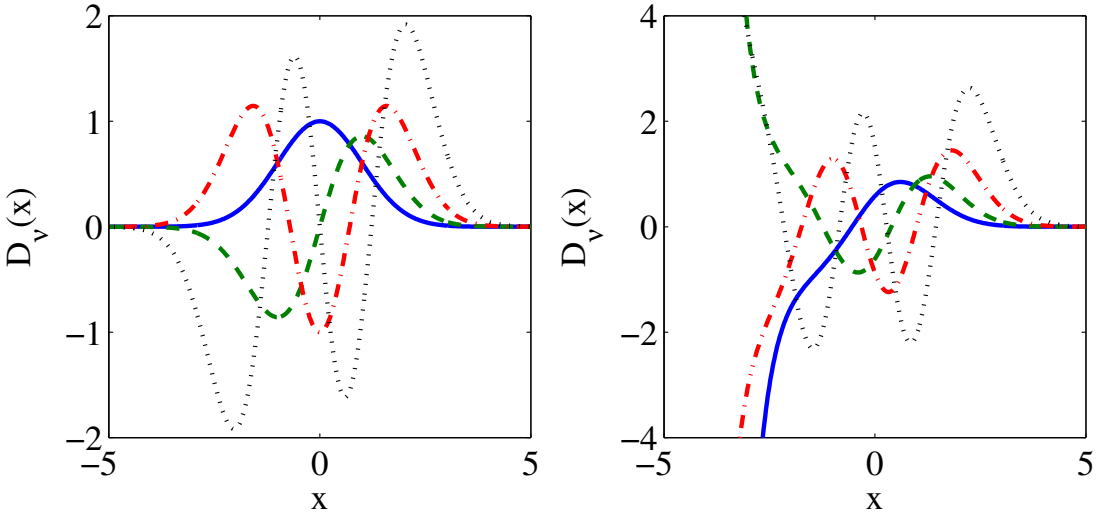


FIGURE 2.2: Parabolic cylinder function $D_\nu(x)$ plotted in the left panel for $\nu = 0$ (blue line), $\nu = 1$ (green), $\nu = 2$ (red), $\nu = 3$ (black) which reduce to the solutions of the harmonic oscillator. $D_\nu(x)$ plotted in the right panel for $\nu = 0.5$ (blue), 1.5 (green), 2.5 (red), 3.5 (black). Here it is apparent that the functions diverge for $x \to -\infty$.

the energy starts to increase as the origin of the harmonic trap is moved away from the δ-function, however the wavefunction remains localised to the left of the δ-function. At the first resonance $d = 0.76$ the wavefunction becomes degenerate with the next highest state and has acquired an extra node. Due to the forbidden crossing of the energy levels the energy decreases after this and the wavepacket is on the right side of the δ-function and is localised in the trap. After the next resonance at $d = 1.74$ the δ-function is at a node of the wavefunction and does not affect it, thus the energy and waveform return to its undisturbed state. After each successive resonance the average position of the wavefunction changes drastically mirroring the change in energy. After the last resonance the wavepacket moves out of range of the δ-function and is affected primarilarly by the trap potential for $d > 4$. Notably, no resonance is observed in the ground state for $g > 0$, however for $g < 0$ a resonance is present which is due to the existence of a bound state in this situation (indicated by circle in Fig. 2.3**(a)**). It is on this bound state which we will concentrate on in future sections.

The ground-state wavefunction can be obtained as $\Psi_0(x_1, x_2) = \phi(X)\psi(x)$ and on the right-hand side of Fig. 2.1 we show its two particle probability density, $|\Psi_0(x_1, x_2)|^2$. The repulsive interaction between the particles is evident as a zero line along the diagonal in the probability density when $x_1 = x_2$. For a finite trap separation the particles become localised in their respective traps and the two particle probability density moves to occupy the upper left-hand side quadrant.

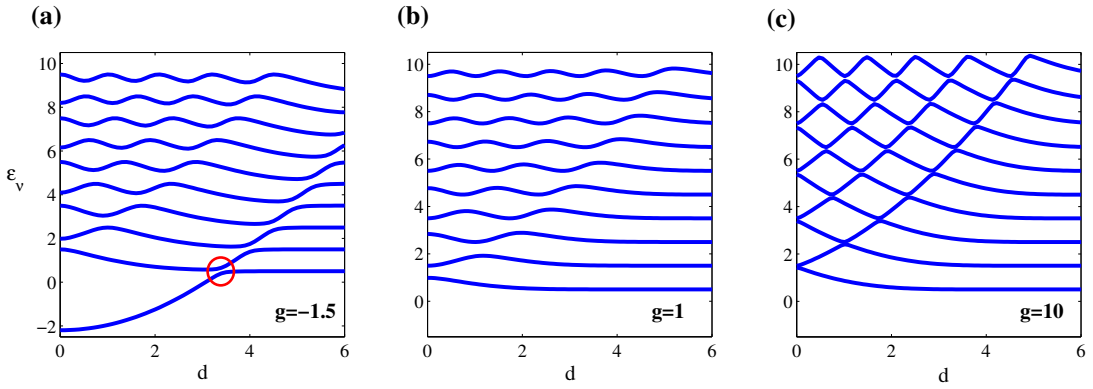


FIGURE 2.3: Energy versus distance d between the traps for different values of the scaled interaction strength **(a)** $g = -1.5$, **(b)** $g = 1$ and **(c)** $g = 10$. For large values of g the energy levels become degenerate at $d = 0$. For finite distances between the traps resonances appear whenever two levels approach each other. For a repulsive interaction, the ground state is not affected by such resonances, however, for an attractive interaction, a resonance can be observed (red circle in panel **(a)**).

2.3 Entanglement

In the case of the two interacting atoms at zero temperature one can calculate the reduced single-particle density matrix (RSPDM) $\rho_1(x, x')$, which is determined as the kernel of the reduced density operator in configuration space

$$\rho_1(x, x') = \int_{-\infty}^{\infty} \Psi_0(x, x_2)\Psi_0^*(x', x_2)dx_2 \ . \tag{2.26}$$

The RSPDM contains important information about the correlations and coherences present in the system through its off diagonal terms. This can be seen in Fig. 2.5 where the RSPDM is plotted for two atoms with interaction strength $g = 10$. The first panel depicts the situation for perfectly overlapping traps and the presence of the off-diagonal terms shows the existing correlations stemming from the overlap of the individual single particle states. In the second panel in Fig. 2.5 the two traps are separated by $d = 0.5$ which breaks the symmetry in the RSPDM and results in a visible reduction of the off-diagonal long range order. The diagonal of the RSPDM represents the single particle density profile of the system and its eigenvectors are the natural orbitals of the composite state. In order to evaluate the von Neumann entropy Eq.(2.3) we need the eigenvalues λ_i of $\rho_1(x, x')$, which are found by numerically solving the integral equation

$$\int_{-\infty}^{+\infty} \rho_1(x, x')\phi_i(x')dx' = \lambda_i\phi_i(x) \ , \tag{2.27}$$

where the $\phi_i(x)$ are the eigenstates associated with the λ_i. The von Neumann entropy follows as $S = -\sum_i \lambda_i \log_2 \lambda_i$. In Fig. 2.6 we show S as a function of both the trap

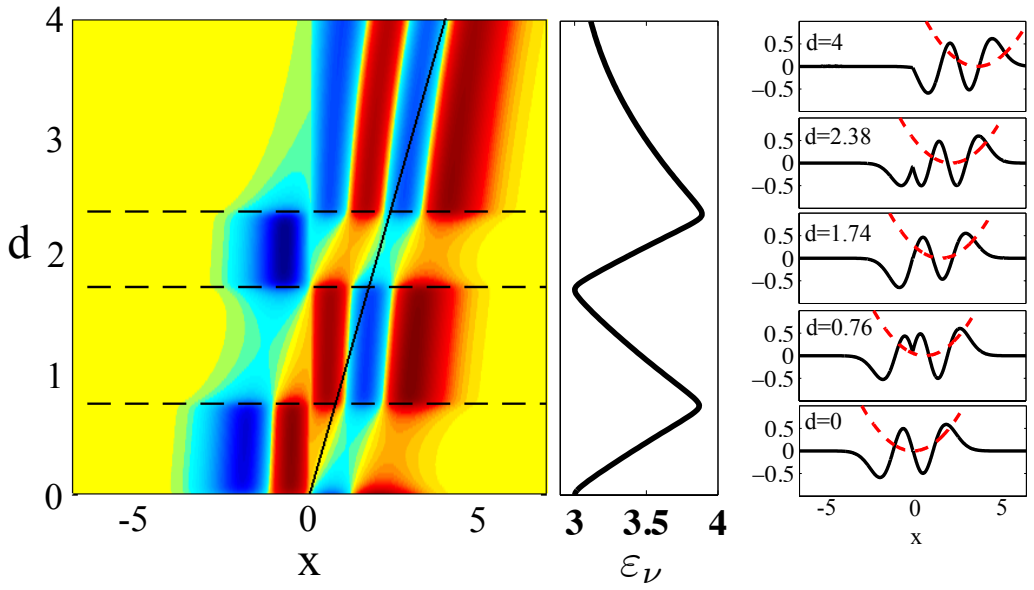


FIGURE 2.4: The relative wavefunction of the third excited state is plotted as a function of d in the left-hand side panel, where blue is negative intensity, red is positive intensity and yellow is zero. The solid line represents the centre of the harmonic trap as a function of d, and the dashed lines indicate the positions of the trap induced shape resonances. The energy ϵ_ν corresponding to the wavefunction is plotted in the middle panel, where the trap-induced shape resonances are visible as stationary points. In the right-most panel the wavefunction is plotted when the δ-function is at the origin of the harmonic trap, $d = 0$, and at the trap induced shape resonances, $d = 0.76, 1.74$ and 2.38. In the top-most figure the trap is moved far from the δ-function at $d = 4$. The height of the barrier is $g = 10$ in all cases.

distance d and the interaction strength g. For the case of a repulsive interaction, it can be seen from panel **(a)** that the von Neumann entropy decreases with increasing trap separation. This should be expected as the short range interaction becomes less important and the state of the system tends towards the product state of two non-interacting particles. Panel **(b)** shows the behaviour of S as a function of the interaction strength, revealing that, after an initial rise, S saturates to an asymptotic value that decreases as d grows. This is again due to the short-range nature of the interaction potential: as the interaction is ineffective for large d, the steady value of S would be smaller for increasing values of the separation. For attractive interactions the situation is slightly different and local maxima and saddle points in S can be observed at certain values of the trap separation [see Figs. 2.6**(c)** and **(d)**]. A comparison between Figs. 2.3 and 2.6**(c)** shows the correspondence of the appearance of these stationary points and the existence of the above-mentioned trap induced shape resonances for bound states in

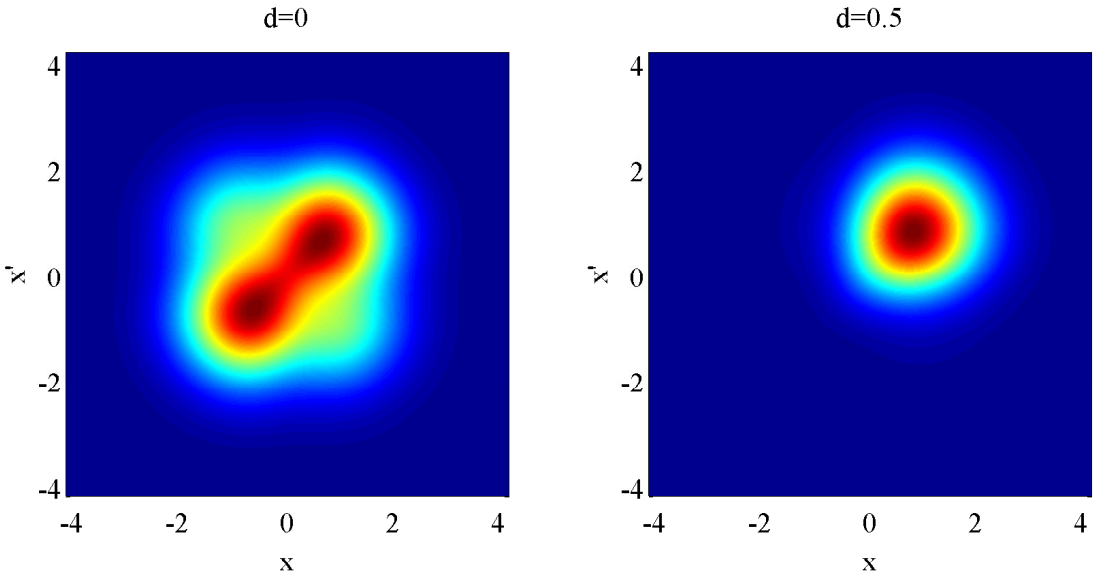


FIGURE 2.5: The RSPDM is plotted for $d = 0$ and $d = 0.5$ for $g = 10$. Even at small separation the off diagonals of the RSPDM are reduced indicating the short distance nature of entanglement.

the energy spectrum. In Fig. 2.7 the two particle wavefunction across this trap induced resonance is shown in the top row of figures. Around the resonance at $d = 3.25$ the state is seen to be localised by the strong attraction between the two traps and at $d = 3.75$ the particles are localised in their respective traps. However at the resonance at $d = 3.5$ the two particle state is spread between the two individual traps with a significant probability still in the centre of the system. This spatial uncertainty leads to the peak of von Neumann entropy in Fig. 2.6**(c)**. Note that, for a given value of d, comparatively smaller absolute values of g are required in the $g < 0$ case than in the repulsive one in order to achieve large values of S.

2.4 Calculation of the Wigner function and assessment of its negativity

We will now investigate the non-classical nature of the two-atom state in a much broader range of operative conditions, including finite temperature. In these situations the von Neumann entropy is not a good indicator of the correlations present as we are no longer dealing with pure states. For this reason, the main tool in our study will be the Wigner function [85] which is a quasi-probability distribution in phase space. The Wigner function describes the motion of a particle as it "jumps" from position x_1 to x_2, and much

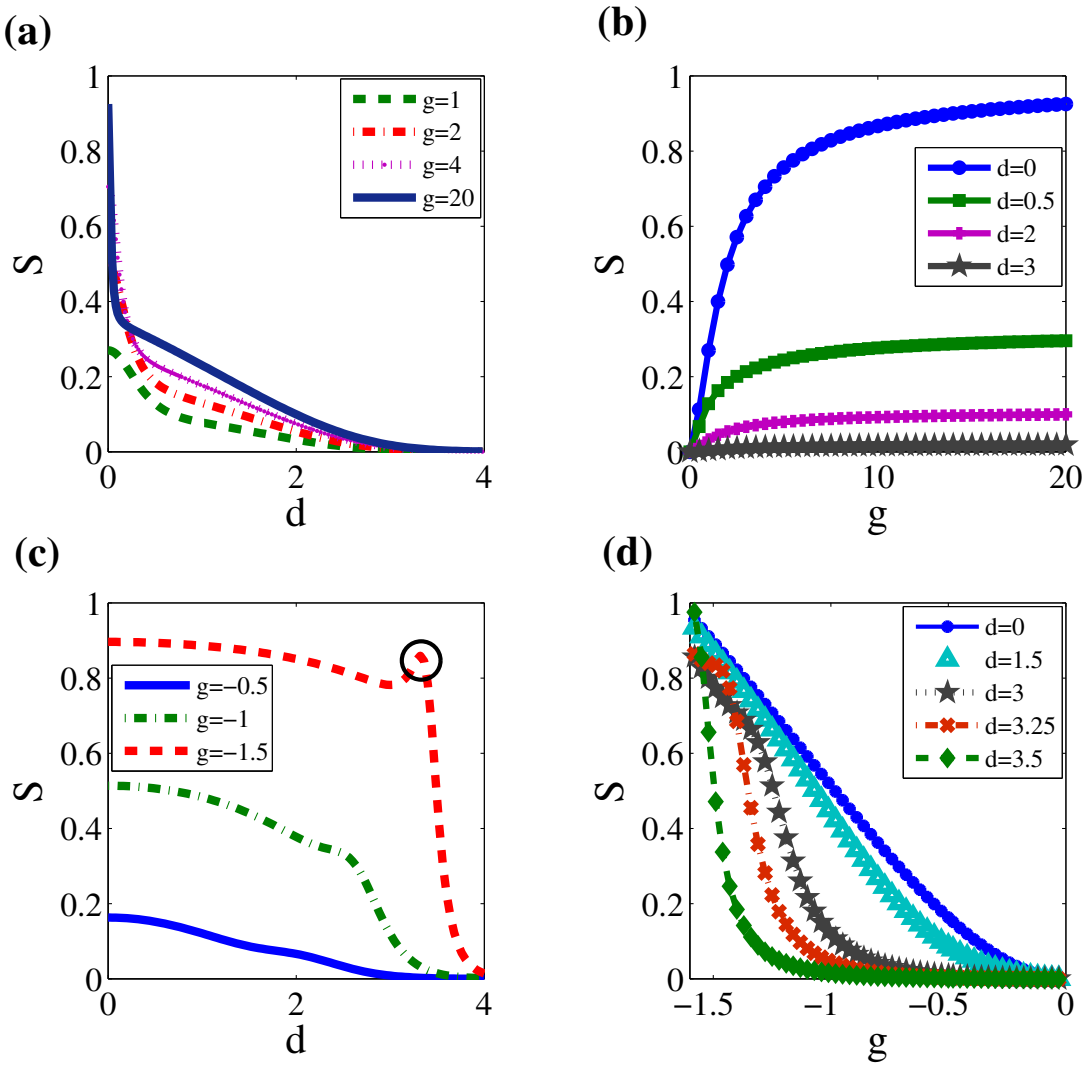


FIGURE 2.6: Von Neumann entropy of the ground state for repulsive [panels **(a)** and **(b)**] and attractive interaction [panels **(c)** and **(d)**]. Plots are shown for the von Neumann entropy versus trap separation, **(a)** and **(c)**, and von Neumann entropy versus particle interaction strength, **(b)** and **(d)**. The local maxima visible in **(c)** and **(d)** for certain values of d are connected to the appearance of shape induced resonances in the energy spectrum, as seen in Fig. 2.3**(a)** for $d \approx 3.5$.

like a quantum jump in the energy levels of an atom we can define the strength of this transition by $\langle x_1|\hat{\rho}|x_2\rangle$ where $\hat{\rho}$ is the density operator. Let us now introduce new co-ordinates, the centre of mass $x = (x_1 + x_2)/2$ and the distance between the jump as $\xi = x_1 - x_2$. The motion of the atom is given by $\langle x + \frac{1}{2}\xi|\hat{\rho}|x - \frac{1}{2}\xi\rangle$ and to construct the full motion of the atom in phase space we have to connect the momentum p with ξ which is achieved by a Fourier transform with respect to the jump distance. The result is the Wigner distribution function for a single atom:

$$W(x,p) = \frac{1}{2\pi\hbar}\int_{-\infty}^{\infty} d\xi\, e^{\left(-\frac{i}{\hbar}p\xi\right)} \left\langle x + \frac{1}{2}\xi \middle| \hat{\rho} \middle| x - \frac{1}{2}\xi \right\rangle . \tag{2.28}$$

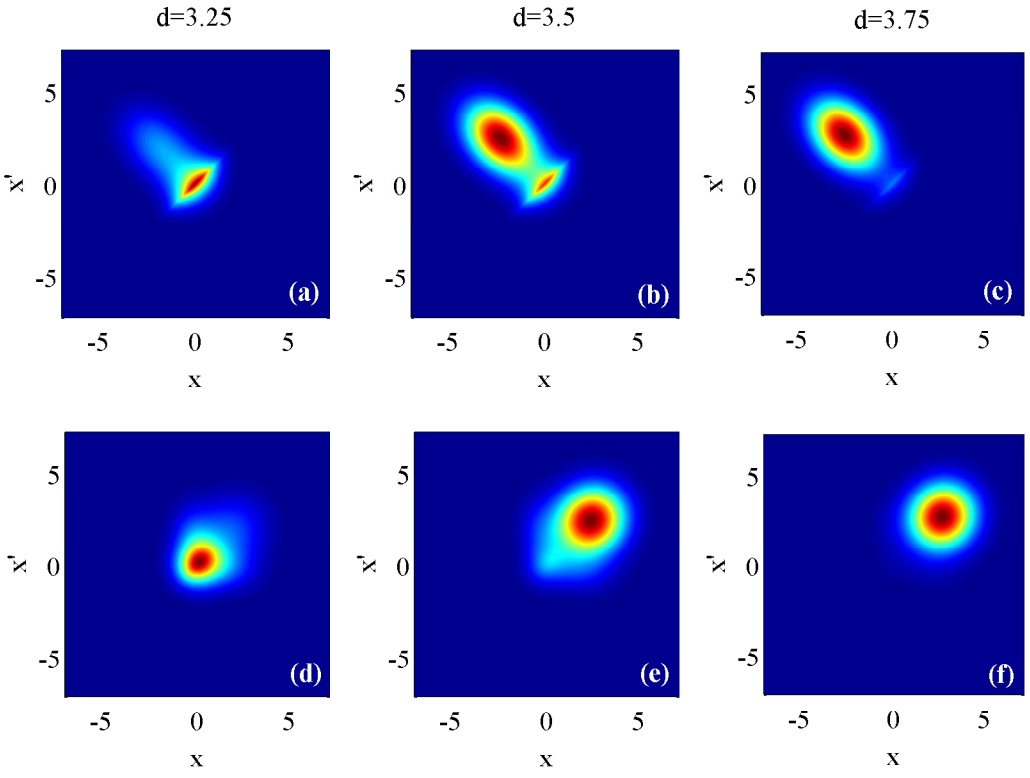


FIGURE 2.7: Top panels: the two particle wavefunction is plotted for different trap distances for $g = -1.5$. The strong attractive interaction between the particles ensures that they stay bonded even with the traps separated by $d = 3.25$. At $d = 3.5$ the von Neumann entropy peaks at a local maximum caused by trap induced shape resonances. At this point the particles begin to become localised in their respective wells, however due to the attractive interaction there is still a density peak between the separate traps. At $d = 3.75$ the force from the trapping potential overcomes that of the interaction the particles are more likely found in their respective traps where the overlap between the two particles is low and the von Neumann entropy approaches zero. Bottom panels: The corresponding RSPDM is plotted at each distance.

which has the property

$$\int_{-\infty}^{\infty} dx \int_{-\infty}^{\infty} dp\, W(x,p) = 1\ . \tag{2.29}$$

The Wigner function is therefore a Fourier transform which maps phase-space functions to Hilbert space operators [84]. Also by integrating out the momenta or positions one can calculate the marginal spatial or momentum distributions of the state, respectively. In the case of a pure state $\hat{\rho} = |\psi\rangle\langle\psi|$ the Wigner function reduces to

$$W(x,p) = \frac{1}{2\pi\hbar} \int_{-\infty}^{\infty} d\xi\, e^{\left(-\frac{i}{\hbar}p\xi\right)} \psi^* \left(x - \frac{1}{2}\xi\right) \psi \left(x + \frac{1}{2}\xi\right), \tag{2.30}$$

where $\langle x + \frac{1}{2}\xi|\psi\rangle = \psi(x + \frac{1}{2}\xi)$ is the state $|\psi\rangle$ projected onto the position coordinate. Hence the Wigner function is the Fourier transform of the shifted position wave functions

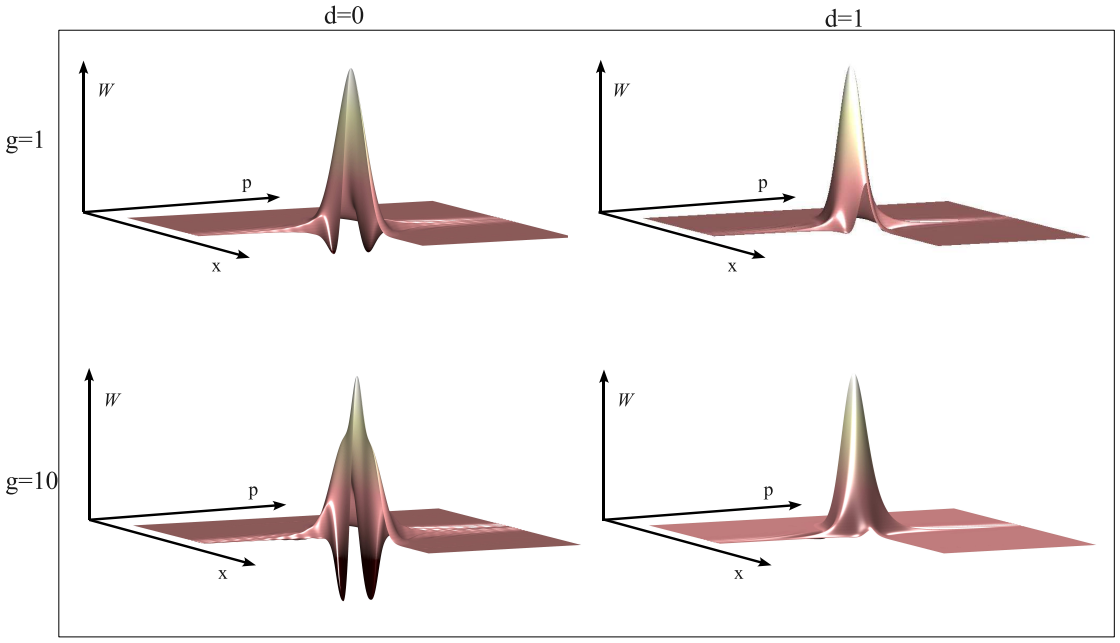


FIGURE 2.8: Wigner function for an interaction strength of $g = 1$ and $g = 10$ at trap separations $d = 0$ and $d = 1$. A quadrant is removed from the plot to show the negative parts of the Wigner distribution which is symmetric about $p = 0$. For $g = 1$ a reduction in the negative part of the Wigner function is evident for $d = 1$ compared to $d = 0$. For $g = 10$ the large negative contribution and sharp peak are indicative of the larger interaction strength at $d = 0$. For $d = 1$ the negative volume is significantly less.

of the state $|\psi\rangle$.

For the specific case of two particles, the Wigner function depends on the position and momentum variables x_j and p_j $(j = 1, 2)$ and is defined as [85]

$$W(x_1, p_1; x_2, p_2) = \int d\xi d\varsigma \frac{e^{-\frac{i}{\hbar}p_1\xi - \frac{i}{\hbar}p_2\varsigma}}{4\pi^2\hbar^2} \rho\left(x_1 + \frac{\xi}{2}, x_2 + \frac{\varsigma}{2}, x_1 - \frac{\xi}{2}, x_2 - \frac{\varsigma}{2}\right). \tag{2.31}$$

It is straightforward to include the effects of a non-zero temperature by weighting the higher-order states of the two-atom spectrum with the appropriate Boltzmann factors, $P_{n,\sigma} = \frac{1}{\mathcal{Z}} e^{\frac{-E_{n,\sigma}}{k_B T}}$, where the $E_{n,\sigma}$ are the energies of the atomic eigenstates identified by the centre-of-mass and relative-motion quantum numbers n and σ, respectively. Moreover, we have introduced the equilibrium temperature of the system T, the Boltzmann constant k_B and the partition function $\mathcal{Z}$. We thus get

$$W(\alpha; \beta) = \sum_{n}^{\infty} \sum_{\sigma}^{\infty} P_{n,\sigma} W_{n,\sigma}(\alpha; \beta), \tag{2.32}$$

where, for easiness of notation, we have written the Wigner function in terms of the two quadrature variables $\alpha = (x_1 + ip_1)/\sqrt{2}$ and $\beta = (x_2 + ip_2)/\sqrt{2}$.

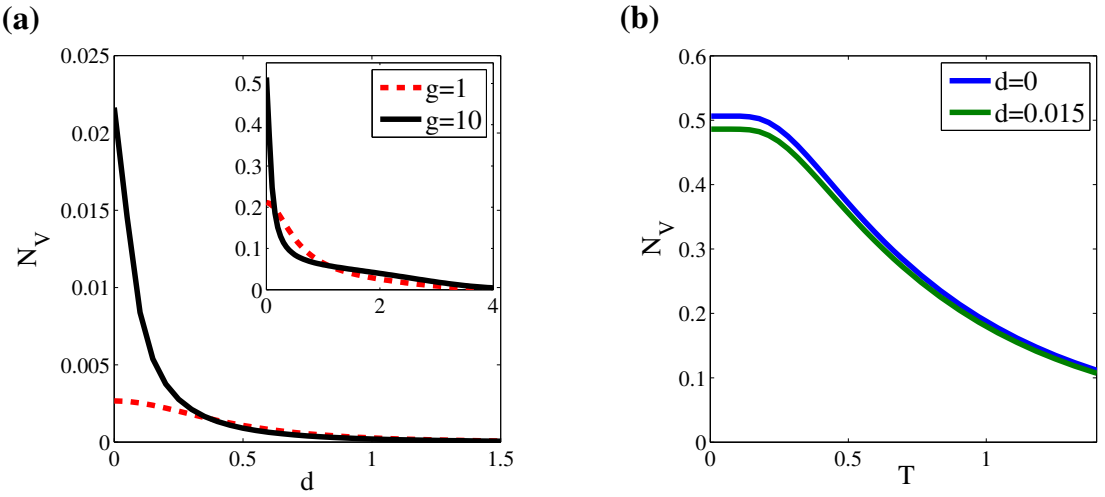


FIGURE 2.9: Panel **(a)** shows the negative volume of the complete Wigner distribution at zero temperature as a function of d. The inset shows N_V when only considering the contribution to the Wigner function associated with the relative part of the problem. Panel **(b)** shows the negative volume against increasing temperature (measured in units of $\hbar\omega/k_B$) for the relative part of the Wigner distribution with an interaction strength of $g = 10$.

2.4.1 Negative volume of the Wigner function

The appearance of negative values in the Wigner function of a system is a strong indication of non-classicality of the associated state, since in this case $W(\alpha;\beta)$ cannot be interpreted as a classical probability distribution describing a state in the phase space. Starting from such premises, Kenfack and Zyczkowski have proposed to use the volume occupied by the negative regions of $W(\alpha;\beta)$ as a quantitative indicator for non-classicality [86]. Such a (dimensionless) figure of merit can be evaluated as

$$N_V = \frac{1}{2}\left(\int_\Omega |W(\alpha;\beta)|d\Omega - 1\right) , \tag{2.33}$$

with Ω being the whole phase-space and $d\Omega = dx_1 dx_2 dp_1 dp_2$. Note that in our case the centre-of-mass part of the wavefunction does not depend on the interaction between the particles. Therefore, it does not contribute to the degree of non-classicality and in Fig. 2.8 we show the Wigner functions associated with only the relative part of our problem for two different values of g and d. Negative parts are clearly visible for small values of d and become more prominent for increasing interaction strength. This is also visible in Fig. 2.9**(a)**, where N_V is plotted against d. However, the degree of non-classicality decreases faster for a larger interaction strength when the traps are moved apart. The temperature dependence of the negative volume is displayed in Fig. 2.9**(b)**, where one can see a very fast decrease once the system is able to access states beyond the ground state.

2.5 Testing non-locality in phase space

The results of the previous Section indicate that a considerable degree of non-classicality might be set in the state of the external degrees of freedom of the two trapped atoms, resilient to some extent to the effects of finite temperature. Moreover, as it should also be clear from Eq. (2.12), our study has shown the evident non-Gaussian nature of the atomic state (as witnessed by the features of the Wigner function). While correlations in Gaussian states are well and easily characterized, we face the lack of necessary and sufficient criteria for the quantification of entanglement in non-Gaussian states [87]. In fact, the available entanglement measures for CV states are based on the use of the negativity of partial transposition criterion formulated in terms of covariance matrices, which carry exact information on the state of a system only in the Gaussian scenario [88]. As we would like to provide a feasible test for entanglement in the state of the system at hand we will in the following assess non-classicality in terms of non-locality probed in the phase-space of the system studied here.

We thus consider the CV version of CHSH inequality developed in Ref. [90] and will explore the key points for completeness. It is well known that the Wigner function calculated at the origin of phase space is equivalent to the expectation value $W(\alpha = 0; \beta = 0) = \frac{4}{\pi^2}\langle \hat{\Pi}_1 \otimes \hat{\Pi}_2 \rangle$, where $\hat{\Pi}_j$ is the parity operator for mode $j = 1, 2$ [89]. The total Wigner function can therefore be written by using *displaced parity operators* as [89]

$$W(\alpha;\beta) = \frac{4}{\pi^2}\langle \hat{D}_1(\alpha)\hat{\Pi}_1\hat{D}_1^\dagger(\alpha) \otimes \hat{D}_2(\beta)\hat{\Pi}_2\hat{D}_2^\dagger(\beta)\rangle, \tag{2.34}$$

where $\hat{D}_j(\alpha)$ is a displacement operator for mode j of amplitude α [88]. A CHSH-like function can then be built starting from the above as

$$\mathcal{B} = \frac{\pi^2}{4}[W(0;0) + W(\sqrt{\mathcal{J}};0) + W(0;-\sqrt{\mathcal{J}}) - W(\sqrt{\mathcal{J}};-\sqrt{\mathcal{J}})] \tag{2.35}$$

with $\mathcal{J}$ a positive constant. As shown above, local realistic theories impose $|\mathcal{B}| \leq 2$ [90] and any value outside this range indicates non-local behaviour.

Equipped with these tools, we can now quantitatively study the non-locality in the state of our system. Using the Wigner function calculated in Sec. 2.4, we determine the violation of the CHSH inequality optimised over $\mathcal{J}$ and study the behaviour of $\mathcal{B}$ against the interaction strength between the particles and the distance between the traps. In Fig. 2.10**(a)** we show the numerically optimised values of $\mathcal{B}$ against d for various interaction strengths g and at zero temperature. Clearly, for short distances the violation of the local realistic bound is larger for strong interactions. The situation is somehow reversed at large distances, where weakly interacting atomic pairs appear to violate the

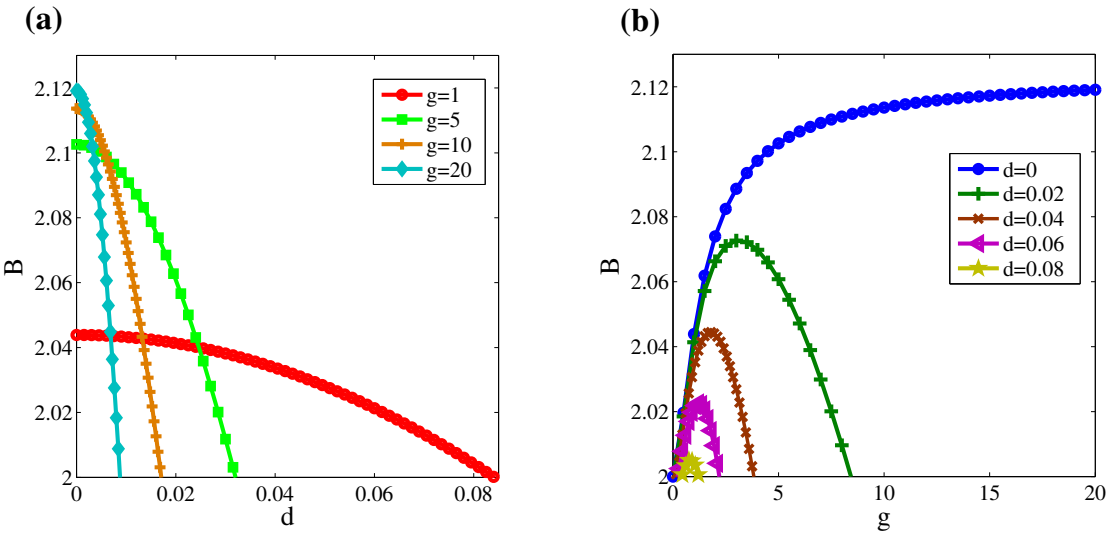


FIGURE 2.10: The violation of the CHSH inequality at $T = 0$ is shown in panel **(a)** against trap separation for various interaction strengths and in **(b)** versus g, for increasing trap separations.

CHSH inequality more significantly. Such an apparently counterintuitive result can be understood by reminding one that the one-dimensional interaction strength is inversely proportional to the one-dimensional scattering length (see Sec. 2.2): a lower value of g corresponds to a larger scattering length. This means that while the correlations stemming from the reduced dimension decay with increasing distance, the influence of the scattering length persists for larger values of d. Comparing these results to the von Neumann entropy shown in Fig. 2.6 it is evident that achieving a non-zero von Neumann entropy does not necessarily correspond to the violation of CHSH inequality, in qualitative agreement with the findings of Ref. [64]. In Fig. 2.10**(b)** we show $\mathcal{B}$ as a function of the interaction strength. The non-monotonic behaviour of the CHSH function against the interaction strength, as well as the disappearance of any violation at finite values of g and for $d \neq 0$, are striking. It can be understood by realising that the offset between the traps breaks the symmetry of the system and a large repulsive interaction between the particles results in less overlap and therefore less correlations in the phase space. Noticeably, although the CHSH inequality is only violated for $d \lesssim 0.08$, recent experiments involving optical lattices have demonstrated the possibility to off-set atomic trapping potentials with an accuracy of exactly this order of magnitude [91].

2.5.1 Finite Temperature

For the case of non-zero temperature we plot the violation of the CHSH inequality for two values of interaction strengths ($g = 1, 10$) in Fig. 2.11. The plot shows general trends of decay of the correlations with increasing temperature and distance, however one can note

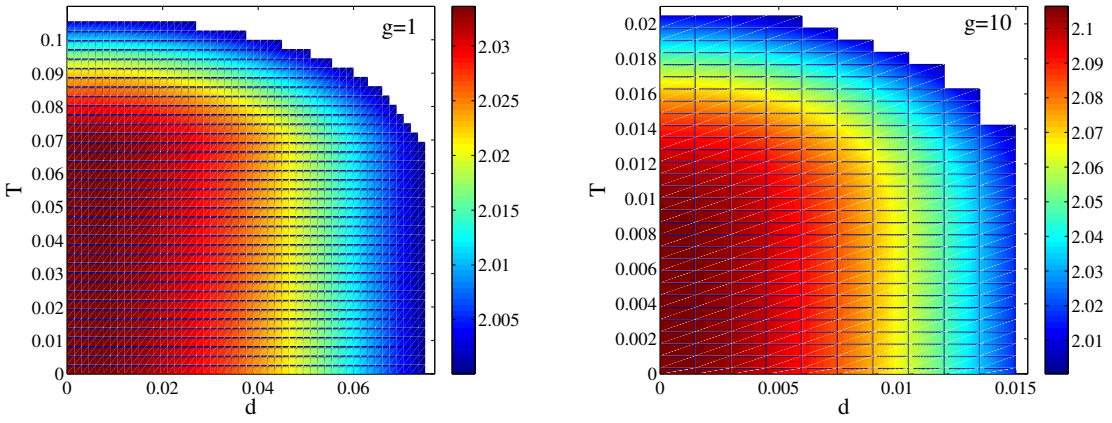


FIGURE 2.11: Degree of CHSH violation against trap-separation and temperature (in units of $\hbar\omega/k_B$) for interaction strengths of $g = 1$ and $g = 10$. The change in temperature has a greater impact on the two particles at greater interaction energies (note the different scalings in the two plots).

that for $g = 1$ the system is more resilient to the effects of an increasing temperature than in the stronger-interaction case because the separations between neighbouring energy levels is larger at low δ-barrier (*i.e.* small g's). At large g, this implies a greater probability to excite higher-energy modes at small temperature. Evidently, the violation of CHSH inequality becomes very sensitive to temperature variations once the thermal energy is comparable to the energy-level separation.

2.5.2 Detection Scheme

We now propose a strategy for the reconstruction of the atomic Wigner function for a non-locality test following the approach suggested by Lutterbach and Davidovich [92]. The key is mapping the information encoded in the external degree of freedom of one of the trapped atoms into a specific internal state of the atom itself, which can then be efficiently read out. For the sake of argument, let us for the moment address the case of a single atom and label the logical states of the qubit as $\{|\uparrow\rangle, |\downarrow\rangle\}$. Physically, they could be two quasi-degenerate metastable ground states of a three-level Λ-like model and transitions from each ground state to the excited level of the Λ model will induce motional state-dependent sidebands on $|\uparrow\rangle$ and $|\downarrow\rangle$. The transition between different motional states of the atom can thus be induced by properly tuned stimulated Raman passages connecting two different sidebands of the ground-state doublet, as described in [93], in a way so as to mimic the dynamics intertwining motional degrees of freedom and internal ones in trapped ions. Such processes can be performed with an almost ideal efficiency. Working in an appropriate Lamb-Dicke limit (where the recoil energy due to the *kicks* induced by the coupling between atomic levels and light is much smaller than

the ground-state energy of the motional mode), it is possible to relate the difference $P_\uparrow - P_\downarrow$ between the probability of finding the atom in $|\uparrow\rangle$ or $|\downarrow\rangle$, respectively, to the expectation value of the displaced parity operator and thus, in turn, to the value of the Wigner function at a given point of the phase space [92]. Such a difference in probability can be effectively measured by means of routinely implemented high-efficiency fluorescence light-based detection methods which is outlined in [94]. In order to reconstruct the two-atom Wigner function, it would be sufficient to collect signals from both the atoms undergoing similar reconstruction protocols and appropriately putting together the statistical data gathered. By using fluorescence cycles of different frequencies for each particle one can distinguish the signals collected, without the need of separating the corresponding traps by a large distance.

2.6 Effects of dissipation

Let us finally discuss the influence of a general loss mechanisms, one per atomic mode, that may affect the two-atom state due to finite-time coherence of the external degrees of freedom. Such a lossy process can be effectively modelled considering each atomic vibrational mode as in contact with a background bath of bosons (due, for instance, to mode-mode coupling induced by an-harmonicity of the traps or position-to-electric-field coupling induced by stray electromagnetic fields in the proximity of the trapped particles) [95]. Here we consider a simple *beam-splitter model* which mimics the losses in the detector as a result of mixing the individual modes of the two particle state with the bosonic bath. Assuming low temperature environments this allows us to describe them as two independent zero-T bosonic baths, each prepared in its collective vacuum state. We call A the environmental bath affecting mode 1 and B affecting mode 2. The Wigner function of the vacuum state of each is

$$W_0(\mu_k) = \frac{2}{\pi} e^{-2|\mu_k|^2} \quad (k = A, B), \tag{2.36}$$

where $\mu_k = \frac{x_k + i p_k}{\sqrt{2}}$ are the quadrature variables of the environmental modes. The interaction between the signal mode j and its environment is modelled as a mixing at a beam splitter having reflectivity η_k. For simplicity and without affecting the generality of our discussions, we assume the reflectivity to be equal in both modes, $\eta_k = \eta$. In phase space, the state of the signal mode after the interaction and after tracing over the environmental degrees of freedom is described by the convolution

$$\begin{aligned} W^\eta(x_1, x_2, p_1, p_2) \quad &= \int dx_A dx_B dp_A dp_B W(\tilde{x}_1, \tilde{p}_1, \tilde{x}_2, \tilde{p}_2) \\ &\quad \times W_0(\tilde{x}_A, \tilde{p}_A) W_0(\tilde{x}_B, \tilde{p}_B), \end{aligned} \tag{2.37}$$

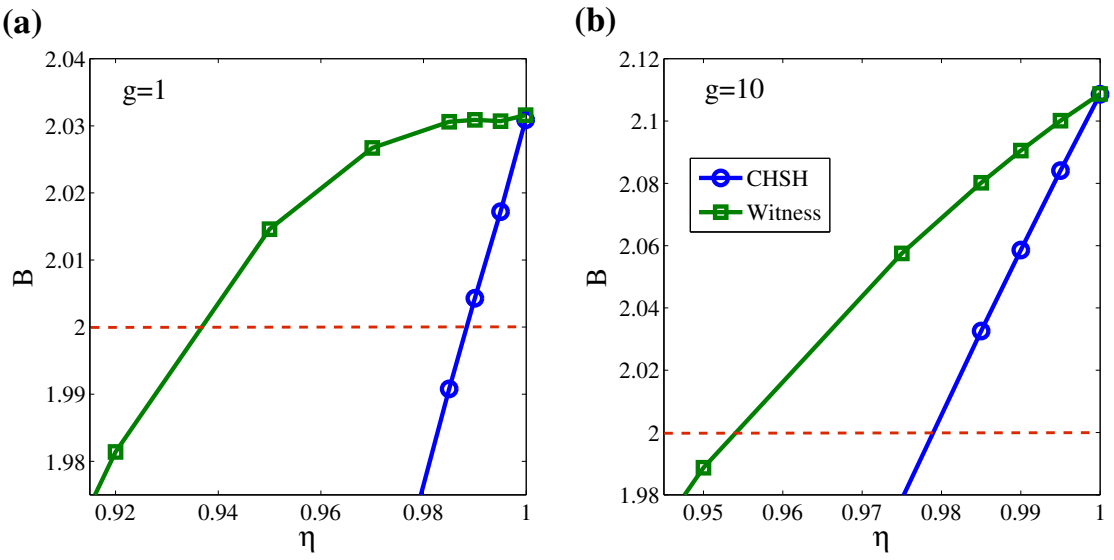


FIGURE 2.12: Plots of CHSH violation and entanglement witness for interaction strengths of $g = 1$ (panel **(a)**) and $g = 10$ (panel **(b)**) with inefficiency η. The violation of CHSH is seen to decay quickly as the detection becomes inefficient (blue lines), however the entanglement witness (green lines) shows the existence of entanglement for greater inefficiencies, with the lower value of g having more resilience to the losses.

where we have introduced the transformed variables

$$\tilde{x}_j = \sqrt{\eta}\, x_j - \sqrt{1-\eta}\, x_k, \quad \tilde{x}_k = \sqrt{\eta}\, x_k + \sqrt{1-\eta}\, x_j, \tag{2.38}$$

$$\tilde{p}_j = \sqrt{\eta}\, p_j - \sqrt{1-\eta}\, p_k, \quad \tilde{p}_k = \sqrt{\eta}\, p_k + \sqrt{1-\eta}\, p_j \tag{2.39}$$

and one should take $k = A$ (B) if $j = 1$ (2). Eq. (2.37) is evaluated numerically and used to test violation of the CHSH inequality against η. Needless to say, the effect of losses (or detection inefficiencies) is to reduce the degree of violation of the CHSH inequality, as shown by the solid blue lines in Fig. 2.12. The same trend highlighted before regarding resilience of non-locality properties for lower values of g is retrieved here.

It is therefore desirable to design viable strategies for a more robust analysis of non-locality. A step in this direction has been recently performed in Ref. [96] with the proposal of a robust entanglement witness based on a CHSH-like inequality that shows resilience with respect to losses/detection inefficiencies of the form considered here. Following the derivation provided by Lee *et al.* [96], one can see that for separable bipartite

states and loss rate/detection inefficiency η, the following inequalities hold

$$\begin{aligned} |\langle \mathcal{W}_{\eta>\frac{1}{2}} \rangle| \quad &= |\tfrac{\pi^2}{4\eta^2}[W^\eta(0,0)+W^\eta(0,-\sqrt{\mathcal{J}})+W^\eta(\sqrt{\mathcal{J}},0)-W^\eta(\sqrt{\mathcal{J}},-\sqrt{\mathcal{J}})] \\ &\qquad +\tfrac{\pi(\eta-1)}{\eta^2}[W^\eta_\alpha(0)+W^\eta_\beta(0)]+2(1-\tfrac{1}{\eta})^2| \leq 2, \\ |\langle \mathcal{W}_{\eta\leq\frac{1}{2}} \rangle| \quad &= |\pi^2[W^\eta(0,0)+W^\eta(0,-\sqrt{\mathcal{J}})+W^\eta(\sqrt{\mathcal{J}},0)-W^\eta(\sqrt{\mathcal{J}},-\sqrt{\mathcal{J}})] \\ &\qquad -2\pi[W^\eta_1(0)+W^\eta_2(0)]+2| \leq 2. \end{aligned} \tag{2.40}$$

Here, $W^\eta(a,b)$ is the two-mode Wigner function calculated in Eq. (2.37) and $W^\eta_{1,2}$ are its single-mode marginals. For the case of perfect detectors ($\eta = 1$) the inequality becomes equivalent to Eq. (2.35). It is apparent that any violation of this inequality for $\eta < 1$ ensures the violation of the CHSH-inequality in the presence of the unitary case as well, thus such witnesses can be used effectively for detecting entanglement in the presence of noise. From the results shown in Fig. 2.12 one can see that, while the CHSH inequality violation is lost for $\eta = 0.98$ at $g = 10$, the entanglement witness still violates it at $\eta \simeq 0.95$, which is a small yet significant improvement. It is important to notice that current avalanche photodiodes used to collect fluorescence have quantum efficiencies exactly in this range. Interestingly the entanglement witness for $g = 1$ is violated for smaller η, echoing the trend noticed for the CHSH at zero and non-zero temperature: lower interaction strengths give rise to states more resilient to influences from the environment.

2.7 Conclusions

We have investigated the non-classical correlations of two interacting bosons in different trapping potentials. The advantage of this model is the analyticity of the solution which is readily obtained through factorising the Hamiltonian and solving for the individual Hamiltonians. In this system the role of trap-induced shape resonances play an important role in the energy spectra and the entanglement properties of the composite system. We have found that the von Neumann entropy shows strong correlations at zero temperature for a variety of interaction strengths and trap displacements. We have also shown the violation of local realistic theories and an interesting and rather counterintuitive behavior has been observed, even at non-zero temperature, for the whole range of interaction strengths analysed. We have related the multiple facets of both the revealed non-locality and the von Neumann entropy to the details of the coupling model used in this work and the corresponding spectrum of the system.

Finally, we have included the effects of general non-idealities (such as dissipative losses affecting the motional degrees of freedom of the trapped atoms or inefficient detectors),

demonstrating the fragility of the atomic non-locality. In order to circumvent such a hindrance, we have shown that some improvements can come from the use of a recently proposed entanglement witness that fits very well with the general approach put forward here.

2.8 Outlook

Further studies on non-classical correlations in two particle systems in higher dimensions would be fruitful as the relation between the scattering length and interaction strength changes and trap induced shape resonances are still present. Furthermore, the effect of angular momentum on the bipartite correlations would be an interesting extension to this study especially when one considers using an asymmetric three dimensional trap.

Chapter 3

Coherence and dynamics of a Tonks-Girardeau gas

3.1 Introduction

Strong interactions entail strong correlations which have been discussed in Chapter 2 in terms of entanglement and non-locality of a bi-partite system. In this Chapter we will look at the collective excitations of a gas of more than two atoms and will describe the many-body phenomena which are present. We will concentrate on the effect that an impurity has on a Tonks-Girardeau (TG) gas, which has been the focus recently of interesting theoretical [97, 98] and experimental work [99]. A number of studies in this direction already exist in the literature, in which the impurity is modelled using a δ-function pseudo-potential [97, 100–104]. These studies have primarily focused on perturbations fixed at the origin and here we introduce a versatile analytical model which can be used to describe the TG gas in the presence of a perturbation of arbitrary strength at any position in a harmonic trap. In addition to describing a static impurity, this model can be interpreted as the limiting case of a split, asymmetric double well trap which may be realized using a sharply focused laser beam detuned from the atomic transition. The ability to position the impurity at any point in the harmonic trap allows us to probe the TG gas and study the spatial properties of the gas such as its coherence. Following recent experimental studies focusing on the absence of thermalisation due to the integrability of the underlying Hamiltonian [105] we investigate the dynamics of the

I would like to acknowledge the contribution of Dr. Krych and Dr. Idziaszek, who derived the solutions for the Hamiltonian in Section 3.2.1.

TG gas after sudden removal of the impurity and we are able to observe periodic revivals of a local density dip.

3.2 The Tonks-Girardeau gas

In Chapter 1 the ability to reduce the dimensions of ultracold gases in optical lattices was discussed [8, 10, 105, 106], and the strongly interacting TG regime was introduced. This topic will be briefly discussed again here. A gas of N bosons in a quasi one-dimensional potential can be approximated by the Hamiltonian

$$\mathcal{H} = \sum_{n=1}^{N} \left[-\frac{\hbar^2}{2m}\frac{\partial^2}{\partial x_n^2} + V_{ext}(x_n) \right] + g_{1D} \sum_{i<j} \delta(|x_i - x_j|) \,, \tag{3.1}$$

where m is the mass of the particles, V_{ext} is the trapping potential and g_{1D} is the 1D interaction strength [107]. This Hamiltonian describes an inhomogeneous Lieb-Liniger gas, which in the strongly repulsive limit $g_{1D} \to \infty$, can be solved by using the Fermi-Bose mapping theorem [7], thereby mapping it to a system of spinless fermions. The basic idea is to replace the interaction term in Eq. (3.1) with a boundary condition on the allowed bosonic wave-function

$$\Psi_B(x_1, x_2, \ldots, x_n) = 0 \quad \text{if} \quad |x_i - x_j| = 0 \,, \tag{3.2}$$

for $i \neq j$ and $1 \leq i \leq\ j \leq N$. Such a constraint is automatically fullfilled by calculating the wave-function using a Slater determinant

$$\Psi_F(x_1, x_2, \ldots, x_N) = \frac{1}{\sqrt{N!}} \det_{(n,j)=(0,1)}^{(N-1,N)} \psi_n(x_j) \,, \tag{3.3}$$

where the ψ_n are the single particle eigenstates of the system. Since the wave-function resulting from the process is anti-symmetric (fermionic), one has to finally symmetrise it using [7]

$$A(x_1, \ldots, x_N) = \prod_{1 \leq i < j \leq N} \mathrm{sgn}(x_i - x_j) \,, \tag{3.4}$$

which gives

$$\Psi_B(x_1, \ldots, x_N) = A(x_1, \ldots, x_N)\Psi_F(x_1, \ldots, x_N) \,. \tag{3.5}$$

For the ground state, which will be the focus of this Chapter, the mapping simply reduces to the absolute value of the fermionic wavefunction

$$\Psi_B(x_1, \ldots, x_N) = |\Psi_F(x_1, \ldots, x_N)| \,. \tag{3.6}$$

3.2.1 Single particle solutions

To apply the mapping mechanism and calculate the Slater determinant, Eq. (3.3), one needs to know the single particle eigenstates of the system under consideration. Here we will investigate a TG gas trapped in a harmonic trap potential of frequency ω, that is split asymmetrically by a tunable δ-perturbation of strength γ at a distance d from the centre of the trap,

$$V_{ext}(x) = \frac{1}{2}m\omega^2 x^2 + \gamma\delta(x-d)\ . \tag{3.7}$$

The limit $d = 0$ for this model is well known and has been studied extensively in recent years [67, 100, 102, 103].

The single particle Schrödinger equation for the potential Eq. (3.7) is

$$\left(\frac{-\hbar^2}{2m}\frac{d^2}{dx^2} + \frac{1}{2}m\omega^2 x^2 + \gamma\delta(x-d)\right)\psi(x) = \epsilon_\nu\psi(x)\ , \tag{3.8}$$

where the energies are given by $\epsilon_\nu = (\nu + \frac{1}{2})\hbar\omega$. Let us rescale all of the units in terms of the undisturbed ($\gamma = 0$) trap length $a = \sqrt{\frac{\hbar}{m\omega}}$ and energy $\hbar\omega$. In this way Eq. (3.8) can be rewritten as

$$\left(\frac{d^2}{dx^2} + \nu + \frac{1}{2} - \frac{x^2}{2} - \kappa\delta(x-d)\right)\psi(x) = 0, \tag{3.9}$$

where $\kappa = \gamma a/(\hbar\omega)$ is the re-normalised strength of the δ-barrier. The solutions of Eq.(3.9) are parabolic cylinder functions which must obey continuity conditions at the position of the δ-function and are equivalent to those used for the relative coordinate of two interacting particles in separate traps treated in Chapter 2,

$$\psi = \mathcal{N}\left(D_\nu(-x)\theta(d-x) + \frac{D_\nu(d)}{D_\nu(-d)}D_\nu(x)\theta(x-d)\right)\ . \tag{3.10}$$

Here $\mathcal{N}$ is the normalisation constant and $\theta(x)$ is the Heaviside step function. The associated energies are found by solving the transcendental equation

$$\nu\Big[D_{\nu-1}(-d)D_\nu(d) + D_{\nu-1}(d)D_\nu(-d)\Big] = 2\kappa D_\nu(-d)D_\nu(d)\ , \tag{3.11}$$

for the solutions that are non-zero at the δ-potential and

$$\frac{D_\nu(d)}{D_\nu(-d)}\nu D_{\nu-1}(-d) + \nu D_{\nu-1}(d) = 0\ , \tag{3.12}$$

for solutions that are zero at the δ-function. The solutions of the latter are simply the harmonic oscillator wavefunctions that vanish at $x = d$. This system and its solution

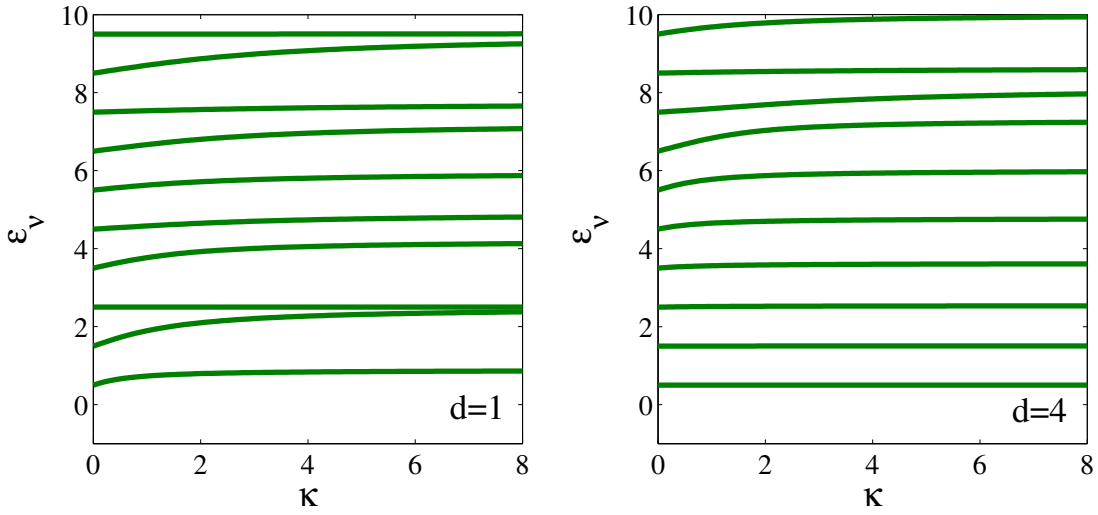


FIGURE 3.1: The energy spectrum of a harmonically trapped particle in the presence of δ-like perturbation at position $d = 1$ and $d = 4$, as a function of the strength of the perturbation κ.

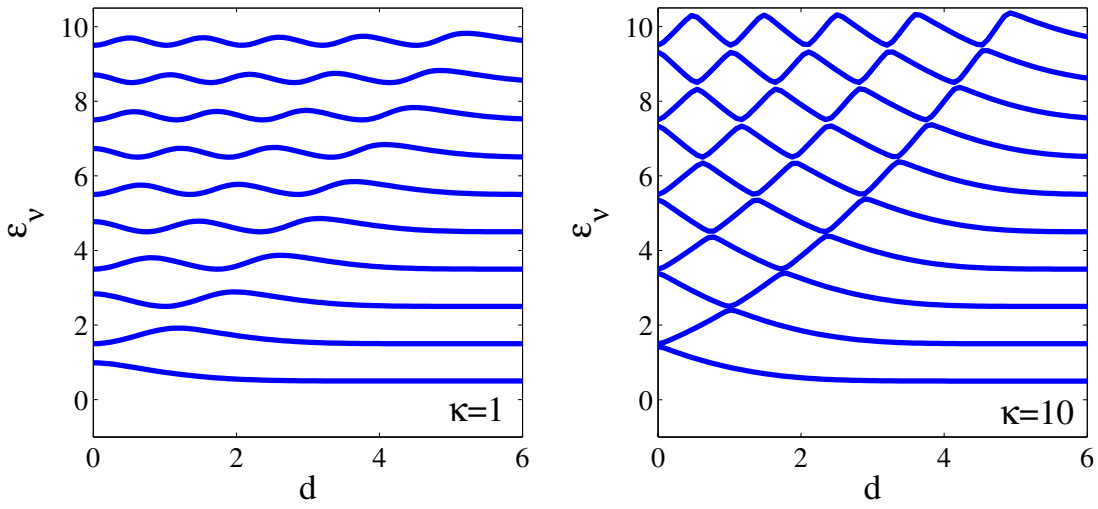


FIGURE 3.2: The energy spectrum of a harmonically trapped particle in the presence of δ-like perturbation with strength $\kappa = 1$ and $\kappa = 10$, as a function of d. Trap induced shape resonances exist at the positions of avoided crossings in the energy spectrum.

have been extensively discussed already in Chapter 2 and we refer the reader to Section 2.2 for a detailed explanation.

In Figs. 3.1 and 3.2 we show the energy spectrum as a function of d and κ, respectively. The presence of the perturbation introduces a non trivial structure and in general leads to an increase of the state's energy for $\kappa > 0$. In Fig. 3.1 it can be seen that the energy approaches a constant value at sufficiently large κ and in Fig. 3.2 a number of oscillations are observed which increase in number for higher order states. The four

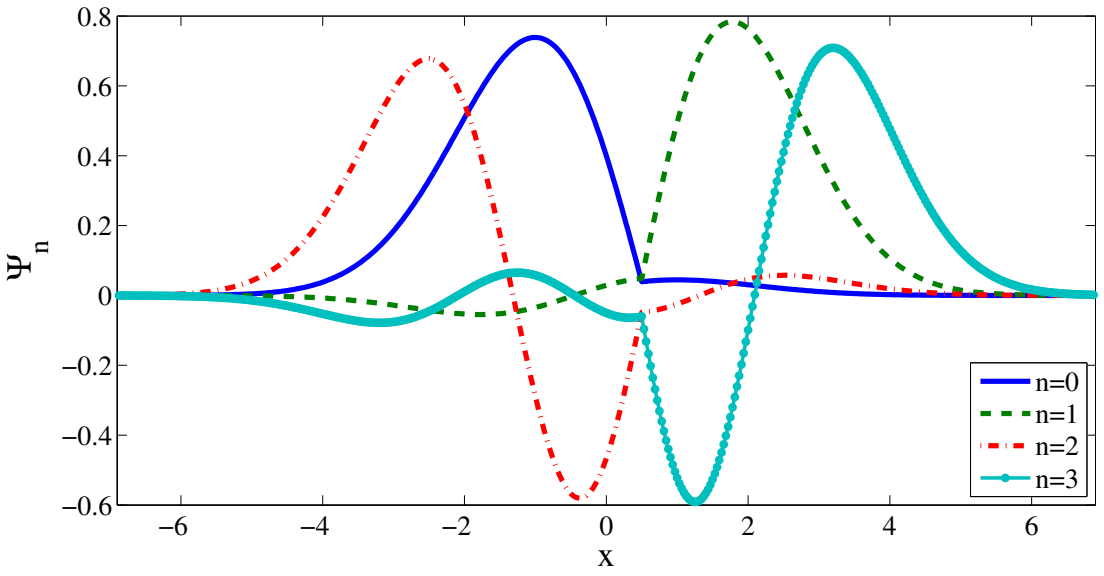


FIGURE 3.3: The four lowest energy eigenfunctions of a particle in a harmonic potential with a repulsive δ-function located at $d = 0.5$ of strength $\kappa = 10$

lowest lying eigenfunctions for $d = 0.5$ and $\kappa = 10$ are shown in Fig. 3.3. It can be seen that the presence of the delta potential results in an abrupt change in the slope of the wavefunction at the position of the δ-function and that the states are already highly localised on one side of the impurity for $\kappa = 10$.

3.3 Static and Dynamic Properties

3.3.1 Single Particle Density Profile

The single particle density is one of the most important observables for ultracold quantum gases. In the TG regime one can obtain it, even time-dependently, from the spectrum of underlying single particle Hamiltonian as [108]

$$\begin{aligned}\rho(x,t) &= N\int_{-\infty}^{+\infty}|\Psi_B(x,x_2,\ldots,x_N;t)|^2 dx_2\ldots dx_N \\ &= \sum_{n=0}^{N-1}|\psi_n(x,t)|^2\,,\end{aligned} \tag{3.13}$$

where we have adopted the convention of labeling the first N eigenfunctions as $n = 0, 1, 2, \ldots (N-1)$.

In Fig. 3.4 we show the ground state density for a gas of 20 particles in a trap with an impurity of strength $\kappa = 10$ at three different positions in the trap. As expected, the δ-impurity creates a significant local dip in the density and has only minimal effect at

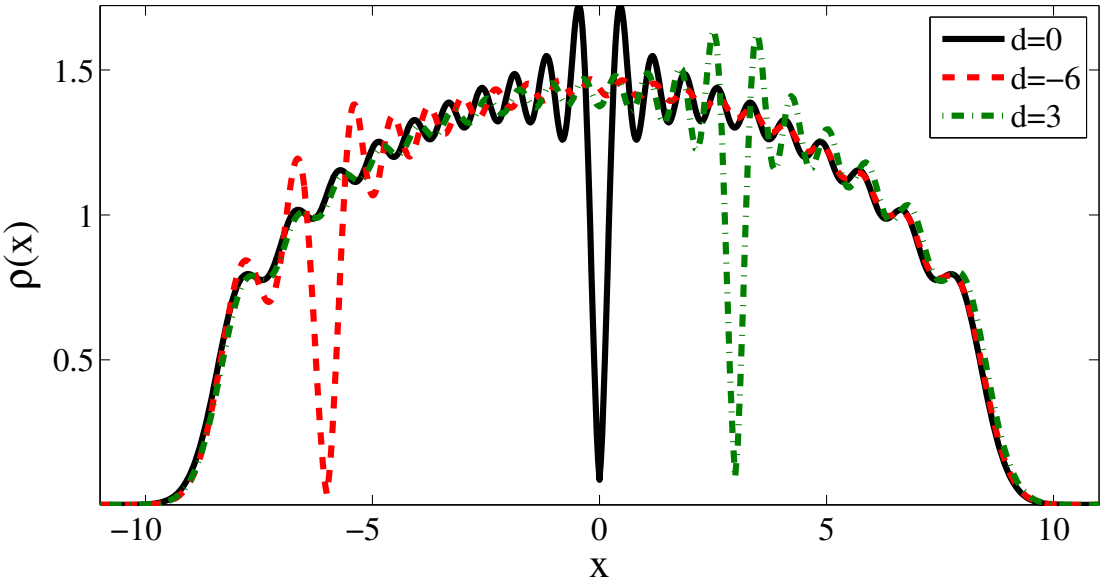


FIGURE 3.4: The ground state density of a harmonically trapped TG gas with 20 particles in equilibrium with a barrier of strength $\kappa = 10$, located at positions $d = 0, 3, -6$.

larger distances. The enhanced oscillations present around the position of the impurity are analogous to the Friedel oscillations which occur around an impurity in the surface charge density of a homogeneous electron gas [109]. As the electron gas obeys Fermi-Dirac statistics each state of the system can only be doubly occupied with electrons of opposite spin up to the Fermi level which is occupied by the most excited electron. When the electron gas encounters the impurity only electrons near the Fermi level can scatter as there are higher empty energy levels that they can occupy. This leads to a density modulation around the impurity which has the form $\rho(x) \approx \frac{\sin(2k_F x+\phi_d)}{x}$, where k_F is the Fermi wavevector and ϕ_d is a dimensionally-dependent phase [110].

In the following we investigate the dynamical properties of the TG gas in a split potential by examining a non-equilibrium situation created by the sudden removal of the impurity. In order to compute the time-dependent density of Eq. (3.13) one needs to employ a time dependent basis. We obtain this basis numerically by using the split operator method in the unperturbed harmonic trap [111]. Alternatively, one may simply employ the well known propagator for the harmonic oscillator to get the time dependent basis [112]. This can then be used to calculate the single particle density of Eq. (3.13).

In Fig. 3.5 we show $\rho(x,t)$ following the sudden removal of an impurity of strength $\kappa = 10$ located at $d = -6$. Time is scaled with respect to the inverse of the trap frequency ω. One can see that the density dip formed by the impurity vanishes almost instantaneously, however a mirror image of the dip appears after half a trap period, $t = \pi$, and then again disappears followed by a complete revival after one trap period,

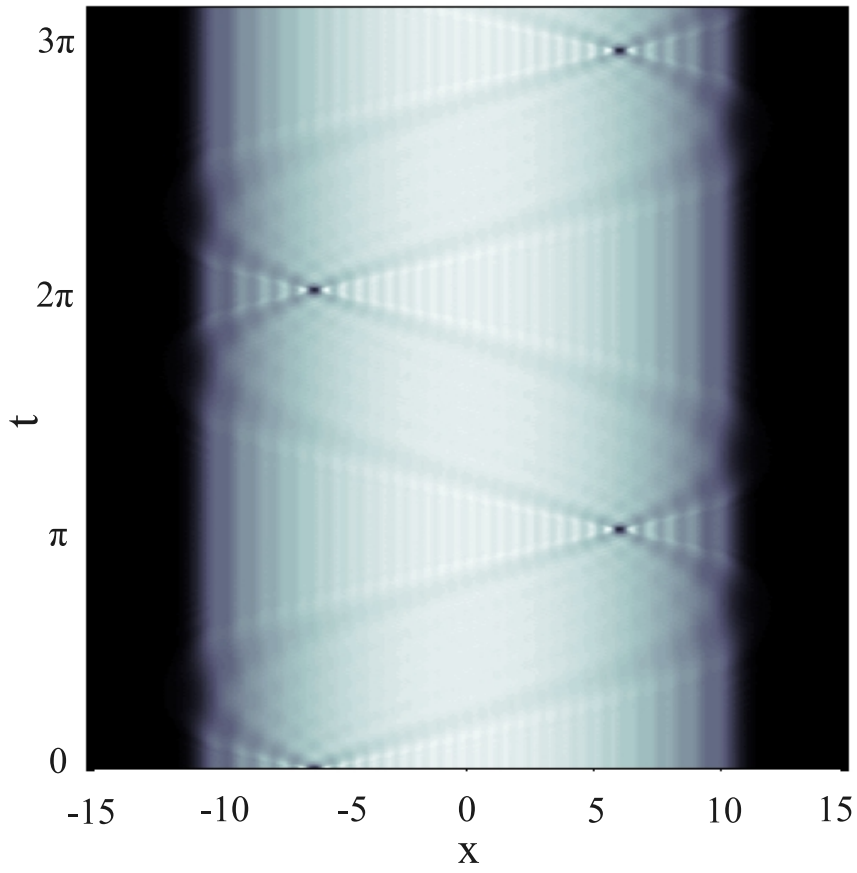


FIGURE 3.5: The time dependent single particle density of a harmonically trapped TG gas following the sudden removal of a δ barrier of strength $\kappa = 10$, located at position $d = -6$.

$t = 2\pi$. This effect is analogous to the Talbot effect from classical optics where periodic refocusing of a diffraction grating is expected to occur in the near field of a transmitted wave. In our situation the δ-function represents the most trivial form of a diffraction grating. The Talbot effect is a coherent *single* particle effect however here the effect occurs in a strongly correlated *many*-body system. This is because the system can be mapped onto free fermions, for which the single particle density is simply the sum of the squares of the single particle eigenfunctions, with each one undergoing its own coherent unitary evolution. In this picture, the occurrences can be explained by noting that all N eigenfunctions superimpose in phase again after every trap period and one finds that the density profile at odd multiples of π is a mirror image of the initial density profile at $t = 0$. It is also worth noting that in between these revivals the density exhibits an interesting fine structure. This is shown in a close up of the density for the time period $0 \leq t \leq \pi$ in Fig. 3.6. When the impurity is removed, the matter wave readjusts to the profile of a harmonically trapped gas by a relaxation of the Friedel oscillations. At $t = \pi/2$ there is complete relaxation of the oscillations, followed by a complete revival

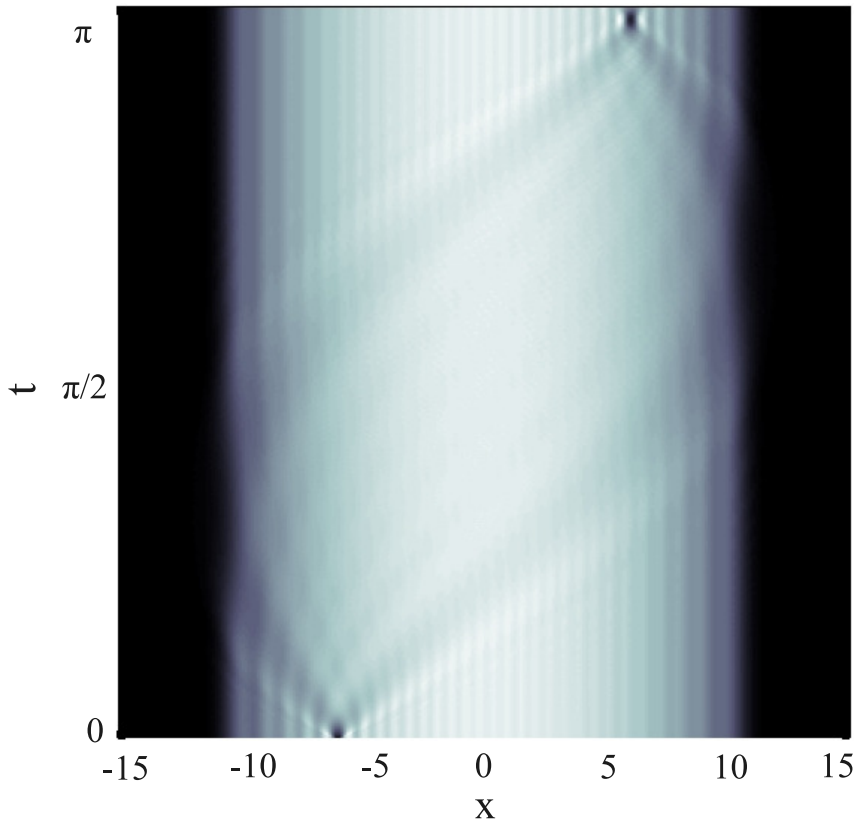


FIGURE 3.6: Detailed view of the time evolution of the single particle density for half a trap period.

at $t = \pi$. This is precisely the fine structure we see in between revivals of the density dip in Fig. 3.5.

3.3.2 Energy profile

It is interesting to consider the energy of the system as a function of the position of the impurity. Due to the Fermi-Bose duality, this can simply be calculated by adding the eigenenergies of the single particle states up to the Fermi energy

$$E_{TG} = \sum_{i=0}^{N-1} \epsilon_i \, . \tag{3.14}$$

The energy profile for a gas of thirty particles for different δ-perturbation strengths as a function of the position of the perturbation is shown in Fig. 3.7. One can see a series of lobes (the plot is symmetric for $d < 0$), which become more pronounced as the strength of the perturbation is increased, but whose position is independent of κ. The position of these local maxima correspond to the positions in which the amplitudes for the single particle wavefunctions peak, highlighting the crystal structure of the ground

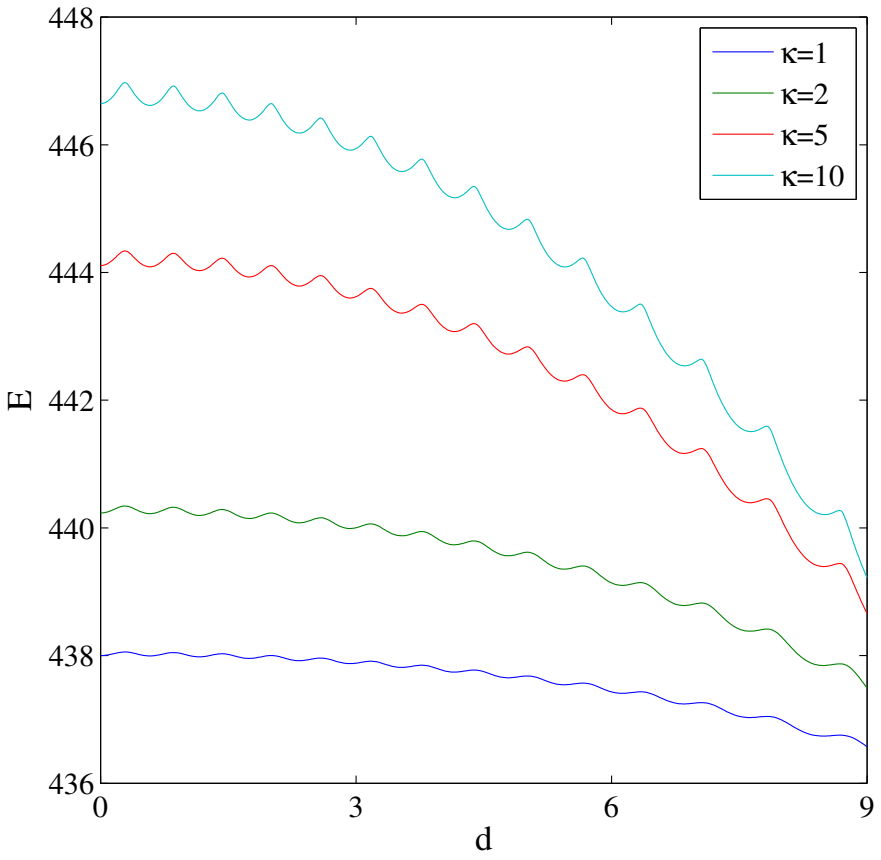


FIGURE 3.7: The energy of a harmonically trapped TG gas of N=30 particles as a function of the position of the δ-perturbation. The position of the lobes are independent of the strength of the δ-function and originate from the crystalline structure of the TG gas.

state. The increase in energy, due to the impurity, is largest when it is located at the centre of the cloud. In fact, one can view the perturbation as a probe which, when dragged adiabatically through a TG gas, makes it possible to gain information on the crystal structure of the state through an energy measurement. In the next section we will look at non-local properties of the ground state, which can be calculated from the reduced single particle density matrix.

3.3.3 Reduced single particle density matrix

The calculation of the reduced single particle density matrix (RSPDM),

$$\rho^1(x,x',t) = N\int_{-\infty}^{\infty} \Psi_B^*(x,x_2,\ldots,x_N,t)\Psi_B(x',x_2,\ldots,x_N,t)dx_2\ldots dx_N \ , \qquad (3.15)$$

and related observables for an ultracold gas is, in general, a difficult feat. The dimension of the integral in Eq. (3.15) increases with particle number and this is very demanding

on computer memory resources. For a TG gas in a harmonic potential, studies have therefore mainly used numerical methods such as Monte-Carlo integration to calculate the RSPDM [48], but some analytic work has also been done in this direction [49]. An exceptionally efficient algorithm for calculating the RSPDM of a TG gas in an arbitrary external potential has been presented by Pezer and Buljan [113]. This algorithm allows for a numerically exact calculation of the RSPDM for a large number of particles with limited memory resources and at a rapid computational speed. The algorithm works for both time dependent and time independent potentials. The essential idea is that $\rho^1(x, x', t)$ can be expressed in terms of the dynamically evolving single particle energy eigenbasis, $\psi_i(x, t)$, as

$$\rho^1(x, x', t) = \sum_{i,j}^{N} \psi_i^*(x, t) A_{ij}(x, x', t) \psi_j(x', t) \ , \tag{3.16}$$

where the $N \times N$ matrix, $\mathbf{A}(x, x', t)$, is given by

$$\mathbf{A}(x, x', t) = (\mathbf{P}^{-1})^T \det \mathbf{P} \ , \tag{3.17}$$

and the entries of the matrix $\mathbf{P}$ are computed as

$$P_{ij}(x, x', t) = \delta_{ij} - 2 \int_x^{x'} d\xi \psi_i^*(\xi, t) \psi_j(\xi, t) \ , \tag{3.18}$$

where δ_{ij} is the Kronecker delta. Given a pair of points (x, x') and the single particle basis functions $\psi_i(x, t)$ one can calculate the RSPDM of a TG gas by merely calculating the $N \times N$ matrix P, its inverse and its determinant, which is a significant saving on computational resources.

We show the effect of the δ-function potential on the many-body correlations in the RSPDM in Fig. 3.8 for the two cases of $d = 0.5$ and $d = 1$ for a gas of $N = 10$ particles. At $d = 0.5$ the δ-function is positioned at the closest intensity maximum from the origin of the unperturbed single particle density. The RSPDM shows prominent off-diagonal terms as the δ-function effectively splits a hard-core boson and creates a superposition state. At $d = 1$ the δ-function is positioned at the closest intensity minimum from the origin of the unperturbed single particle density. In this case the off-diagonal terms are reduced as the δ-function is located between two hard-core bosons and splits the gas into two separated subsystems.

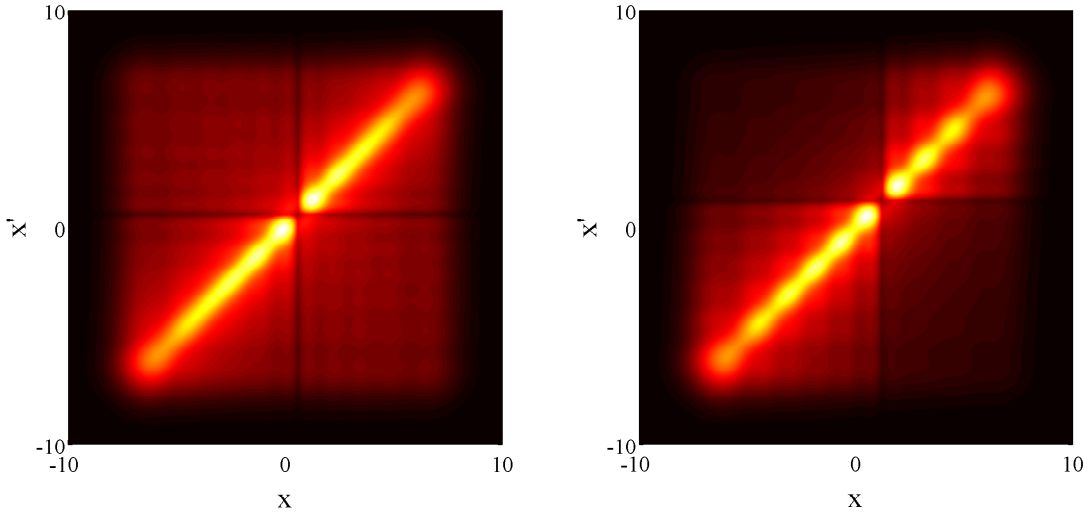


FIGURE 3.8: The RSPDM is calculated for a gas of $N = 10$ particles for two different positions of the δ-function of strength $\kappa = 10$. In the left-hand side panel the δ-function is positioned at $d = 0.5$, at the first intensity maximum of the unperturbed density. In the right-hand side panel the δ-function is positioned at $d = 1$, at the first intensity minimum of the unperturbed density. The contrast in the off-diagonal implies that the state at $d = 0.5$ has a greater coherence than the state at $d = 1$.

3.3.4 Natural orbitals

The RSPDM can be written in terms of its natural orbitals $\phi_i(x)$ as shown in Eq. (1.26) where λ_i are the associated occupation numbers. The expansion in Eq. (1.26) is extremely useful for understanding the ground state properties of cold atomic gases, as the natural orbitals are defined not only for an ideal gas but also for interacting, thermal and non-uniform gases. The fraction of particles that are in the lowest lying orbital $\phi_0(x)$ is the largest eigenvalue λ_0 of the RSPDM. Therefore, in analogy to the macroscopic occupation of a single eigenstate in a Bose-Einstein condensate, this orbital is sometimes referred to as the *BEC* state and the quantity λ_0 can act as a measure of the coherence in the system, which we will discuss in the next section.

In Fig. 3.9 the three natural orbitals with the lowest energy for a gas of 20 particles are shown. In the we top row the δ-function coincides with a position of a maxima in coherence at $d = 0.22$. In the bottom row the δ-function is at a position of a minima of coherence at $d = 0.42$. Even though the difference in the position of the δ-funcion is quite small compared to the size of the gas this has a profound effect on the lowest energy orbital. As this orbital is occupied by a large fraction of the gas it plays a significant role in the coherence of the system.

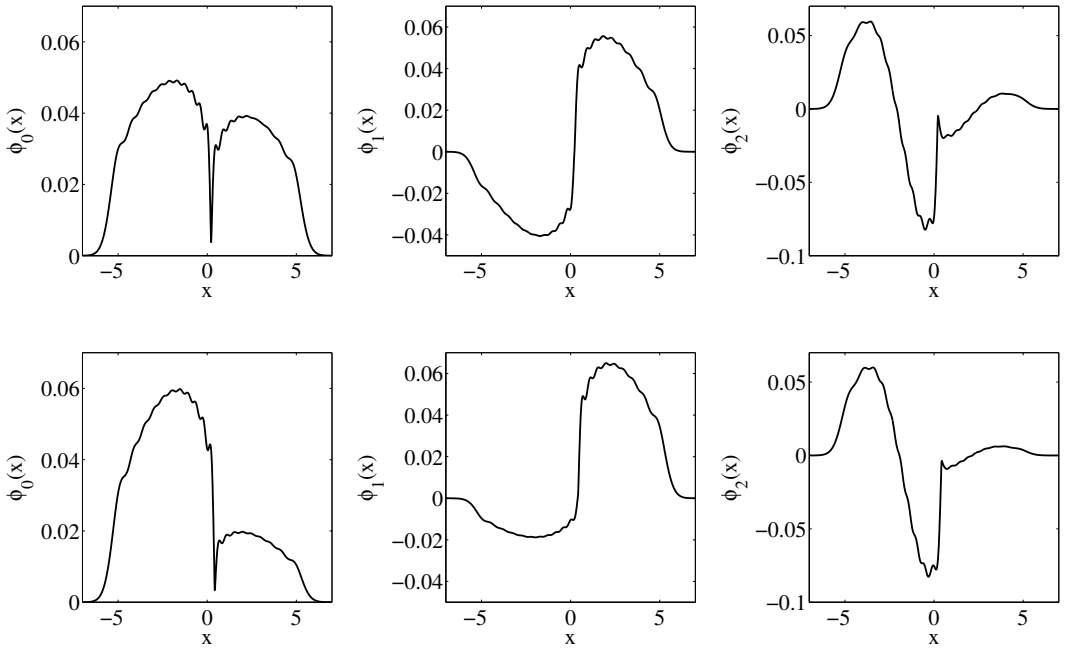


FIGURE 3.9: The three lowest energy orbitals are shown for a gas of $N = 20$ particles for two different positions of the δ-function of strength $\kappa = 10$. In the top row the δ-function is positioned at a maximum of coherence ($d = 0.22$) and in the bottom row the δ-function is positioned at a position of minimum coherence ($d = 0.42$).

3.3.5 Momentum distribution

Another important measure of coherence can be inferred from the momentum distribution of the gas, which is derived from the RSPDM in Eq. (1.27). For a homogenous, non-interacting Bose gas at zero temperature the momentum distribution is a δ-function, reflecting the macroscopic occupation of the lowest natural orbital, whereas in the strongly interacting TG gas in equillibrium, the momentum distribution is comprised of a non-trivial distribution of quasi-momenta. The amplitude of the peak of the momentum distribution at $k = 0$ can therefore also be used to measure the spatial coherence present in the system. It is well known that this quantity does not follow a trivial behaviour in a disturbed, strongly interacting gas and that in particular, it can show a dependence on the parity of the number of particles [102, 114–117].

In Fig. 3.10 the momentum distribution for a gas of 10 particles is shown with the δ-function barrier located at $d = 0.5$ (solid line) and $d = 1$ (dashed line) which are the positions of an intensity maximum and minimum of the unperturbed single particle density respectively. In each case the barrier splits the gas into two almost separate wells. At $d = 0.5$ the barrier is positioned at a maximum of the unperturbed single particle density which is the probable position of a hard-core boson. This particle is split into a

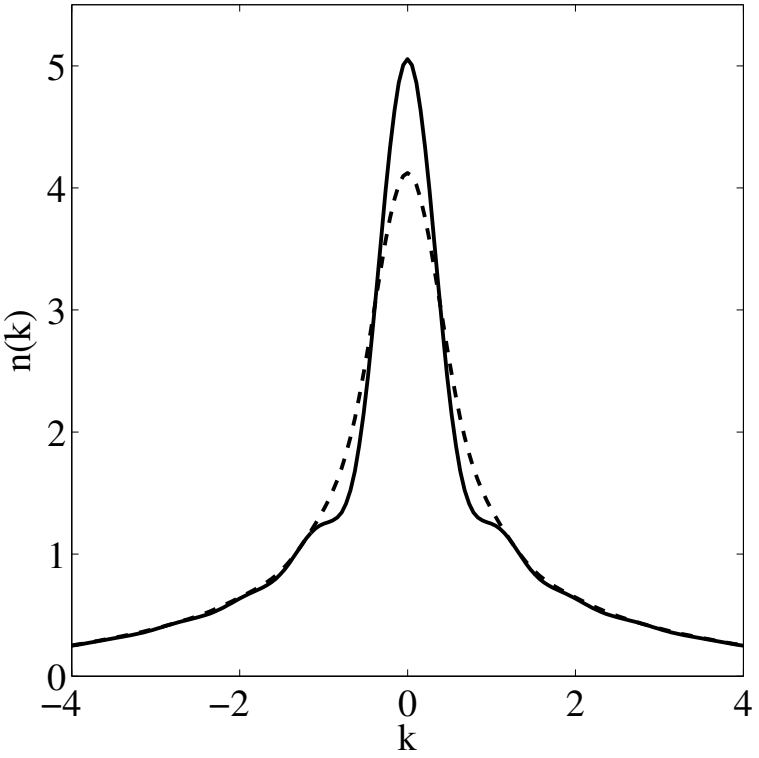


FIGURE 3.10: The momentum distribution of a gas of 10 particles punctuated with a δ-barrier of height $\kappa = 10$ is shown. At the point of high coherence (solid line, $d = 0.5$) the momentum distribution has secondary peaks caused by an interference effect. At the point of low coherence (dashed line, $d = 1$) the momentum distribution is broadened as the barrier separates the gas into two localised wells.

superposition state to the left and right-hand side of the barrier thus connecting the two localised gases. This results in interference between these separate gases which causes the appearance of the secondary peaks in the momentum distribution. At $d = 1$ the barrier is positioned between two particles and localises the gas almost completely into the two separate wells consequently broadening the momentum distribution. It should also be noted that there is a large difference in the heights of the respective momentum peaks indicating a difference in the coherence of these two situations.

In Fig. 3.11 we show the occupation of the lowest orbital, λ_0, in the left-hand panel and the peak of the momentum distribution, $n(k = 0)$, in the right-hand side panel. Both quantities are plotted as a function of distance of the perturbation from the trap centre for gas of $N = 10$ particles. As expected, they exhibit similar features that are dominated by an oscillatory structure which becomes more pronounced as the strength of the δ-perturbation increases. As in the interpretation of the energy oscillations, the maxima correspond to positions where the single particle eigenstates have large probabilities, i.e. where the position of the δ-potential corresponds to a lattice point of the underlying crystal structure of the TG gas. For comparison in Fig. 3.12 we show the same quantities

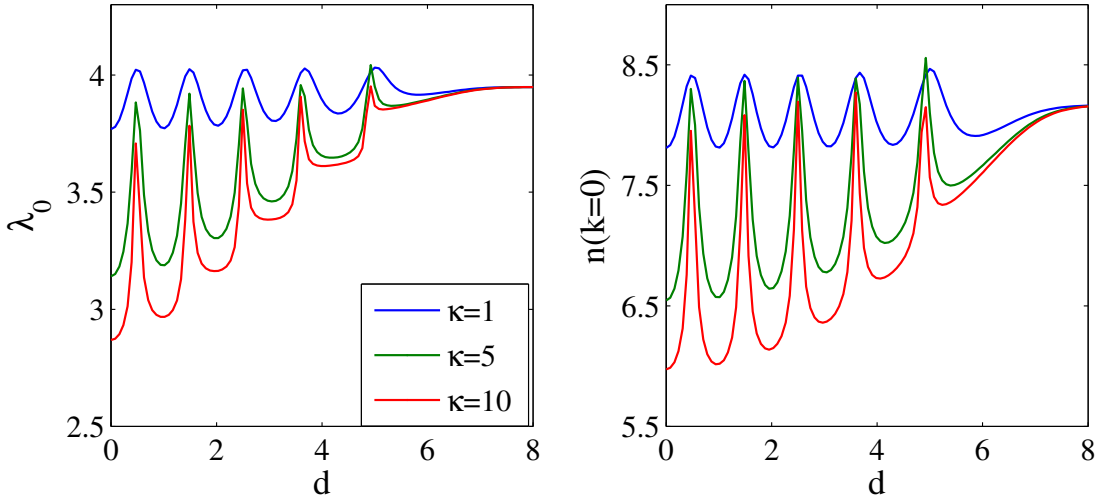


FIGURE 3.11: The largest eigenvalue of the RSPDM λ_0 and the peak of the momentum distribution $n(k = 0)$ as a function of eccentricity d for perturbation strengths $\kappa = 1, 5, 10$ for a TG gas of $N = 10$ particles.

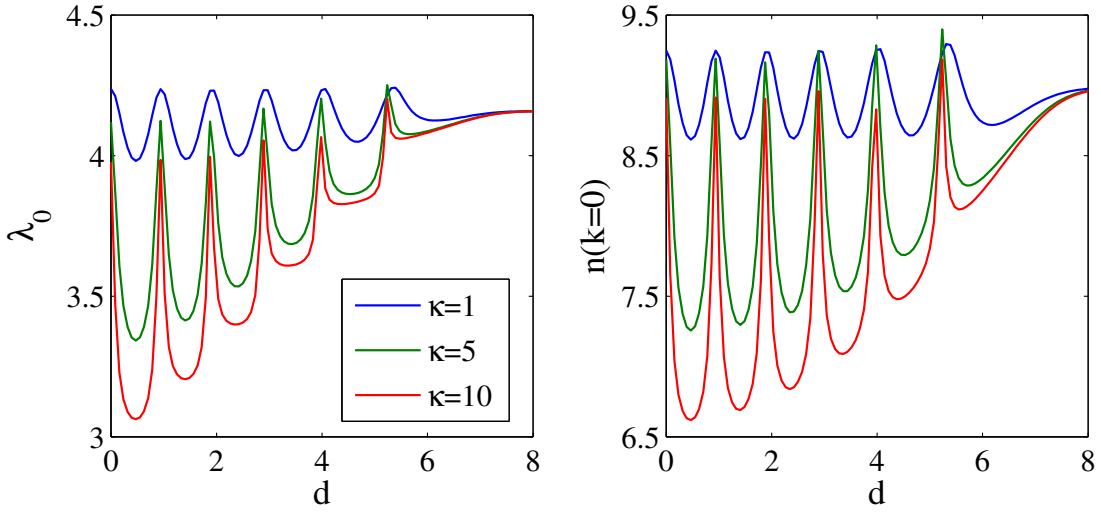


FIGURE 3.12: The largest eigenvalue of the RSPDM λ_0 and the peak of the momentum distribution $n(k = 0)$ as a function of eccentricity d for perturbation strengths $\kappa = 1, 5, 10$ for a TG gas of $N = 11$ particles.

for the $N = 11$ case. In this case we see a maximum of coherence at $d = 0$, as symmetry reasons require a single particle to sit in the centre of the trap for odd particle numbers [102].

3.4 Free expansion

This dependence of the coherence on the position of the disturbance can be experimentally observed by measuring the visibility in an interference experiment. To simulate this, we calculate the time evolution of the single particle density $\rho(x,t)$ as the gas is allowed to expand in free space. This was calculated numerically using the split operator method [111] but one may also employ a scaling transformation [114]. Initially at $t = 0$ the gas is confined in the harmonic trap where the δ-function is positioned at $d = 0.5$ and $d = 1$ for a gas of $N = 10$ atoms and $\kappa = 10$ (same situation as in Fig. 3.8). For $t > 0$ the trapping potential and the δ-function are removed and the two parts of the gas are allowed to overlap and interfere. In Fig. 3.13 the single particle density is plotted and the difference in the visibility of the interference fringes is clearly observable for a gas with large coherence (left-hand side panel) and a gas with low coherence (right-hand side panel).

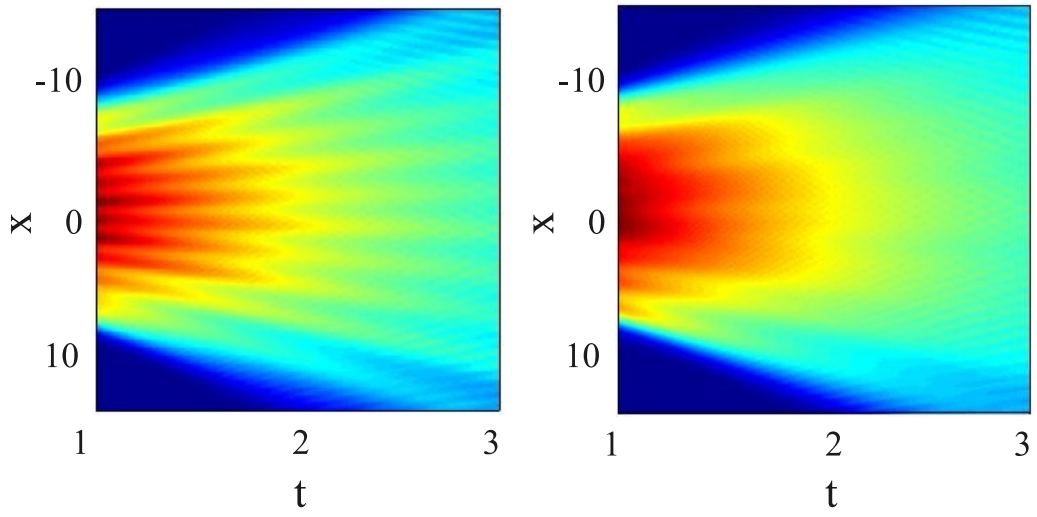


FIGURE 3.13: Single particle density of the free evolution of the gas after realease from the trapping potential. Left-hand side: the δ-barrier is positioned at $d = 0.5$ corresponding to a maximum coherence. Right-hand side: the δ-barrier is positioned at $d = 1$ corresponding to a minimum coherence. Interference fringes indicate greater spatial coherence which confirms the results from Fig. 3.11.

3.5 Conclusions

We have discussed a model describing a harmonically trapped TG gas in the presence of a δ-perturbation of arbitary strength and eccentricity. We have taken advantage of the exact solution of the fundamental single particle problem and shown how it can be used in combination with known techniques to describe the ground state properties of

the gas. It should be emphasised that this is a suitable model to test concepts in exactly solvable systems due to the current experimental feasibility of embedding impurities in ultracold gases [118, 119].

We have calculated the energy profile of the gas in the presence of the impurity and found an undulating profile as the perturbation is displaced through the gas, which highlights the crystal structure of the TG ground state. In addition, we have calculated the momentum distribution and largest eigenvalue of the RSPDM as a function of both the eccentricity and strength of the perturbation which is an indication of the coherence of the gas. Again, we have found that these properties reflect the highly localised nature of the particles in the TG gas.

Furthermore as a novel application of our model we have investigated the time density dynamics after a sudden removal of the perturbation. We find that the gas exhibits the classical Talbot effect with the image of the impurity reappearing at multiples of the inverse trap frequency. Finally we simulated the ballistic expansion of the gas and showed the presence of interference fringes which exist when the gas is split at the position of a particle in the gas. This is a readily achieveable experiment which can be used to explore the coherence properties of the TG gas.

3.6 Outlook

As discussed previously, experiments have been carried out embedding ions in ultracold gases [120] and recently theoretical work has described the effect of the ions micromotion on a neutral atom [121]. It would be an interesting extension of this work to investigate the effect of this micromotion on the TG gas.

Chapter 4

The orthogonality catastrophe in a Fermi gas

4.1 Introduction

In the past decade ultracold quantum gases have emerged as ideal candidates for designing controllable experiments to simulate effects in condensed matter physics [6]. The advantage of using ultracold gases lies in their ability to create clean systems such as atomic lattices without impurities and defects. Also in the ground state of the gas there are no phonons so the system is free of thermal fluctuations. When one has the ability to create such ideal systems the pertinent course of action is to study how impurities play a role in the dynamics of the system by means of a quantum quench. If we take a state $|\Psi\rangle$ which is an eigenstate of the Hamiltonian $\hat{H}$ a quench is the result of the sudden application of a different Hamiltonian, $\hat{H}' = \hat{H} + \lambda V$, which forces the system under study out of equilibrium. These quenches can be global, such as a change of trapping frequency or interaction strength, or they can be local, like the effect of an impurity which interacts with a subset of the system thus allowing detailed investigations into the theory of quantum interactions and decoherence.

We will concentrate on studying a local quench in this Chapter and will explore a hybrid system in which two separate, ultra-cold atomic systems are combined in such a way that their coupling can be externally controlled and their states independently

I would like to acknowledge the contribution of Dr. Lo Gullo, who derived the many-particle overlap for thermal states in Section 4.7.

measured. Existing examples of such systems are single spin impurities embedded in ultracold Fermi gases [122, 123] and the combination of neutral [124, 125] or charged single atoms [119, 126] with Bose-Einstein condensates. The impurity we consider consists of a two-level system which interacts via a δ-function potential with an environment of one-dimensional, non-interacting, spinless fermions. This choice of environment is particularly interesting as it allows us to study a quantum many-body effect which has been observed in solid state systems, the Anderson orthogonality catastrophe (OC).

4.1.1 Orthogonality Catastrophe

4.1.1.1 Time independent case

Let us discuss the original idea of Anderson [127] by considering the ground state of a non-interacting, spin-polarized Fermi gas in a hard-wall, spherically-symmetric box of radius R at zero temperature. The many-particle wave-function of the gas is given by the Slater determinant of the radial single-particle eigenstates $\psi_n(k_j, x_j)$ as

$$\Psi(r_1, r_2, \ldots, r_N) = \frac{1}{\sqrt{N!}} \det_{(n,j)=(0,1)}^{(N-1,N)} \psi_n(k_j, r_j) \ , \tag{4.1}$$

where r_j (k_j) is the coordinate (wavenumber) of the j^{th} particle. For spherical symmetry ($l = 0$) the eigenstates are given by the Bessel functions

$$\psi_n(k_j, r_j) = \frac{\sin(k_j r_j)}{k_j r_j} \ , \tag{4.2}$$

where $k_j = \pi n/R$ and the energy of the single particle states are $E_j = \hbar^2 k_j^2/2m$. For simplicity only the $l = 0$ scattering states are presumed here, however this does not alter the result as the inclusion of higher angular momenta will act to increase the orthogonality [127]. Consider now the same system, but in the presence of a static perturbation. Intuitively, the single-particle states are deformed and if the perturbation is highly localised, the new states can be written asymptotically as $\psi_n'(k_j, r_j) \sim \frac{\sin(k_j r_j + \delta(1 - \frac{r_j}{R}))}{k_j r_j}$, where δ is an s-wave phase shift which leads to a modified state of the Fermi sea $|\Psi'\rangle$.

The idea behind the OC is to see under which conditions the respective many-body states become orthogonal, ie. $\langle\Psi|\Psi'\rangle \to 0$. For this the overlap between two many-body wavefunctions needs to be calculated which is no easy task for states with a large number of particles. Fortunately the many-body overlap may be calculated by only considering the single particle states of the systems being studied which we will now outline. Consider the single particle Hamiltonians $\hat{h}$ and $\hat{h}'$ and their respective single

particle eigen-equations

$$\begin{aligned} \hat{h}|\psi_m(x)\rangle &= \epsilon_m|\psi_m(x)\rangle \ , \\ \hat{h}^{'}|\psi_n^{'}(x)\rangle &= \epsilon_n^{'}|\psi_n^{'}(x)\rangle \ . \end{aligned} \tag{4.3}$$

For fermions the many-body wavefunctions are easily obtained as Slater determinants

$$\begin{aligned} \Psi_i(x_1,...,x_N) &= \frac{1}{N}\sum_P \mathrm{sgn}(P)\ \psi_{P(1)}(x_1)\cdots\psi_{P(N)}(x_N) \ , \\ \Psi_j^{'}(x_1,...,x_N) &= \frac{1}{N}\sum_{P'} \mathrm{sgn}(P')\ \psi_{P'(1)}^{'}(x_1)\cdots\psi_{P'(N)}^{'}(x_N) \ , \end{aligned} \tag{4.4}$$

where $P(P')$ is the permutation over the indices labeling the occupied states. The overlap between any two many-body wavefunctions can then be calculated as

$$\begin{aligned} \Lambda_{i,j} &= \langle\Psi_j^{'}(x_1,...,x_N)|\Psi_i(x_1,...,x_N)\rangle \\ &= \int (\Psi_j^{'}(x_1,...,x_N))^*\Psi_i(x_1,,...,x_N)dx_1\cdots dx_N \\ &= \sum_{P,P'}\mathrm{sign}(P)\mathrm{sign}(P')\prod_l \Delta_{P(l),P'(l)} \ , \end{aligned} \tag{4.5}$$

where $\Delta_{m,n} = \int\ dx(\psi_n^{'}(x))^*\psi_m(x)$ is the overlap between two single particle states. We assume that only N_1 and N_2 single particle states can be occupied by the two sets $\{|\psi_m(x)\rangle\}$ and $\{|\psi_n^{'}(x)\rangle\}$ respectively where $N_1 \geq N$ and $N_2 \geq N$. The elements of the matrix Λ are the minors of order N of the $N_2 \times N_1$ matrix $\Delta_{m,n}$ made of all the possible occupied single particle state's overlaps.

For the ground state this result is identical to that in Anderson's original paper [127],

$$\nu = \Lambda_{0,0} = \langle\Psi^{'}|\Psi\rangle = \det[\Delta_{m,n}] \ , \tag{4.6}$$

This result shows that to calculate the many-body overlap one must only take the determinant of the matrix of single particle states $\Delta_{m,n}$. When evaluating the overlap for Anderson's original situation with fermions in a spherically symmetric box, one finds $\nu \propto N^{-\frac{\alpha}{2}}$ with $\alpha = \frac{2\delta^2}{\pi^2}$. Therefore the overlap goes rapidly towards zero for N and/or δ sufficiently large [127].

It is interesting to note that this calculation of the many body overlap for fermionic states can be straightforwardly applied to a Tonks-Girardeau gas which has been discussed in Chapter 3. To calculate the many-body overlap for this situation the appropriate unit anti-symmetric function has to be applied to the fermionic wavefunction $\Psi_B = A\Psi_F$,

$A = \prod_{1\leq i<j\leq N} sgn(x_i - x_j)$ which gives

$$\begin{aligned}\nu &= \int (\Psi_B(x_1, ..., x_N))^* \Psi_B^{'}(x_1, ..., x_N) dx_1 \cdots dx_N \\ &= \int (A\Psi_F(x_1, ..., x_N))^* A\Psi_F^{'}(x_1, ..., x_N) dx_1 \cdots dx_N \\ &= \int A^2 (\Psi_F(x_1, ..., x_N))^* \Psi_F^{'}(x_1, ..., x_N) dx_1 \cdots dx_N \\ &= \int (\Psi_F(x_1, ..., x_N))^* \Psi_F^{'}(x_1, ..., x_N) dx_1 \cdots dx_N.\end{aligned} \tag{4.7}$$

As A can only have values ± 1 its square is always positive and the overlap for two systems of strongly interacting bosons is equivalent to that of the corresponding system of non-interacting fermions in Eq. (4.5).

4.1.1.2 Time dependent case

While Anderson's original work involved stationary states, the creation of a perturbed many-body state is, in general, a time-dependent process. The dynamical theory of the OC was developed by Nozières and De Dominicis [128] who described the effects appearing in X-ray absorption spectroscopy in metals. An incident X-ray is absorbed by the metal and the photon energy is used to promote an electron from the core level to an unoccupied state in the conduction band. At zero temperature the only unoccupied states lie above the Fermi-energy and for this absorption process to be possible the energy of the incident X-ray must be at least $\hbar\omega_T = E_b + E_C$ where ω_T is the threshold frequency for the creation of the hole, E_b is the width of the occupied conduction band and E_C is the binding energy of the core-level. The ejected electron leaves behind a hole in the core level which is seen as an impurity by the electron gas. The core-hole can decay in several possible ways, but two processes dominate. The first decay is an Auger process which involves an electron from a higher state falling into the core-hole while its energy is transferred to another electron whose energy is then increased. By using Auger spectroscopy the electron which gains this energy can be measured [129]. The second process results in the emission of an X-ray photon by the electron which falls into the core-hole and this provides a measurement over the occupied states in the ground state of the Fermi sea.

The question is what impact does the sudden appearance of the core-hole have on the $N \approx 10^{23}$ conduction electrons in the metal and how does this affect the single particle spectrum of the Fermi sea? Nozières and De Dominicis calculated the transient response of a Fermi sea after the *sudden* switching on of a core-hole in a metal where a direct manifestation of the OC can then be observed in the single-particle spectrum of the

Fermi gas

$$A(\omega)=2\Re\int_{-\infty}^{\infty}dt\; e^{i(\omega-\omega_T)t}\nu(t)\;, \tag{4.8}$$

here $\nu(t)=\langle\Psi|e^{i\hat{H}t}e^{-i\hat{H}'t}|\Psi\rangle$ is the propagator of the core hole's retarded Green's function at zero temperature

$$G(t) \;=\; -ie^{-it\omega_T}\Theta(t)\langle\Psi|e^{i\hat{H}t}e^{-i\hat{H}'t}|\Psi\rangle. \tag{4.9}$$

Here $\Theta(t)$ is the Heaviside step function, $|\Psi\rangle$ is the initial equilibrium state of the Fermi system, governed by the Hamiltonian $\hat{H}$, and the subsequent evolution of the Fermi sea in the presence of the impurity is given by $\hat{H}'$ [130]. In the absence of the core-hole, the single-particle spectrum of the homogeneous non-interacting Fermi gas is a Dirac δ-function peaked at the Fermi energy. However due to the interactions inside the electron gas within the OC regime the spectral function broadens and turns into a power law distribution which eliminates any δ- function character. In real systems where the number of electrons is $N\sim 10^{23}$, typically α is found to be in the region $0.1\rightarrow 0.2$. Relating this to Anderson's many-body overlap, $\nu=N^{-\alpha/2}$, the values lie in the range of $0.1\rightarrow 0.01$.

The evaluation of the Green's function in Eq. (4.9) now amounts to calculating the overlap $\nu(t)$ between the perturbed and unperturbed time-dependent many-body wave-functions. However, given that

$$\begin{aligned}\nu(t) &= \langle\Psi|e^{i\hat{H}t}e^{-i\hat{H}'t}|\Psi\rangle \\ &= \sum_j |\Lambda_{0,j}|^2 e^{-i(E_j'-E_0)} \\ &= \det[A_{n,m}(t)]\;,\end{aligned} \tag{4.10}$$

with $A_{n,m}(t)=\int(\psi_n'(x,t))^*\psi_m(x,t)dx$, this reduces to calculating the overlap of the time-dependent single-particle states and Eq. (4.10) can be therefore evaluated by simple knowledge of the relevant quenched single-particle states, $\psi_n'(x,t)$.

4.2 Loschmidt Echo

A powerful tool to study the sensitivity of quantum evolutions due to perturbations is the Loschmidt echo [131]. It is a measure of the reversibility of a quantum state when an imperfect time-reversal procedure is applied to it and can be written as

$$L(t)=|\langle\Psi|e^{i\hat{H}_1t}e^{-i\hat{H}_2t}|\Psi\rangle|^2\;, \tag{4.11}$$

where $|\Psi\rangle$ is the initial state evolved under two different Hamiltonians $\hat{H}_1$ and $\hat{H}_2$. In the case where $|\Psi\rangle$ is an eigenstate of $\hat{H}_1$ and $\hat{H}_2 = \hat{H}_1 + \lambda V$ is the same Hamiltonian with a perturbation of strength λ the Loschmidt echo is a measure of the sensitivity of the evolution of the initial state to a perturbation. In this case the Loschmidt echo can also be referred to as the fidelity of the state and is the squared norm of Eq. (4.10)

$$L(t) = |\nu(t)|^2. \tag{4.12}$$

The Loschmidt echo has a broad scale of interest in different scientific communities and is used in studying quantum phase transitions, quantum criticality, quantum chaos, spin echo in NMR and decoherence in open quantum systems [132, 133]. For this last area the application of the Loschmidt echo is particularly exciting as it is clear that decoherence limits the implementation of quantum computers as one scales up the number of qubits and increases the complexity of the system. The Loschmidt echo is thus a powerful tool to examine the noisy effects of the environmental degrees of freedom and allows one to quantify decoherence.

The Loschmidt echo usually is a decaying function of time and the rate of decay depends on the classical dynamics of the system, the choice of initial state and more importantly the form and strength of the perturbation applied to the system [134–136]. If we study the Loschmidt echo averaged over an ensemble of initial states it will initially embark on parabolic decay $\overline{L(t)} \simeq 1 - (\eta t/\hbar)^2$ where η is an average dispersion based on the type of perturbation used. However, the parabolic decay only holds for short times when the propagators of the individual Hamiltonians can be approximated by their second order Taylor expansions, ie. $\exp(-iHt/\hbar) = 1 - iHt/\hbar - (Ht)^2/(2\hbar^2)$.

After the initial parabolic decay the asymptotic decay is dependent on the strength of the perturbation κ and can generally be classified into two regimes: Gaussian and exponential. In the Gaussian regime the Loschmidt echo decays as $\overline{L(t)} \simeq \exp(-(\eta t/\hbar)^2)$; this applies to the situation where the perturbation is weak compared to the mean energy level spacing of the unperturbed Hamiltonian. In the exponential regime the Loschmidt echo decays as $\overline{L(t)} \simeq \exp(-\Gamma t)$ which holds when the perturbations are large on the scale of the mean energy level spacing. Here Γ is a function κ and at long times the Loschmidt echo saturates as $\overline{L(t)} \sim N^{-1}$ where N is the size of the Hilbert space.

4.3 Impurity in an Harmonic Trap

Since all that is needed to construct the overlaps between the many-body wavefunctions are the eigensolutions of the corresponding single particle problems the δ-split harmonic

trap offers an exactly solvable model in which to investigate the effects of the OC on a large Fermi gas. The model and its solutions have been discussed in Chapter 3 and here we consider the initial state $|\Psi\rangle$ to be given by Fermi gas of N particles at zero temperature trapped in a simple harmonic oscillator potential. The perturbed state $|\Psi'\rangle$ is the harmonically trapped gas punctuated by a δ-function potential of height κ situated at a distance d from the trap centre. The respective Hamiltonians $\hat{H}$ and $\hat{H}'$ are scaled as described previously (Sec. 3.2.1) and are presented here in that form

$$\hat{H} = \sum_{n=1}^{N} \left[-\frac{\partial^2}{\partial x_n^2} + \frac{1}{2} x_n^2 \right] , \tag{4.13}$$

$$\hat{H}' = \sum_{n=1}^{N} \left[-\frac{\partial^2}{\partial x_n^2} + \frac{1}{2} x_n^2 + \kappa \delta(x_n - d) \right] . \tag{4.14}$$

The magnitude of κ is related to the scattering phase shift δ explained in Anderson's work [127].

In the left panel of Fig. 4.1 the overlap for an infinite δ-function positioned at the origin is plotted versus total particle number N. If the δ-function has infinite height this means that every even eigenstate is degenerate with the next highest odd eigenstate and can be easily written as

$$\psi_n(x) = \begin{cases} C_n e^{-\frac{x^2}{4}} H_n(x), & n \text{ odd} , \\ C_{n+1} e^{-\frac{x^2}{4}} H_{n+1}(|x|), & n \text{ even} , \end{cases} \tag{4.15}$$

with the normalisation $C_n = (\sqrt{\pi/2} a_\perp 2^n n!)^{-\frac{1}{2}}$ where $a_\perp = \sqrt{\frac{\hbar}{m\omega}}$ [137]. As N increases the overlap between $|\Psi\rangle$ and $|\Psi'\rangle$ decreases as prescribed by the OC. The δ- function only affects the even eigenstates which means that $\nu(2N) = \nu(2N+1)$ which results in a step pattern visible in the right-hand side panel of Fig. 4.1. Interestingly, and in contrast to Anderson's finding that the states become orthogonal for increasing N we find that the many-body overlap begins to increase again after an initial decrease at a certain N, which is dependent on the strength of the impurity κ. From the right-hand side panel of Fig. 4.1 this increase can be seen to appear for $N > \kappa$. Even though this contradicts Anderson's original treatise it is not in conflict with his original result as the effect the scattering potential has on the Fermi gas is different in each case. In Anderson's system only states near the Fermi surface are taken into account, meaning that the highest states are affected by an approximately equal scattering phase shift δ. In our case the impurity acts at the bottom of the Fermi sea and affects each state though an energy dependent phase shift $\delta(E)$. So for higher lying states the effect of the impurity is diminished and eventually, as the size of the system is increased, the presence of the impurity is negligible and $\nu \to 1$. This does not mean that we cannot

adequately study the orthogonality catastophe in our system, however we are limited to look at the situation of κ quite large compared to the Fermi energy. This ensures that in the system we are studying the overlap does not begin to increase again for N large but not infinite.

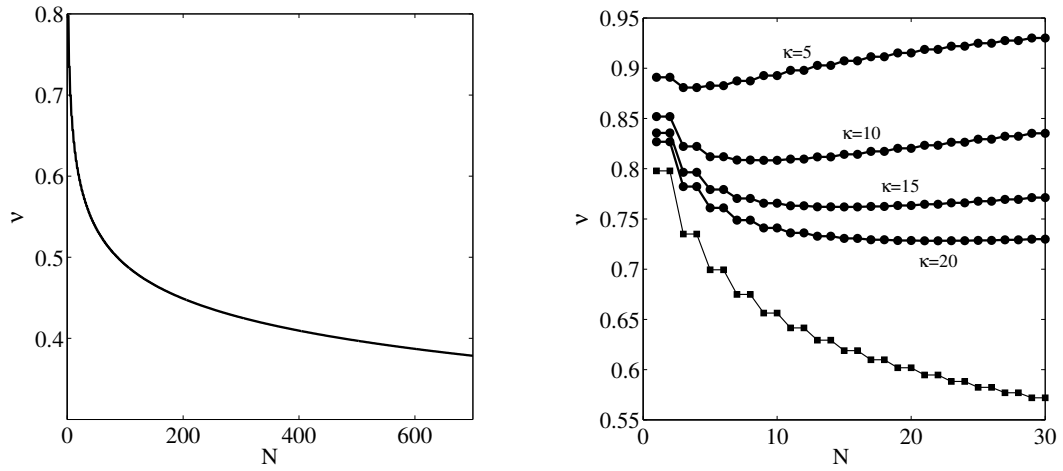


FIGURE 4.1: Overlap, ν, as a function of total particle number N. Left panel: δ-function on the origin of the harmonic trap with $\kappa \to \infty$. Right panel: δ-function of variable height $\kappa = 5, 10, 15$ and 20. For comparison $\kappa \to \infty$ is also shown (squares).

The left-hand side panel of Fig. 4.2 shows the time-independent overlap, ν, as a function of the position of the δ-function, d, for a constant height $\kappa = 1$. It is apparent that

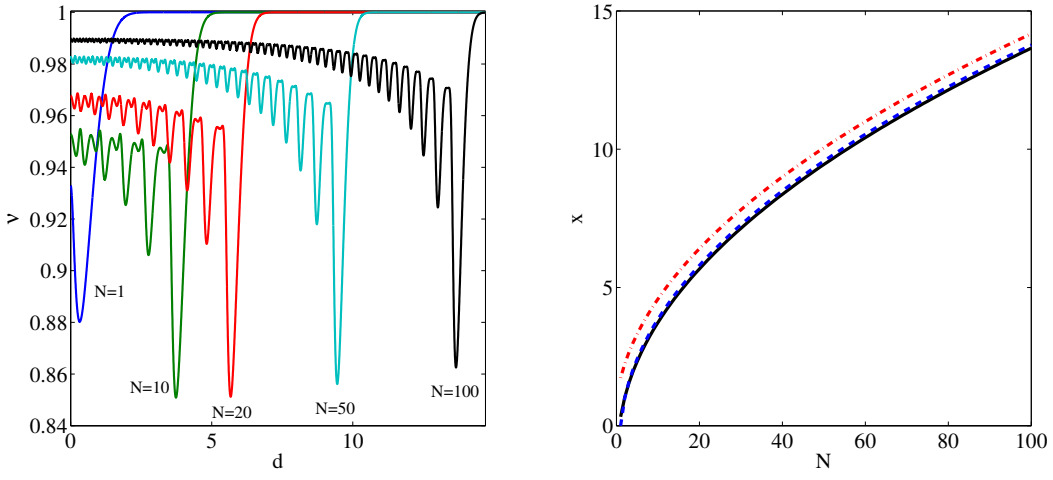


FIGURE 4.2: Left panel: The time-independent overlap, ν, is plotted versus the position d of the δ-function of height $\kappa = 1$ for $N = 1$ (blue line), 10 (green line), 20 (red line), 50 (cyan line) and 100 (black line). Right panel: The position of the δ-function when ν is a minimum is plotted versus N (solid black line). For comparison the position of the largest critical point of the highest single particle state of the Fermi sea $|\psi_N\rangle$ is shown (blue dashed line) and its width $\Delta x = \sqrt{(2n+1)}$ (red dot-dashed line).

as the total number of particles in the trap N is increased the number of troughs also increases, which highlights the crystaline nature of the Fermi-gas which is equivalent to that of the Tonks-Girardeau gas that was discussed in Chapter 3. This is because the number of nodes of the single particle states increases linearly for increasing N. What is interesting is that as the δ-function is moved from the origin of the harmonic trap the effect of the impurity potential is being moved away from the bottom of the Fermi-sea exclusively towards the Fermi surface where the overlap, ν, reaches its minimum. In the right panel of Fig. 4.2 it is shown that the minimum of ν (solid black line) follows the maximum of the probability density of the highest state in the Fermi sea, $|\psi_N\rangle$. This point lies at the edge of the single particle density of the gas which means that the impurity only disturbs a small number of particles at the Fermi edge.

The OC also manifests itself in a time evolving system which can be observed in the Loschmidt echo $L(t)$. The echo corresponding to Fermi gases for different N and κ=200 is shown in Fig. 4.3. As expected from our previous considerations, it decreases rapidly once the system size is above a moderate number. As we are creating an out of equilibrium state through the application of a sudden perturbation the minimum value of the Loschmidt echo far exceeds that which is calculated for the time-independent case. However if one was to undertake this process adiabatically the form of the overlap would be identical to that in Fig. 4.1. The revivals seen in the echo are located at the time corresponding to the inverse of the particle-hole resonances $E_j^{'} - E_0$ in the Fermi gas which are apparent from Eq. (4.10). For small particle numbers the magnitude of the revival is quite large and shows an almost complete reformation of the initial state. However for large particle numbers the OC diminishes the strength of these revivals until they are eventually no longer observable.

Conversely, if one were to consider the reverse case of starting at $t = 0$ with a gas split by a δ-function, which is then suddenly removed, one would expect perfect refocusing of the state at the revival times. This is a result of the fact that the new basis in this case is the harmonic oscillator and the evolution of all the single particle states are in phase.

4.3.1 Finite sized impurity

The impurity discussed so far has been a δ-function which is a mathematical construct of zero width and is assumed here to represent a highly localised atom or laser beam. However in reality this may not be the case due to the finite size of the particle and the beam waist of the laser. To investigate the effect of a finite sized impurity one can replace the δ-like interaction in Eq. (4.18) with a Gaussian potential with a characteristic

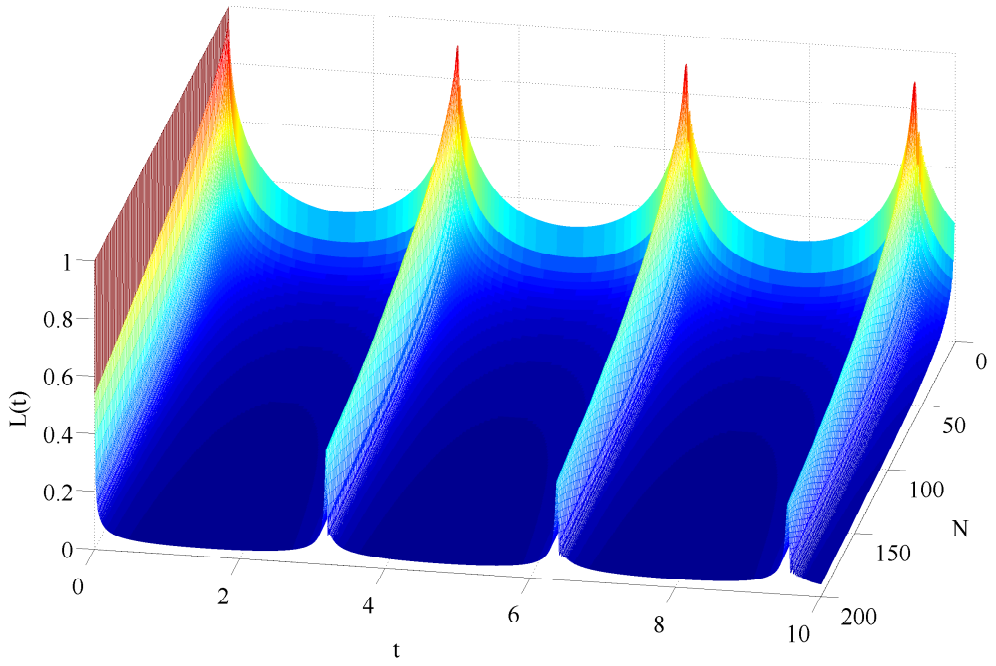


FIGURE 4.3: Loschmidt echo $L(t)$ as a function of the particle number N for $\kappa = 200$. After an initial decay revivals are seen at longer times.

width σ and height κ given by

$$V(x) = \kappa e^{-\left(\frac{x}{\sqrt{2}\sigma}\right)^2}. \tag{4.16}$$

Since the δ-like interaction only affects the even parity wavefunctions of the system, leaving the odd parity ones unchanged [138], the main effect of a finite width is a modification of all eigenstates of the system which hastens the appearance of the othogonality catastrophe. In the top row of Fig. 4.4 the overlap is calculated for a centrally placed Gaussian potential of width $\sigma = 0.01$ (left-hand side) and 0.1 (right-hand side) as a function of the total particle number N. As N is increased the overlap decays highlighting the presence of the orthogonality catastrophy. The width of the Gaussian has a strong effect on the rate of decay stemming from the odd states of the harmonic oscillator being affected to a greater extent. Similar to the case of the δ-function the overlap starts to increase again after the system reaches a certain size.

It is interesting to investigate the Loschmidt echo of this system for two points which have the same value of ν in the time independent case. The points chosen are shown in Fig. 4.4 as circles at $N = 23$ and $N = 293$ for $\sigma = 0.01$ and $N = 13$ and $N = 163$ for $\sigma = 0.1$ with $\kappa\sigma = 15$ in each case. The decay of the respective Loschmidt echoes are plotted in the second row of Fig. 4.4 and one can see that for $\sigma = 0.01$ the rate of the decay is greater for the state with the larger particle number. For $\sigma = 0.1$ the large

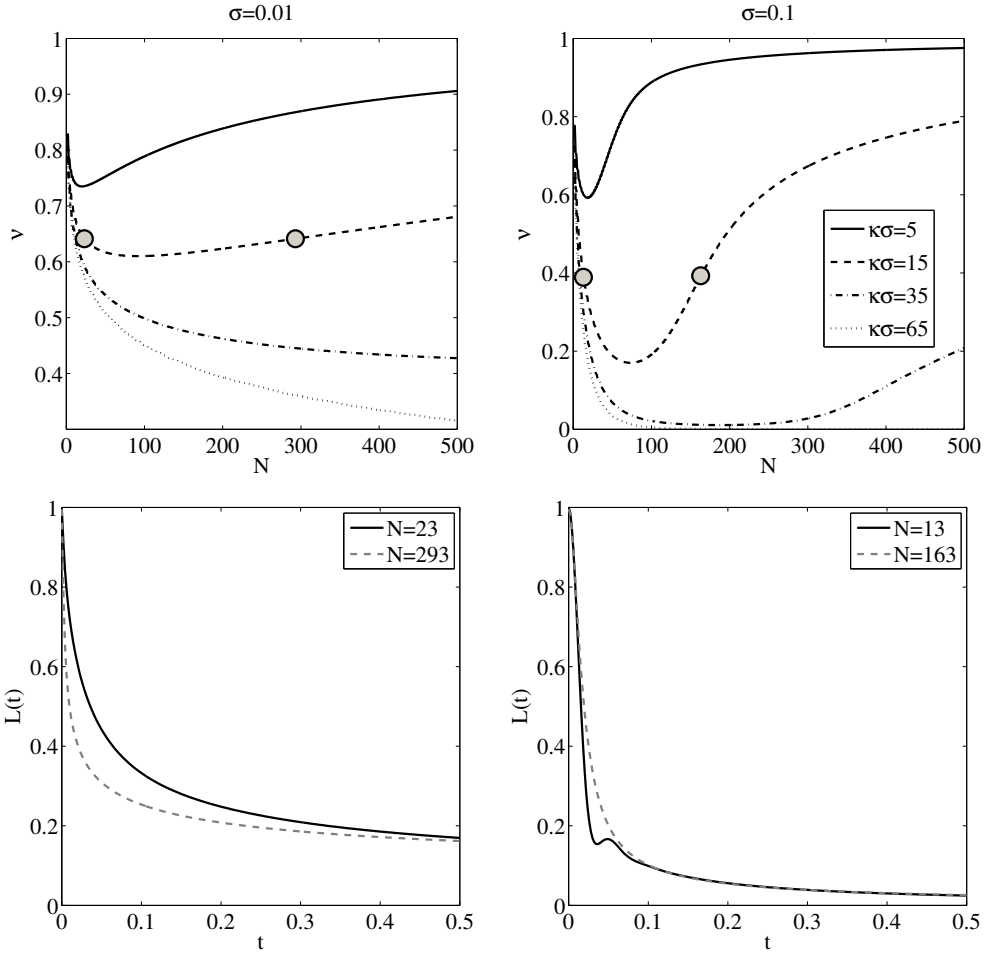


FIGURE 4.4: Time independent overlap, ν, of two many-body states of the harmonic oscillator. The perturbed state has a repulsive Gaussian barrier placed in the centre of the trap. In the top row ν is plotted versus N for defects of width $\sigma = 0.01$ and $\sigma = 0.1$ for different heights of the barrier κ. In the bottom row the Loschmidt echo is plotted for parameters which result in equal values of ν for differnt N as indicated by the grey circles in the upper row plots.

width of the Gaussian creates a lobe at short times in $L(t)$ for $N = 13$ which is washed out for larger particle numbers. In both cases the initial decay of the echo is strongly reliant on the number of particles in the state, however at long times the values of the echoes become equivalent.

4.4 System and Environment Model

In what follows we demonstrate how the physics of the OC influences the dynamics of a single auxiliary two-level system which is coupled to a non-interacting Fermi gas in a harmonic trap. As our system we choose a highly localised neutral atom [139, 140], whose relevant two levels, $|g\rangle$ and $|e\rangle$, are assumed to be separated by the energy $\hbar\Omega$, so that

the Hamiltonian reads $H_s{=}\frac{\hbar\Omega}{2}(|e\rangle\langle e| - |g\rangle\langle g|)$. The environment of the non-interacting Fermi gas is described by

$$\hat{H} = \int \hat{\Psi}^\dagger(x) \left(-\frac{\hbar^2}{2m}\frac{d^2}{dx^2} + \frac{1}{2}m\omega^2 x^2 \right) \hat{\Psi}(x) dx, \tag{4.17}$$

where $\hat{\Psi}^\dagger(x)$ is the fermionic field creation operator. At low enough temperatures, s-wave scattering is the dominating interaction process between the Fermi gas and the atom. For simplicity but without affecting the generality of our discussion, we assume that only $|e\rangle$ has a finite (positive) s-wave scattering length, while $|g\rangle$ does not interact with the environment. This does not restrict the generality of our approach as the inter-particle interactions can be tuned to any desireable value by exploiting the appropriate Feshbach resonances. Assuming that a confining potential strongly localizes the impurity's wave-function, so that its kinetic energy can be neglected, we are led to the following interaction Hamiltonian between the impurity and the Fermi gas

$$\hat{H}_I = \kappa \int \hat{\Psi}^\dagger(x) V(x) \hat{\Psi}(x) dx, \tag{4.18}$$

where $V(x) = \delta(x)$ which is the standard δ-function pseudo-potential approximation for the scattering interaction unless otherwise stated.

The analogy with the situation typically considered in the context of Anderson's OC theory should now be apparent: the localised spatial interaction of the impurity with the ultra-cold gas plays a role synonymous to the interaction of the core hole with the rest of the electrons in a metal. A key point to stress is that here, in contrast to the case of a metal, we have typically a far smaller number of particles in the environment, which could in principle compromise the observability of the OC effects. However, as noted in Sec. 4.1.1.1 the OC can be observed in the mesoscopic domain for large κ.

Let us start by assuming that, at time $t < 0$, the atom is prepared in $|g\rangle$ with the Fermi gas in its ground state $|\Psi\rangle$. The collective state of the hybrid system can be written as $|\Phi\rangle = |g\rangle \otimes |\Psi\rangle$. At $t = 0$, a properly set interaction between the atom and a classical laser field prepares the two-level state in $(|g\rangle + |e\rangle)/\sqrt{2}$ and the perturbed Fermi sea evolves according to $\hat{H} + \hat{H}_I$, driving the overall system into a correlated state of the form

$$|\Phi'\rangle = \left(|g\rangle \otimes e^{-i\hat{H}t}|\Psi\rangle + |e\rangle \otimes e^{-i(\hat{H}+\hat{H}_I)t}|\Psi\rangle \right) / \sqrt{2}. \tag{4.19}$$

The state of the environment now comprises the atomic states $|\Psi'_g(t)\rangle = e^{-i\hat{H}t}|\Psi\rangle$, associated with the non-interacting microscopic state $|g\rangle$, and $|\Psi'_e(t)\rangle = e^{-i(\hat{H}+\hat{H}_I)t}|\Psi\rangle$, which results from the scattering mechanism. The time-dependent density matrix of the

entire system is

$$|\Phi^{'}\rangle\langle\Phi^{'}| = \frac{1}{2}\Big(|g\rangle\langle g| \otimes |\Psi^{'}_{g}(t)\rangle\langle\Psi^{'}_{g}(t)| + |g\rangle\langle e| \otimes |\Psi^{'}_{g}(t)\rangle\langle\Psi^{'}_{e}(t)| + |e\rangle\langle g| \otimes |\Psi^{'}_{e}(t)\rangle\langle\Psi^{'}_{g}(t)| + |e\rangle\langle e| \otimes |\Psi^{'}_{e}(t)\rangle\langle\Psi^{'}_{e}(t)|\Big), \tag{4.20}$$

and the time dependent density matrix of the impurity can be calculated by tracing out the environment $\rho_s(t) = \mathrm{Tr}_{|\Psi\rangle}|\Phi^{'}\rangle\langle\Phi^{'}|$ which leads to

$$\rho_s(t) = \frac{1}{2}\Big(|g\rangle\langle g|\langle\Psi^{'}_{g}(t)|\Psi^{'}_{g}(t)\rangle + |g\rangle\langle e|\langle\Psi^{'}_{e}(t)|\Psi^{'}_{g}(t)\rangle + |e\rangle\langle g|\langle\Psi^{'}_{g}(t)|\Psi^{'}_{e}(t)\rangle + |e\rangle\langle e|\langle\Psi^{'}_{e}(t)|\Psi^{'}_{e}(t)\rangle\Big). \tag{4.21}$$

Taking into account the normalisation condition $\langle\Psi^{'}_{i}(t)|\Psi^{'}_{i}(t)\rangle = 1$ for $i = \{g, e\}$ and noting that the coherences of the reduced state are proportional to the scalar product

$$\langle\Psi^{'}_{g}(t)|\Psi^{'}_{e}(t)\rangle = \langle\Psi|e^{i\hat{H}t}e^{-i(\hat{H}+\hat{H}_I)t}|\Psi\rangle = \nu(t), \tag{4.22}$$

the reduced state can be written as

$$\rho_s(t) = \frac{1}{2}\Big(|g\rangle\langle g| + |g\rangle\langle e|\,\nu^{*}(t) + |e\rangle\langle g|\,\nu(t) + |e\rangle\langle e|\Big). \tag{4.23}$$

The equivalence with the time-propagator $\nu(t)$ highlighted in Eq. (4.10) proves a direct link between the decoherence of an impurity in a fermionic environment and the phenomenon of Anderson OC.

4.5 Entanglement

Given the formal connection between $\nu(t)$ and the impurity's dynamics, we can quantify the degree of entanglement within the state in Eq. (4.19) by means of the von Neumann entropy $S(t) = -\sum_i \lambda_i(t)\log_2\lambda_i(t)$, where $\lambda_i(t)$ are the time-dependent eigenvalues of $\rho_s(t)$, the reduced state of the impurity only. The time-dependent von Neumann entropy is shown in Fig. 4.5 for systems with different particle number and two different values of the interaction strengths. If the interaction energy is at or above the Fermi energy, as in Fig. 4.5**(a)**, it can be seen that after the interaction is switched on, the coupled system evolves into a fully entangled state ($S = 1$). This indicates that the many-particle state, created after the disturbance is switched on, almost immediately becomes orthogonal to the initial equilibrium state, as demanded by the catastrophe effect. It is remarkable to note that, already for a small number of particles, the state of the atomic gas is not separable at any time following the quench. The inset of Fig. 4.5**(a)** shows the entropy

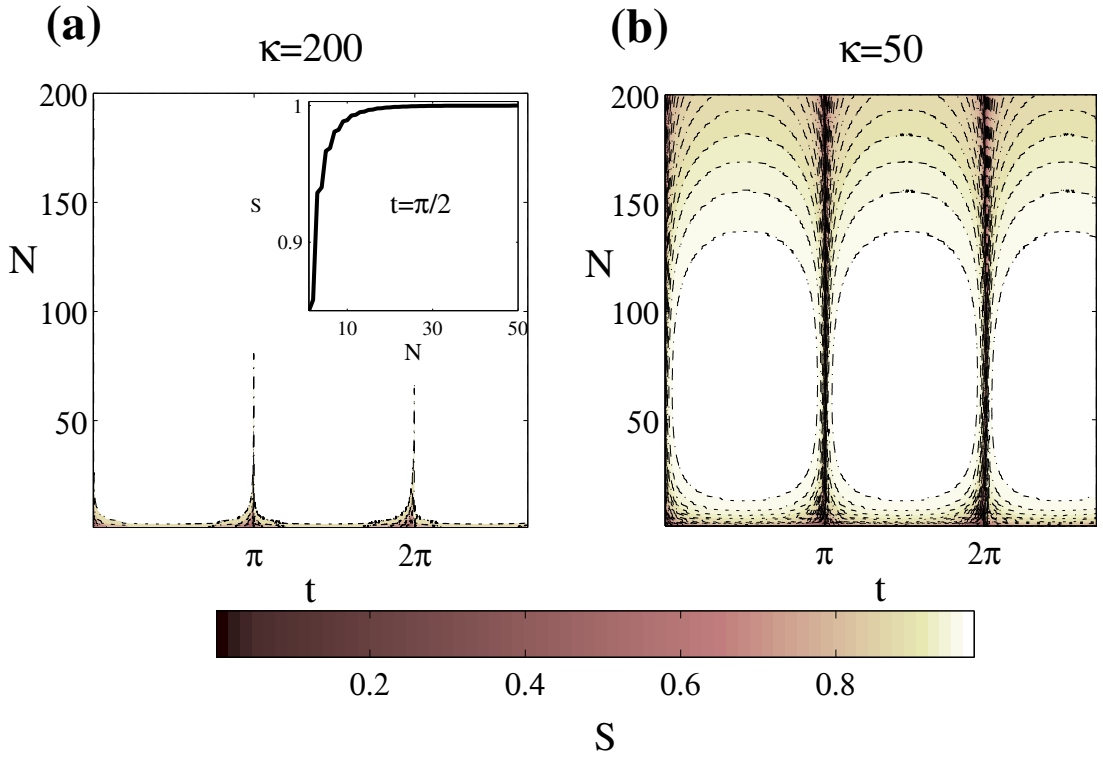


FIGURE 4.5: (Color online)**(a)** Time-dependent von Neumann entropy as a function of the particle number for $\kappa = 200$. The inset shows a time slice at $t = \pi/2$. **(b)** Time-dependent von Neumann entropy as a function of the particle number for $\kappa = 50$.

at a fixed moment in time, clearly indicating that the orthogonal state is already reached for a mesoscopic number of particles [$N \approx 15$ in Fig. 4.5**(a)**]. An interesting point to make is that, provided one has the ability to tune the coupling to a large value, the qualitative features shown above remain similar for even smaller Fermi environments. This is in contrast to the case of a metal where large particle numbers and relatively weak scattering strengths are in order. Fig. 4.5**(b)** shows the von Neumann entropy for the weaker value $\kappa = 50$ of the scattering strength. In this case, full orthogonality is established only for larger particle numbers and a maximally entangled state is achieved at $N = 50$. For $N > 125$ the strength of the perturbation is too weak to greatly disturb the higher states and the effect of the OC is seen to diminish.

4.6 Detection

Let us now show how the properties of our complex system-environment state can be directly inferred by looking at the system state only [141]. In particular, we suggest to use Ramsey interferometry on the atom to measure the time-dependent overlap $\nu(t)$ and, from it, the single-particle spectrum of the Fermi gas. As discussed previously, this spectrum is known to be strongly affected by the OC [130]. Spectral information will

therefore provide a definite signature of OC which can be easily compared to the original experiments in metals. Our scheme is based on a protocol put forward in Ref. [142]: after the creation of the entangled atom-environment state, we allow the hybrid system to freely evolve for a time t. During this time, a phase-shift gate is applied to the atom, such that $|g\rangle \to |g\rangle$ and $|e\rangle \to e^{i\phi}|e\rangle$, giving the state of the overall system as

$$|\Psi(t)\rangle = (|g\rangle \otimes e^{-i\hat{H}t}|\Psi\rangle + e^{i\phi}|e\rangle \otimes e^{-i(\hat{H}+H_I)t}|\Psi\rangle)/\sqrt{2}. \tag{4.24}$$

Using again a classical field, the state of the atom can be changed as

$$\begin{aligned} |g\rangle &\to (|g\rangle + |e\rangle)/\sqrt{2}\,, \\ |e\rangle &\to (|g\rangle - |e\rangle)/\sqrt{2}. \end{aligned} \tag{4.25}$$

We finally measure the probability for the atom to be found in $|g\rangle$, which reads

$$P_g(t,\phi) = [1 + \cos(\phi)\nu_R(t) - \sin(\phi)\nu_I(t)]/2, \tag{4.26}$$

where $\nu(t) = \nu_R(t) + i\nu_I(t)$ is the overlap entering the OC theory in Eq. (4.22). Eq. (4.26) is plotted for various different total particle numbers in Fig. 4.6. After the initial switching on of the qubit $P_g(t)$ starts to oscillate with a constant amplitude about $P_g(t) = 0.5$. The amplitude of these oscillations depends on the total particle number N and as with the Loschmidt echo it decreases for N large. Using, for example, resonance fluorescence techniques, $P_g(t,\phi)$ can be measured for various values of the phase ϕ and thus fitted to Eq. (4.26), from which the overlap function $\nu(t)$ can be extracted as a fitting parameter. The single-particle spectrum $A(\omega)$ can then be obtained from the Fourier transform on the time-dependent overlap $\nu(t)$, according to Eq. (4.8). A typical spectrum is shown in Fig. 4.7 and one can see that $A(\omega)$ exhibits almost identical features to those observed via X-ray absorption of metals [130]. First of all, the main peak has a finite height at the Fermi energy, which implies that the transition probability is not diverging anymore. Moreover, the spectrum is asymmetric with respect to the mean peak, showing that the 'emission' and 'absorption' rates are different at ω and $-\omega$, respectively. Physically, this means that the system is out of equilibrium and is trying to settle into a new state. Fig. 4.7 **(b)** shows that the logarithm of the tails of the spectrum decay following a power law (continuous blue line) instead of an exponential one (dashed red line), as it would be expected for a system at equilibrium.

The effect of a finite size impurity on the spectral function has also been explored, some results of which are presented in the left panel of Fig. 4.8, where a Gaussian potential is used with height $\kappa = 5000$ and widths $\sigma = 0.001$ and $\sigma = 0.01$ for a gas of $N = 100$ particles. In both cases the asymmetric broadening of the spectral function is preserved,

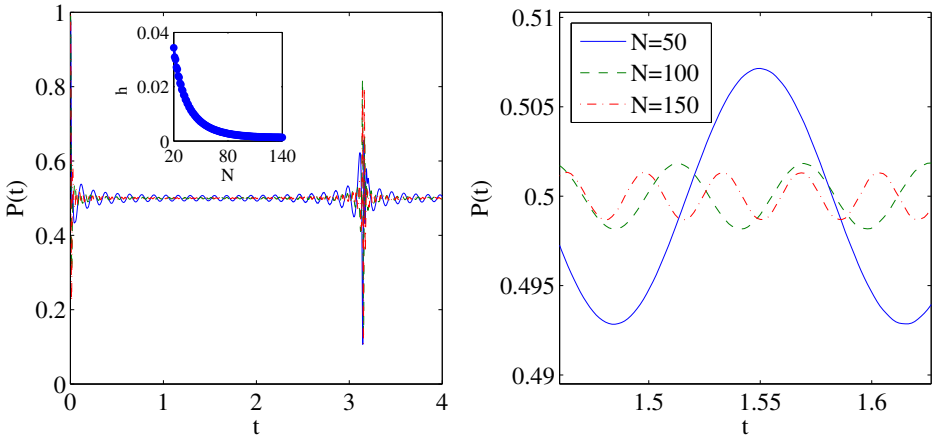


FIGURE 4.6: The probability for the qubit to be measured in the ground state $P_g(t)$ is plotted in the LHS panel for different particle numbers, $N = 50, 100, 150$. The inset shows the mean amplitude of the oscillations in the time period $\pi/2 - 0.25, \pi/2 + 0.25$ and how this changes with particle number showing the onset of the OC. The RHS panel is a magnification of $P_g(t)$ around $t = \pi/2$ which shows the change in amplitude of the oscillating probability for different particle numbers.

however the magnitude of the main peak is reduced as the width of the impurity is increased. The finite sized impurity excites not only the even but also the odd states of the harmonic trap, which leads to an increased number of peaks in the spectral function at large frequencies. Numerically this makes it difficult to capture all the excitation frequencies for $N > 50$ and $\sigma \geq 0.05$.

Modern experimental techniques allow for the opportunity to observe the OC in cold atoms highlighted by a recent experiment which has demonstrated a species-selective dipole potential trapping geometry that tightly localised an individual impurity (^{40}K) in a quasi-one-dimensional gas of on average 180 atoms (^{87}Rb) [143]. Although the atoms used in this specific experiment are bosonic, there is no reason such a setup cannot be used for fermionic samples. Alternatively, one can use a confinement-induced resonance to drive the atoms into the fermionized Tonks-Girardeau regime, where the Loschmidt echo is equivalent to that of non-interacting fermions [144].

4.7 Finite Temperature

The above argument holds for situations in which the Fermi gas is initially prepared in a pure state. However it is often the case that the gas has a thermal component and its

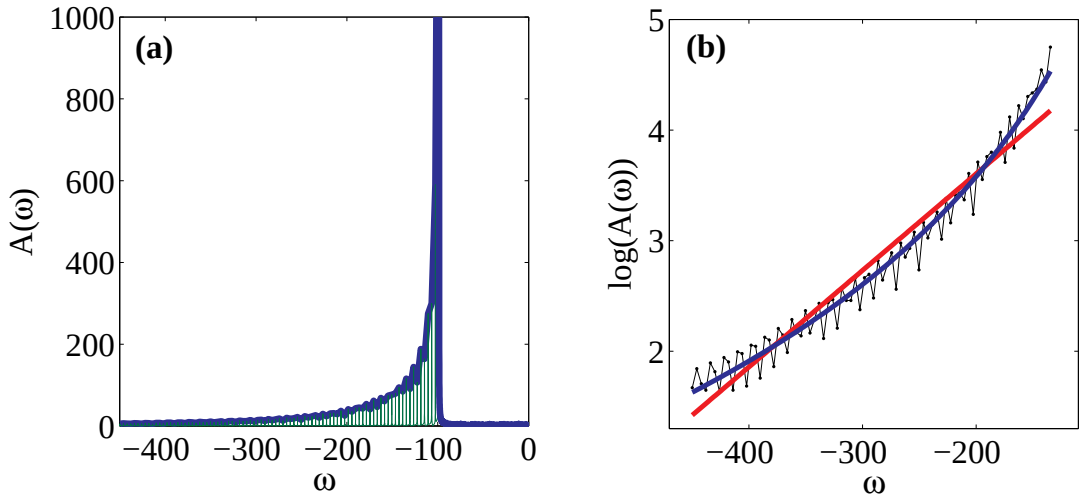


FIGURE 4.7: Spectral function. **(a)** The spectral function $A(\omega)$ for $N = 100$ and $\kappa = 100$ (δ function). The continuous blue curve is the envelope of the otherwise discrete spectrum. The asymmetry is clearly visible. **(b)** Comparison of the spectrum (black line) with an exponential (dashed red line) and a power-law fit (continuous blue line) with exponent -2.41.

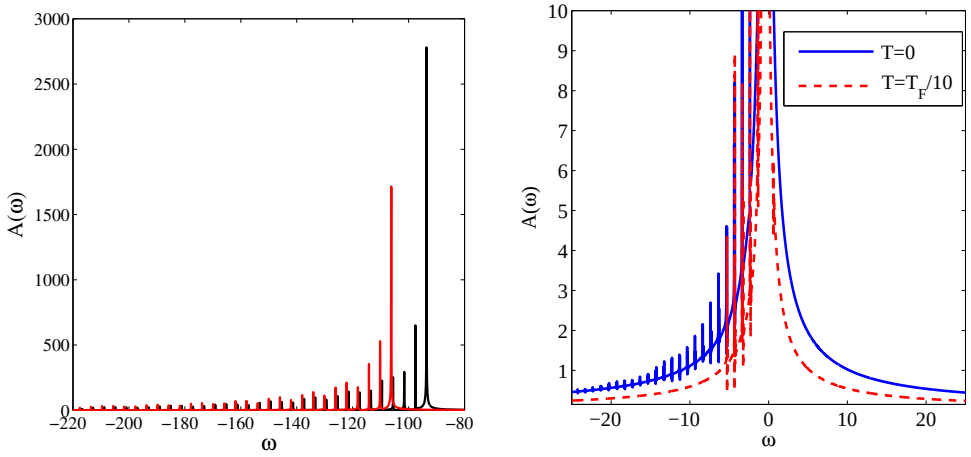


FIGURE 4.8: Left Panel: The spectral function $A(\omega)$ for $N = 100$. A Gaussian of height $\kappa = 5000$ and width $\sigma = 0.001$ (black Line) and $\sigma = 0.01$ (red line) is used for the perturbation. Right Panel: The effect of finite temperature for a system of $N = 7$ particles with $\kappa = 5$ is shown. The suppression given by the exponential coefficient appearing in Eq. (4.29) is evident as the spectrum for $T \neq 0$ has a lower amplitude than the one for $T = 0$.

quantum state is mixed. The overlap for mixed states is given by

$$\nu(t) = Tr(\hat{U}'(t)\hat{\rho}\hat{U}(-t)) \,, \tag{4.27}$$

where $\hat{U}(t) = e^{-i\hat{H}t}$ and $\hat{U}'(t) = e^{-i\hat{H}'t}$ are the corresponding unitary evolution operators which generate the dynamics in the unperturbed and perturbed system. In the case of an initial pure state one recovers $Tr(\hat{U}'(t)|\Psi\rangle\langle\Psi|\hat{U}(-t)) = \langle\Psi|\hat{U}(-t)\hat{U}'(t)|\Psi\rangle =$

$\langle\Psi(t)|\Psi'(t)\rangle$. Using the generalised overlaps in the previous section one may derive a formula which holds for a general class of initial mixed states,

$$\begin{aligned} Tr(\hat{U}^{'}(t)\hat{\rho}(0)\hat{U}(-t)) &= \sum_i \langle\Psi_i(X)|\hat{U}^{'}(t)\hat{\rho}(0)\hat{U}(-t)|\Psi_i(X)\rangle \\ &= \sum_i \langle\Psi_i(X)|\Big(\sum_j |\Psi_j^{'}(X)\rangle\langle\Psi_j^{'}(X)|\Big)\hat{U}^{'}(t)\hat{\rho}(0)\hat{U}(-t)|\Psi_i(X)\rangle \\ &= \sum_{i,j} \langle\Psi_n(X)|\Psi_j^{'}(X)\rangle\langle\Psi_j^{'}(X)|\hat{U}^{'}(t)\hat{\rho}(0)\hat{U}(-t)|\Psi_i(X)\rangle \\ &= \sum_{i,j} e^{-\imath(E_j^{'}-E_i)t}\langle\Psi_i(X)|\Psi_j^{'}(X)\rangle\langle\Psi_j^{'}(X)|\hat{\rho}(0)|\Psi_i(X)\rangle \ . \end{aligned} \tag{4.28}$$

Let us assume that the initial state of the gas is in thermal equilibrium, and can be described in the framework of the canonical ensemble, such that

$$\nu(t) = \mathrm{Tr}(\hat{U}^{'}(t)\hat{\rho}\hat{U}(-t)) = \sum_{i,j,l} C_l \Lambda^*_{j,i}\Lambda_{j,l}\, e^{-\imath\Delta_{j,i}t} \ , \tag{4.29}$$

with $C_l = e^{E_l/k_BT}/Z$ where $Z = \sum_j e^{-E_j/k_BT}$ and we have set $\Delta_{j,i} = E_j^{'} - E_i$. In the limit $k_BT \ll \mu_F$ where μ_F is the chemical potential, we get

$$\nu(t) = Tr(\hat{U}^{'}(t)\hat{\rho}(0)\hat{U}(-t)) = \sum_j |\Lambda_{j,0}|^2 e^{-\imath\Delta_{j,0}t}, \tag{4.30}$$

as in Eq. (4.10). We note that the Loschmidt echo is given by

$$|\nu(t)|^2 = \sum_{j,i} |\Lambda_{j0}|^2|\Lambda_{i0}|^2 e^{-\imath\Delta^{'}_{j,i}t} \ , \tag{4.31}$$

where $\Delta^{'}_{j,i} = E_j^{'} - E_i^{'}$ is the energy difference among the fermion-hole pairs as measured from the new Fermi energy $E_0^{'}$.

The influence of a finite temperature can lead to a blurring of the OC effect. One can see from Eq. (4.29) that its effect is two-fold: on the one hand it introduces new frequencies to the system, since now $\Delta_{m,n} \neq 0$ even for $n \neq 0$, which is manifested in a broadening of the spectrum. On the other hand exponential factors are introduced, namely $C_n = e^{-E_n/k_BT}/Z$, so that the heights of the peaks are exponentially suppressed (see right panel Fig. 4.8). This leads to a loss of the characteristic power law for the spectrum tails and therefore requires us to work at temperatures which are well below the Fermi energy in order to observe the OC effects.

4.8 Conclusions

In summary we have investigated the occurance of the OC in a system of ultracold fermions which can also describe the Tonks-Girardeau gas. For a time-independent system the catastrophe has been numerically observed for a harmonically trapped gas of fermions under the influence of a δ- function perturbation. We have shown that the OC plays an important role in the dynamics of coupled systems consisting of an ultracold atomic gas interacting with a single two-level system. In this respect, we have quantitatively linked the OC to the mechanism of decoherence undergone by the two-level system and signaled by the Loschmidt echo. The occurance of OC has also shown to be robust for mixed states at finite temperature and for impurities of finite width.

It should be stressed that, beside pointing out the exciting possibility to explore the OC in a realistic set-up radically different to the one originally envisaged by Anderson, the scenario addressed here demonstrates that the measurement of a single impurity allows one to obtain highly nontrivial information about the behaviour of a complex environment. Such information is invaluable for tasks of environmental characterization and interaction-identification, thus suggesting an ideal probe for testing ultracold atomic gases. In this sense, this work stands as the ultra-cold counterpart of the hallmark experiments in the X-ray absorption spectrum of metals while demonstrating, at the same time, the appropriateness of auxiliary quantum systems as probes for ultra-cold quantum gases.

4.9 Outlook

The behaviour of the overlap in many-body systems under the effect of both global and local perturbations of different forms is an interesting area which has been previously un-explored. The sudden change of the trapping frequency on the state can lead to intriguing results about the time evolving state of the system. The question would then be twofold: when does the average of the time evolving state reach its time average and does this give a good description of the out-of-equilibrium dynamics of the state?

Chapter 5

Effect of interparticle interaction in a free-oscillation atomic interferometer

5.1 Introduction

In all scientific pursuits accurate measurements are crucial, however measurements are beset by noise and uncertainty in the measurement apparatus. Interferometry is a powerful measurement technique which exploits wave phenomena to accurately measure distances and forces by measuring the phase difference that a wave has aquired after travelling along two different paths. However the precision of an interferometer to measure this phase is limited. In optical interferometry the number of photons, N, is the resource that is used to to increase the precision of an experiment. Classically the uncertainty in the measured phase $\delta\varphi$ scales as $1/\sqrt{N}$ and this is called the standard quantum limit (SQL). However interferometry using non-classical states (squeezed states and other strongly correlated states) can do much better than this and allows the uncertainty to scale with $1/N$, which is known as the Heisenberg limit. Optical interferometers, in comparison to their atomic counterparts, have been widely explored and can generate a wide range of entangled states, such as the NOON state [145–148]. The NOON state is a maximally entangled many-body state of the form

$$|\psi_{NOON}\rangle = \frac{1}{\sqrt{2}}\left(|N\rangle_a|0\rangle_b + |0\rangle_a|N\rangle_b\right), \tag{5.1}$$

and is a superposition of N particles in mode a with zero particles in mode b and zero particles in mode a with N particles in mode b. By using NOON states in interferometry

the uncertainty in parameter estimation can be minimized and the Heisenberg limit is reached. However a major drawback in optical setups is their short coherence times especially when compared to atomic ensembles [149]. As exploiting entanglement in order to enhance the measurement precision is the goal, maximizing coherence times is of paramount importance.

While making use of atomic ensembles can enhance the lifetime of a generated state there is an experimental cost, as such systems are often more difficult to control given current technologies [149]. Recently proposals using the strongly correlated Tonks-Girardeau gas to create macroscopic superpositions have emerged [150, 151] and some remarkable advances have been made by using Bose-Einstein condensates (BECs) as resources [152, 153]. Compared with thermal atoms, the ultra-cold atoms in BECs offer a greater control and can, for example, form atomic solitons whose non-dispersive properties can be exploited to create macroscopic superposition states for interferometry [154–157]. The established creation of BECs in harmonic traps has led to new interferometry designs which exploit the periodic dynamics of the particles to create Michelson and Mach-Zehnder interferometers [158–161]. Such schemes, which present a viable approach to atomic interferometry are referred to as free oscillation atom interferometers.

In this Chapter we take a similar approach. We start with two bosonic atoms held on one side of a harmonic trap split by a δ-potential. The atoms are then released and allowed to scatter off the barrier twice, thus realizing a Michelson type interferometer. By employing numerical diagonalization techniques we are able to exactly solve the model and show that by adjusting the height of the barrier one can generate a range of spatially entangled states of the atoms. While some studies have explored how different trapping geometries affect the performance of an interferometer, we rigorously assess the effects different interaction regimes have on the value of the states created. We measure this value by calculating the quantum Fisher information (QFI)[162], and show that for certain interaction strengths this simple setup can generate NOON states.

5.1.1 Quantum Fisher Information

In interferometry the goal is to estimate accurately a phase φ by minimizing the uncertainty of the estimated value φ_{est} [162],

$$\delta\varphi = \left\langle \left(\varphi_{est} \left| \frac{\delta\langle\varphi_{est}\rangle}{\delta\varphi} \right|^{-1} - \varphi \right)^2 \right\rangle^{\frac{1}{2}} . \tag{5.2}$$

The Cramér-Rao inequality gives a lower bound on this uncertainty

$$\delta\varphi \geq \frac{1}{\sqrt{\mathcal{F}}} \,, \tag{5.3}$$

where $\mathcal{F}$ is the Fisher information which is defined as

$$\mathcal{F} = \int \left(\frac{\partial}{\partial\varphi} \log p_\varphi(\varphi_{est}) \right)^2 p_\varphi(\varphi_{est})\, d\varphi_{est} \,. \tag{5.4}$$

The function $p_\varphi(\varphi_{est})$ is a probability function for φ_{est} which depends on the chosen φ. By replacing the probability function with the density operator $\rho(\varphi)$ the quantum Fisher information (QFI) can be obtained as

$$\mathcal{F}_Q = \mathrm{Tr}[\rho(\varphi) A^2] \,, \tag{5.5}$$

where A is a Hermitian operator known as the *symmetric logarithmic derivative* and defined by

$$\frac{\partial\rho(\varphi)}{\partial\varphi} = \frac{1}{2}[A\rho(\varphi) + \rho(\varphi)A] \,. \tag{5.6}$$

It can be written in the eigenbasis of $\rho(\varphi)$ as

$$(A)_{ij} = \frac{2}{\lambda_i + \lambda_j}[\rho^{'}(\varphi)]_{ij}, \tag{5.7}$$

where λ_i are the eigenvalues of $\rho(\varphi)$ and we have labelled $\rho^{'}(\varphi) = \frac{\partial\rho(\varphi)}{\partial\varphi}$. For the case of $\lambda_i + \lambda_j = 0$ we define $(A)_{ij} = 0$ [150, 163].

The quantum Cramér-Rao bound can now be defined in term of the QFI as

$$\delta\varphi \geq \frac{1}{\sqrt{\mathcal{F}}} \geq \frac{1}{\sqrt{\mathcal{F}_Q}} \,, \tag{5.8}$$

indicating that the QFI defines the amount of information an observable knows about an unknown parameter. A state with maximal QFI will minimize $\delta\varphi$ and will allow us the most sensitive measurement.

For a pure state $\rho(\varphi) = |\psi(\varphi)\rangle\langle\psi(\varphi)|$ the *symmetric logarithmic derivative* takes the form of

$$A = 2\left(|\psi(\varphi)\rangle\langle\psi^{'}(\varphi)| + |\psi^{'}(\varphi)\rangle\langle\psi(\varphi)| \right) , \tag{5.9}$$

from which the QFI follows

$$\begin{aligned} \mathcal{F}_Q = 4\ \mathrm{Tr}\Big(& |\psi(\varphi)\rangle\langle\psi^{'}(\varphi)|^2 + |\psi(\varphi)\rangle\langle\psi^{'}(\varphi)|\psi^{'}(\varphi)\rangle\langle\psi(\varphi)| + \\ & |\psi(\varphi)\rangle\langle\psi(\varphi)|\psi^{'}(\varphi)\rangle\langle\psi(\varphi)|^2 + |\psi(\varphi)\rangle\langle\psi(\varphi)|\psi^{'}(\varphi)\rangle\langle\psi^{'}(\varphi)| \Big) \,. \end{aligned} \tag{5.10}$$

Performing the trace results in

$$\begin{aligned}\mathcal{F}_Q = 4\Big(&|\langle\psi^{'}(\varphi)|\psi(\varphi)\rangle|^2 + \langle\psi^{'}(\varphi)|\psi^{'}(\varphi)\rangle + \\ &|\langle\psi(\varphi)|\psi^{'}(\varphi)\rangle|^2 + \langle\psi(\varphi)|\psi^{'}(\varphi)\rangle\langle\psi^{'}(\varphi)|\psi(\varphi)\rangle\Big)\,,\end{aligned} \tag{5.11}$$

and using $\langle\psi(\varphi)|\psi^{'}(\varphi)\rangle = -\langle\psi^{'}(\varphi)|\psi(\varphi)\rangle$ the quantum Fisher information for a pure state is

$$\mathcal{F}_Q = 4\Big(\langle\psi'(\varphi)|\psi'(\varphi)\rangle - |\langle\psi'(\varphi)|\psi(\varphi)\rangle|^2\Big). \tag{5.12}$$

For separable states the maximum QFI is N, which is the number of particles (or quanta) we are using in our interferometer and this corresponds to the standard quantum limit, given by $\delta\varphi = 1/\sqrt{N}$. However we can go beyond this limit by using entangled particles which can yield a maximum QFI of N^2, which is the Heisenberg limit, $\delta\varphi = 1/N$. As mentioned previously this limit is reached by one particularly important class of states, the NOON state,

$$|\psi_{NOON}\rangle = \frac{1}{\sqrt{2}}\left(|N\rangle_a|0\rangle_b + |0\rangle_a|N\rangle_b\right). \tag{5.13}$$

In our scheme we will consider two particles only and we are interested in spatial correlations of this two-particle state. The system we are investigating is a harmonic trap which is separated into two distinct regions by a barrier which is placed at its origin. In this case the NOON state corresponds to both particles being simultaneously on the left-hand side (LHS) $\Big[|2\rangle_L|0\rangle_R\Big]$, or $|20\rangle$, and right-hand side (RHS) $\Big[|0\rangle_L|2\rangle_R\Big]$, or $|02\rangle$, of the barrier. After colliding with the barrier the state can then be described as

$$\psi = a|20\rangle + b|11\rangle + c|02\rangle \tag{5.14}$$

where a, b and c are the weights of the different components and $a^2 + b^2 + c^2 = 1$. Consider an interferometry experiment where one adds a phase φ to one arm of the interferometer. This yields

$$\psi(\varphi) = a|20\rangle + b|11\rangle e^{i\varphi} + c|02\rangle e^{2i\varphi} \tag{5.15}$$

with the derivative given by

$$\psi'(\varphi) = ib|11\rangle e^{i\varphi} + 2ic|02\rangle e^{2i\varphi}. \tag{5.16}$$

This allows one to calculate the QFI by simply multiplying sections of the two-body wavefunction by a complex factor. The final result for the QFI is real and does not depend on φ and is given by

$$\mathcal{F}_Q = 4\left(b^2 + 4c^2 - |b^2 + 2c^2|^2\right)\,. \tag{5.17}$$

5.1.2 Von Neumann Entropy

As the NOON state is a bi-partite entangled state we will also make use of the von Neumann entropy (vNE) to quantify the entanglement of the atoms. Recall from Chapter 2 that it is defined by the entropy of the reduced single particle density matrix, ρ, as

$$S(\rho) = \mathrm{Tr}[\rho \log_2 \rho] = -\sum_i \lambda_i \log_2 \lambda_i \tag{5.18}$$

where the λ_i are the eigenvalues of the single particle density matrix,

$$\int \rho(x_1, x_2)\chi_i(x_2)dx_2 = \lambda_i \chi_i(x_1) \; . \tag{5.19}$$

The vNE will measure the total entanglement present, accounting for both inter-particle and spatial entanglement, and as such will present some qualitative differences to the QFI.

Due to the indistinguishability of bosons one must be careful when dealing with the vNE as an entanglement measure in certain situations. As noted by Murphy *et al* [164] for two strongly repulsive trapped bosons, a value of vNE ≈ 1 does not imply any genuine entanglement to be present. The seemingly large vNE can be attributed as a pathological occurrence due to exploiting the Bose-Fermi mapping and treating the atoms as non-interacting fermions in this regime which requires anti-symmetrization of the wave function. The stationary situation considered by Murphy *et al* [164], in which a barrier splits the trap and the indistinguishability of bosons results in the situation of one boson occupying each side of the trap, gives rise to a non-zero vNE. However in our case, the dynamical scattering process and constant interaction between the particles ensures the generated state is genuinely entangled and not a by-product of indistinguishability.

5.2 Preliminaries

5.2.1 The Model

The atomic interferometer we consider is a harmonic trap punctuated centrally by a δ-function potential of variable height. The δ-function barrier will act as a beam splitter for the interacting atoms, and for numerical simplicity we restrict our investigation to the case of two particles. We assume the trap is such that only longitudinal motion is

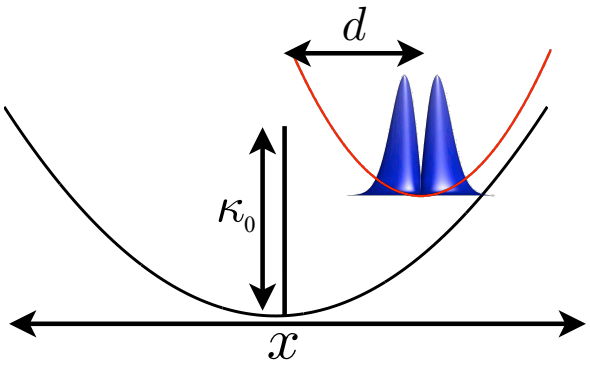


FIGURE 5.1: Schematic of the atom interferometer. The two atoms are initially trapped in a separate harmonic potential (indicated by the red line) at a distance d from the barrier of height κ_0. They are then released from this preparatory trap and are allowed to evolve in the new trap gaining velocity and colliding with the barrier. This motion is repeated cyclically due to the harmonicity of the trap.

permitted and transverse motion is tightly restricted, thus forming an effectively one-dimensional system. The Hamiltonian is then given by

$$\mathcal{H}_\Omega = \sum_{n=1}^{2}\left(-\frac{\hbar^2}{2m}\frac{\partial^2}{\partial x_n^2} + \frac{1}{2}m\Omega^2 x_n^2 + \kappa_0\delta(x_n)\right) + V\left(|x_1 - x_2|\right), \tag{5.20}$$

with m being the mass of each particle, Ω the harmonic potential frequency of the interferometry trap and κ_0 is the height of the δ-function barrier. The boson-boson interaction, V, can be well approximated by a point-like potential [165], which is given by

$$V\left(|x_1 - x_2|\right) = g_{1D}\ \delta\left(|x_1 - x_2|\right), \tag{5.21}$$

with g_{1D} the one-dimensional coupling constant between the particles defined in terms of the three-dimensional scattering length as discussed previously in Section 1.2.3. This parameter will be central in our analysis of different regimes and can be experimentally tuned by applying a Feshbach resonance, a powerful technique that is well established in cold atomic physics [166].

Initially the two atoms are prepared in a seperate tight harmonic trap a distance d from the centre of the interferometer trap (see Fig. 5.1) with the Hamiltonian given by

$$\mathcal{H}_\omega = \sum_{n=1}^{2}\left(-\frac{\hbar^2}{2m}\frac{\partial^2}{\partial x_n^2} + \frac{1}{2}m\omega^2(x_n - d)^2\right) + g'_{1D}\left(|x_1 - x_2|\right)\ . \tag{5.22}$$

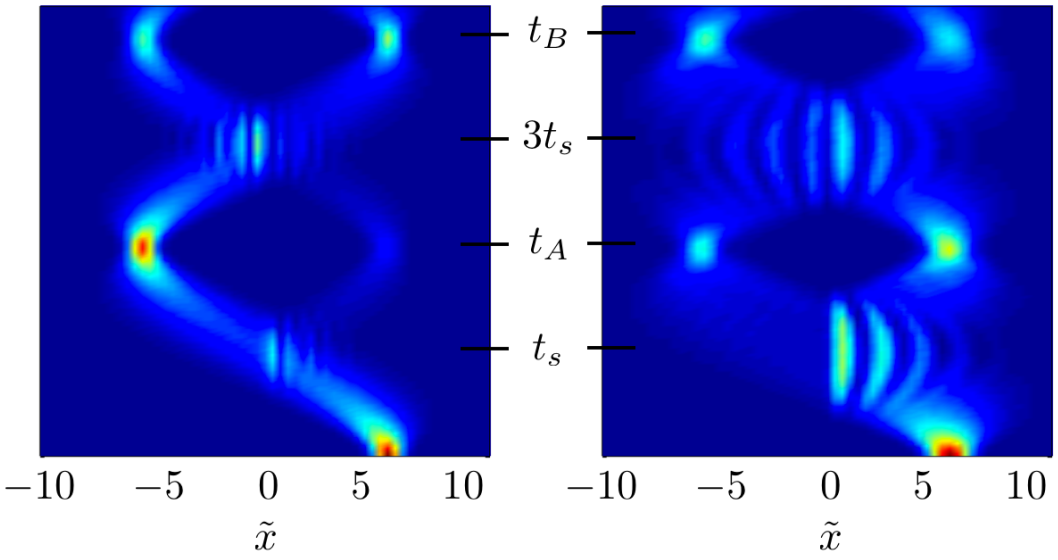


FIGURE 5.2: Single particle density versus time for two attractive (left-hand side panel) and two repulsive atoms (right-hand side panel). The barrier is positioned at $x = 0$ and the two particles are initially trapped at $d = 6$ with $\epsilon = 5.164$. At time t_s the particles scatter off the barrier and come to rest at time t_A at the first turning point. At time $3t_s$ the atoms recombine and scatter a second time and come to rest again at time t_B.

Here ω is the trap frequency of the preparatory trap and the interaction strength g'_{1D} is modified from g_{1D} to reflect this. In the following we will make use of scaled units such that the coordinates are rescaled with respect to the ground state of the harmonic oscillator of the interferometer trap, $\tilde{x}_n = x_n/a_\perp$ and the energy is scaled in units $\tilde{E}_n = E_n/(\hbar\Omega)$. Thus,

$$\tilde{\mathcal{H}}_\Omega = \sum_{n=1}^{2}\left(-\frac{1}{2}\frac{\partial^2}{\partial\tilde{x}_n^2} + \frac{1}{2}\tilde{x}_n^2 + \kappa\delta\left(\tilde{x}_n\right)\right) + g\ \delta\left(|\tilde{x}_1 - \tilde{x}_2|\right), \tag{5.23}$$

$$\tilde{\mathcal{H}}_\omega = \sum_{n=1}^{2}\left(-\frac{1}{2\epsilon}\frac{\partial^2}{\partial\tilde{x}_n^2} + \frac{1}{2}\epsilon\left(\tilde{x}_n - \tilde{d}\right)^2\right) + g\ \delta\left(|\tilde{x}_1 - \tilde{x}_2|\right), \tag{5.24}$$

where $\epsilon = \omega/\Omega$ is the ratio of the frequencies of the preparatory trap and the interferometer trap and $g = g_{1D}a_\perp = g'_{1D}a_\perp/\epsilon^2$ and $\kappa = \kappa_0 a_\perp$.

In order to solve the Hamiltonians, $\tilde{\mathcal{H}}_\Omega$ and $\tilde{\mathcal{H}}_\omega$, we must determine the single particle eigenstates and associated energies. For the time-independent Schrödinger equation for the preparatory trap is

$$\tilde{\mathcal{H}}_\omega\psi(\tilde{x_1}, \tilde{x_2}) = \tilde{E}'_n\psi_n(\tilde{x_1}, \tilde{x_2})\ . \tag{5.25}$$

This can be solved by taking advantage of the separability of the hamiltonian into centre of mass and relative coordinate systems, for which the solutions are known [137].

The time-independent Schrödinger equation for the interferometer trap,

$$\tilde{\mathcal{H}}_\Omega \phi_n(\tilde{x_1}, \tilde{x_2}) = \tilde{E}_n \phi(\tilde{x_1}, \tilde{x_2}) \ , \tag{5.26}$$

does not allow for factorisation due to the interaction term and we solve it numerically using the discrete variable representation (DVR) method [167, 168].

5.2.2 Discrete Variable Representation (DVR)

The DVR method allows to exactly diagonalize a many body Hamiltonian and scales as ${N_p}^{N^2}$, where N_p is the number of grid points taken in configuration space. While this is numerically intensive for the large values of N it is possible for small numbers of particles and we restrict ourselves here to $N = 2$. In the DVR the two-particle wavefunction is represented by the direct product [167, 168]

$$\phi(x_1, x_2) = \sum_{i,j=1}^{N_p} \phi_{ij} f_i(x_1) f_j(x_2) \ , \tag{5.27}$$

where ϕ_{ij} is the value of the two-body wavefunction at the mesh points $x_1 = q_i$ and $x_2 = q_j$ with $i, j = 1, 2, ..., N_p$ which are restricted by arbitrary boundaries a and b in (x_1, x_2) such that

$$a < q_i < b. \tag{5.28}$$

The $f_i(q)$ are a set of N_p Langrange functions which satisfy the following interpolation and orthogonality conditions

$$f_i(q_j) = \delta_{ij} \quad \forall \ i, j, \tag{5.29}$$

$$\int_a^b f_i^*(q) f_j(q) dq = \lambda_i \delta_{ij} \ , \tag{5.30}$$

where the λ_i are the generalised Christoffel numbers associated with the mesh, in this case $\lambda_i = 1 \quad \forall \ i$. Using this technique it is possible to rewrite the time-independent Schrödinger equation as a set of discretised linear simultaneous equations given by

$$\sum_{k,l=1}^{N_p} \left(T_{ik}\delta_{jl} + T_{jl}\delta_{ik} + \left[V_k + V_l \right] \delta_{ik}\delta_{jl} + g_{1D}\delta_{il}\delta_{jl}\delta_{kl} + \right) \phi_{kl} = E \, \phi_{ij} \ , \tag{5.31}$$

where $V_i = \frac{1}{2} q_i^2 + \kappa \delta(q_i)$ and T_{ij} is the kinetic energy matrix defined as

$$T_{ij} = (\lambda_i \lambda_j)^{-1/2} \int_a^b f_i^*(q) \left[-\frac{1}{2} \frac{d^2}{dq^2} \right] f_j(q) dq. \tag{5.32}$$

As we are using a Cartesian mesh the Lagrange functions are given by

$$f_i(q) = \frac{1}{N_p} \frac{\sin[\pi(q - q_i)]}{\sin[\pi(q - q_i)/N_p]} \ , \tag{5.33}$$

and the kinetic energy matrix elements reduce to

$$T_{ij} = \begin{cases} \frac{\pi^2}{6}\left(1 - \frac{1}{N_p^2}\right) \ , & \text{if } i = j \ , \\ (-1)^{i-j} \frac{\pi^2}{N_p^2} \frac{\cos[\pi(q_i - q_j)/N_p]}{\sin^2[\pi(q_i - q_j)/N_p]} \ , & \text{if } i \neq j \ . \end{cases} \tag{5.34}$$

This allows one to numerically diagonalize Eq. (5.31) and directly find the two-particle eigenfunctions and energies.

5.2.3 Time Evolution

Time evolution is achieved by constructing the time dependent wave function in terms of the eigenstates of the Hamiltonian $\tilde{\mathcal{H}}_\Omega$

$$\psi_m(\tilde{x}_1, \tilde{x}_2, t) = \sum_{n=0}^{\infty} a_{mn} \phi_n(\tilde{x}_1, \tilde{x}_2) e^{-i\tilde{E}_n t} \ , \tag{5.35}$$

where

$$a_{mn} = \int \psi_m(\tilde{x}_1, \tilde{x}_2) \phi_n(\tilde{x}_1, \tilde{x}_2) d\tilde{x}_1 d\tilde{x}_2 \ , \tag{5.36}$$

is the overlap of the individual solutions to the Hamiltonians. Due to the atoms' initial potential energy they will gain velocity, scatter at the barrier at time $t_s = \pi/2\Omega_\delta$ (*scattering A*) and return to the classical turning points of the trap at $t_A = \pi/\Omega_\delta$ (see the dynamics of the single particle density in Fig. 5.2). Here $\Omega_\delta \leq \Omega$ is an effective trap frequency adjusted to the presence of the δ-function barrier. At time $3t_s = 3\pi/2\Omega_\delta$ the atoms scatter a second time (*scattering B*) and again return to the classical turning points at $t_B = 2\pi/\Omega_\delta$. This setup resembles an atomic Michelson interferometer. While the following analysis can easily be performed by describing the barrier with a well localised potential of any shape, the choice of a δ-function is done to clearly isolate the interesting physical effects and does not constitute any loss of generality. A δ-function potential is a good approximation to a localised laser potential or an interaction with an atomic impurity fixed at $x = 0$ [82]. In the first case the barrier height κ can be experimentally tuned by changing the laser intensity, whereas in the second case a Feshbach resonance can be employed. This, coupled with the capacity to alter the inter-particle interaction, means we have a highly adaptable system with which to create superposition states.

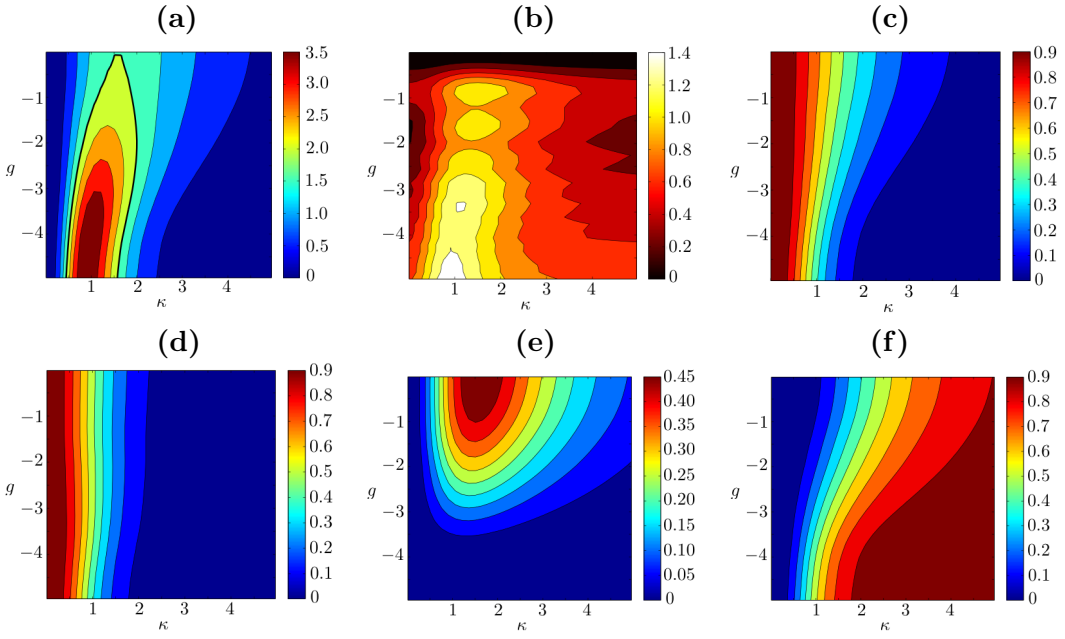


FIGURE 5.3: Contour plots for the **(a)** QFI, **(b)** vNE, **(c)** transmission coefficient (T), and population coefficients for states **(d)** $|20\rangle$, **(e)** $|11\rangle$ and **(f)** $|02\rangle$ plotted against attractive interaction strength g and barrier height κ at time t_A. At this time the atoms have reached the classical turning point after scattering once off the barrier (*Scattering A*). The ratio of trapping frequencies is chosen to be $\epsilon = 5.164$.

5.3 Analysis of different interaction regimes

5.3.1 Attractive Interactions

5.3.1.1 Scattering A

Let us discuss the case of an attractive dimer scattering once off the δ-barrier. In Fig. 5.3 **(a)** the QFI against attractive interaction strength, g, and barrier height κ is shown. The thick bold line signifies the classical shot noise limit $\mathcal{F}_Q = N = 2$ of the QFI, which is attainable for separable states. Interestingly one can see that even for a weakly interacting dimer this bound can be exceeded. As the attractive interactions between the atoms are increased, the QFI grows to its maximal obtainable value of $\mathcal{F}_Q = N^2 = 4$ for a barrier height of $\kappa \approx 1$. In panel **(b)** we see that the behavior of the vNE is qualitatively in agreement, although more complex. The small scale details are due to the interaction leading to a constantly varying inter particle entanglement, which is not captured in the calculation of the QFI. Looking at the transmission coefficient T, Fig. 5.3 **(c)**, it can be seen that the parameters giving $T = 0.5$ are the same ones that give the maximum of the QFI, which corresponds to the density profile in which the atoms are split equally by the scattering process. We can confirm that the state generated in

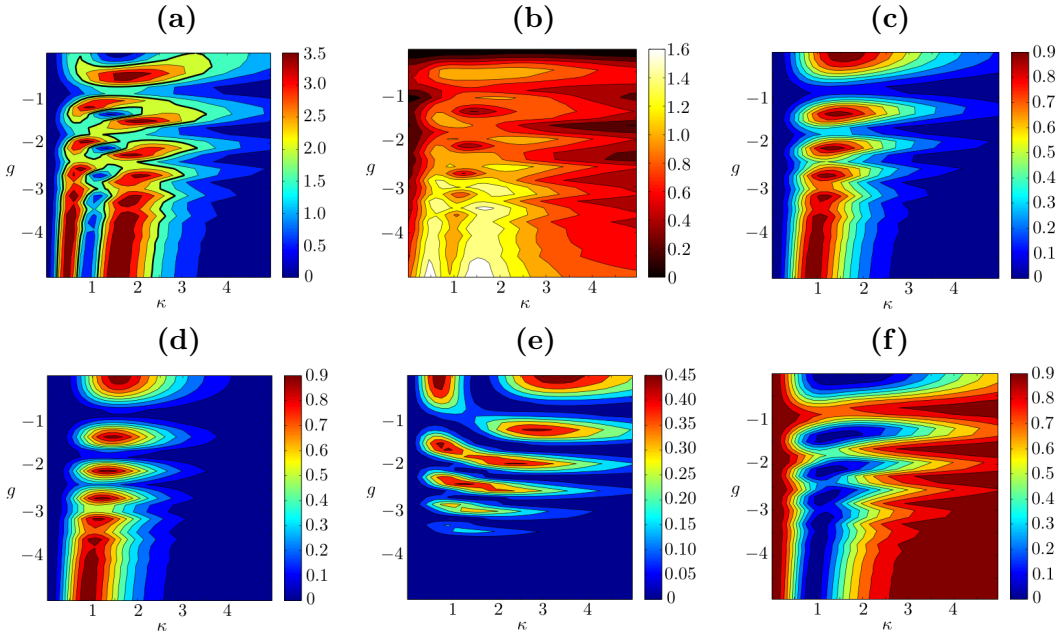


FIGURE 5.4: Contour plots for the **(a)** QFI, **(b)** vNE, **(c)** transmission coefficient (T), and population coefficients for states **(d)** $|20\rangle$, **(e)** $|11\rangle$, and **(f)** $|02\rangle$ plotted against attractive interaction strength g and barrier height κ at time t_B. At this time the atoms have reached the classical turning point after scattering twice off the barrier (*Scattering B*). The ratio of trapping frequencies is chosen to be $\epsilon = 5.164$.

this situation is the NOON state $\frac{1}{\sqrt{2}}(|20\rangle + |02\rangle)$ by looking at the various population coefficients, Figs. 5.3 **(d)-(f)**. The region in which the QFI is maximized corresponds to the one where the $|11\rangle$ state is surpressed and the $|20\rangle$ and $|02\rangle$ states are equally populated. This can be explained by the relatively strong attractive interaction within the dimer. In this region the bonds cannot be broken and hence the pair of atoms does not split into one atom on the left and one on the right. This situation is analogous to atomic solitons which have been studied extensively in the literature [154, 157], and where it was shown that macroscopic superposition states can be created by moving an atomic soliton through a barrier of finite width. Due to the attractive interactions between the constituent atoms the soliton is known to retain its density profile and atom number after collision with the barrier and thus allow for creation of NOON states.

5.3.1.2 Scattering B

After the second scattering process the dynamics becomes more complex for an attractive dimer. Examining the QFI (see Fig. 5.4 **(a)**) it can be seen that even for weakly attractive particles we can attain $\mathcal{F}_Q \approx 4$. As the interaction strength is increased the QFI peaks at two values of barrier height, κ. The behavior of the vNE is shown to be qualitatively similar in panel **(b)**. This behavior is also mirrored in the dynamics of the transmission

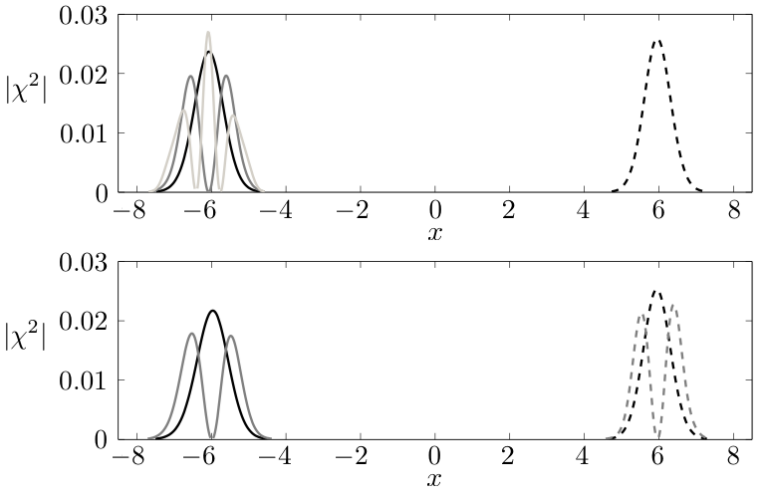


FIGURE 5.5: The first four orbitals of an attractive dimer are plotted at times t_A [top panel] and t_B [bottom panel]. At t_A three orbitals occupy the LHS of the trap and one on the RHS. Due to the strong attractive interaction the dimer is tightly bound and cannot be split, hence there is only a reflection probability of 0 or 1 for each orbital for large negative g. At t_B the orbitals pair up due to the double degeneracy and two orbitals occupy the LHS and RHS of the trap with similar density profiles.

coefficient, T [cfr. panel **(c)**], and we find that $T = 0.5$ corresponds to a maximum in the QFI. The most striking feature is clearly the intricate series of maxima appearing in all panels. These stem from the phase accumulated by the atoms due to their attractive interaction and for increased interaction the phase of the dimer oscillates faster which results in the interference pattern. We see the same qualitative behavior in the various population coefficients shown in Fig. 5.4 **(d)-(f)**, where the maximum QFI corresponds, as expected, to a suppression of the $|11\rangle$ state. Interestingly the value of κ which resulted in a maximum QFI for *Scattering A* results in a minimum in QFI for *Scattering B* for the same value of interaction strength. This can be explained by studying the behaviour of the atomic orbitals for the parameter values concerned.

For the maximum achieved QFI in this regime, corresponding to $g = -5$ and $\kappa \approx 1.5$, Fig. 5.5 shows the four lowest energy atomic orbitals obtained by diagonalizing the RSPDM, χ, to confirm if a superposition is created at times t_A [top panel] and t_B [bottom panel]. At t_A three orbitals can be seen occupying the LHS of the trap, which stems from the large attractive interaction leading to the transmission coefficient becoming $T = 0$ or 1. Even though each orbital occupies separate sides of the trap this is not a NOON state as explained by the orbital occupation numbers in Fig. 5.6 **(a)** which shows that at t_A the lowest orbital is still maximally occupied and all higher orbitals have lower occupation. At time t_B (see the bottom panel of Fig. 5.5) the two orbitals can be seen to each occupy a separate side of the trap. The occupation numbers of these orbitals start to become doubly degenerate leading to a QFI of $\mathcal{F}_Q = N^2$, see Fig. 5.6 **(b)**. This

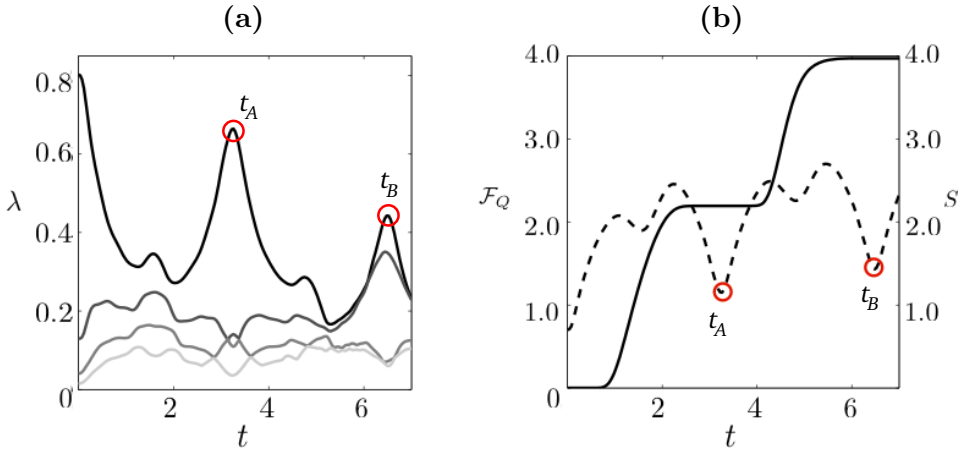


FIGURE 5.6: **(a)** The orbital occupation numbers are plotted versus time for an attractive interaction. At time t_B the orbitals become doubly degenerate meaning that both particles are in an equal superposition of being on the LHS and RHS of the trap simultaneously. **(b)** The behaviour of the Fisher information (solid) and entropy (dashed) are plotted versus time. The maximum F_Q reached is N^2 meaning a NOON state is created.

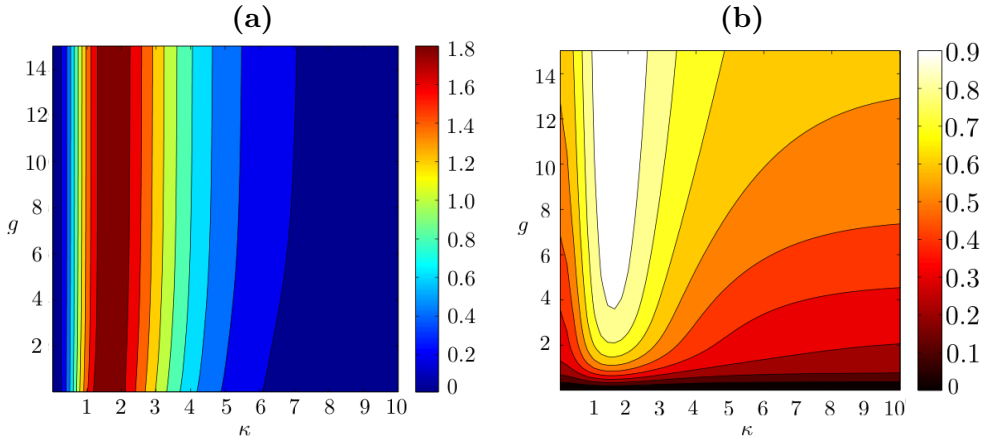


FIGURE 5.7: Contour plots for the **(a)** QFI and **(b)** vNE plotted against repulsive interaction strength g and barrier height κ at time t_A, corresponding to the classical turning point after scattering once off the barrier (*Scattering A*).

degeneracy of eigenvalues of the density matrix indicates that two equal sub-states exist in this case, which makes the overall state $\frac{1}{\sqrt{2}}(|20\rangle + |02\rangle)$. In Fig. 5.6 **(b)** the dashed line shows the dynamically changing vNE, which has two pronounced dips exactly at t_A and t_B. This is due to the fact that the vNE measures the total entanglement. At these classical turning points the relative inter-particle interaction is at its weakest and thus the drop in the entanglement.

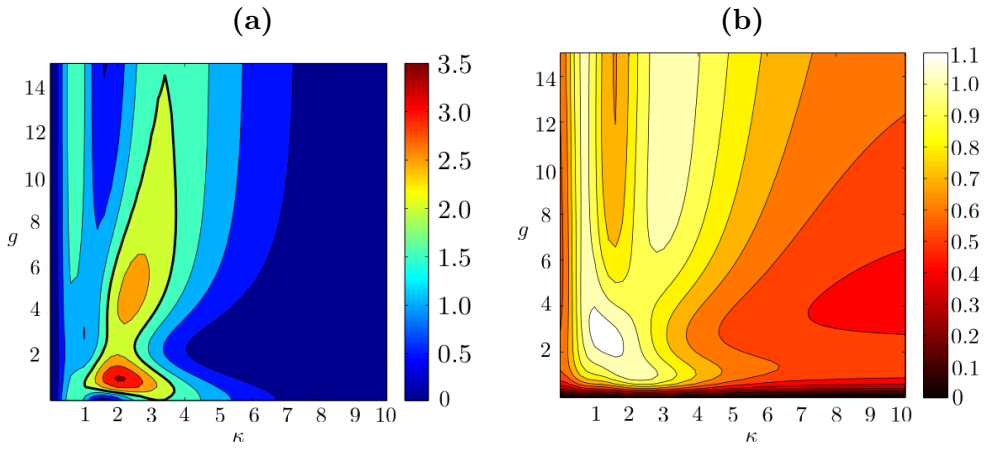


FIGURE 5.8: Contour plots for the **(a)** QFI and **(b)** vNE plotted against repulsive interaction strength g and barrier height κ at time t_B, corresponding to the classical turning point after scattering twice off the barrier (*Scattering B*).

5.3.2 Repulsive Interactions

5.3.2.1 Scattering A

We now turn our attention to the case of repulsive interaction between the atoms. This regime gives rise to behaviours that do not promote the generation of spatial entanglement easily as the repulsive nature prefers a situation in which one atom occupies each side of the trap. Fig. 5.7 **(a)** shows that the QFI remains below 2 for the whole range of parameter space considered. After the first scattering event examining the vNE (see Fig. 5.7 **(b)**) we see it attains a maximum of approximately 1, reached only for strongly repulsive atoms. The maximum $\mathcal{F}_Q = 2$ occurs for a barrier height $\kappa \approx 1.5$ regardless of the interaction strength g, reaching the classical limit for a transmission coefficient of $T = 0.5$.

5.3.2.2 Scattering B

Similar to the attractive interaction case the dynamics becomes much richer after the second scattering process due to the phase acquired by the various components of the two-particle state. It is now possible to generate states with $\mathcal{F}_Q > 2$, however it is within a much more restricted area of the parameter space when compared to the attractive interaction. In Fig. 5.8 it can be seen that for small repulsive interactions a QFI of $\mathcal{F}_Q > 3.5$ can be reached and the vNE shows qualitatively similar behaviour. As the interaction strength g is increased the particles enter the Tonks-Girardeau (TG) regime and for strongly repulsive atoms the QFI approaches its classical limit of 2 corresponding to the state $|\psi\rangle = \frac{1}{2}|20\rangle + \frac{1}{\sqrt{2}}|11\rangle + \frac{1}{2}|02\rangle$ resulting from a 50/50 splitting.

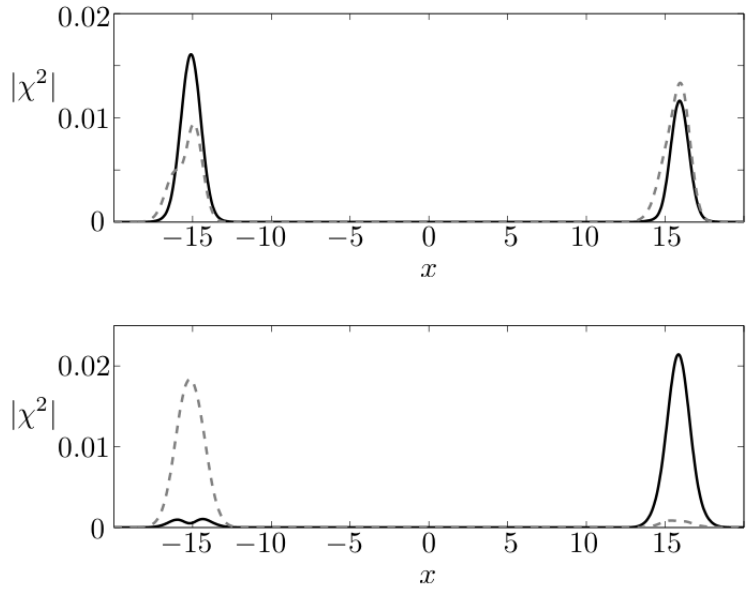


FIGURE 5.9: Atomic orbitals of the reduced single particle density matrix at times t_A [top panel] and t_B [bottom panel] with a repulsive interaction. At t_A each orbital has equal probability to be in the LHS or RHS of the trap. At t_B each orbital is at opposite sides of the trap, indicating a highly entangled quasi-NOON state.

For the optimal case, $g = 1.5$, we examine the first two atomic orbitals to determine the type of state generated in Fig. 5.9 at t_A [top panel] and t_B [bottom panel]. At t_A each orbital occupies both sides of the trap with nearly equal probability due to the 50/50 splitting at the barrier and corresponds to $F_Q \approx N$. At t_B the orbitals almost fully occupy different sides of the trap and their occupation numbers approach double degeneracy indicating the presence of a superposition state which leads to $\mathcal{F}_Q = 3.883$ (see Fig. 5.10).

5.3.3 Case $\epsilon = 1$

The behaviour of the vNE, $S(t)$, shown in Fig. 5.6 can be further understood by considering the case where the initial preparatory potential for the atoms has the same trapping frequency as the interferometer trap, i.e. $\epsilon = 1$. In this case no relative motion between the atoms exist in the interferometer and one can expect the von Neumann entropy to be constant whenever the particles are far from the barrier. This is illustrated in the right-hand side panel of Fig. 5.11 where the QFI and von Neumann entropy are plotted versus time for $\epsilon = 1$. It is clear that whenever the QFI increases an increase in the entanglement of the state has to be found in the von Neumann entropy as well. However far from the barrier the overall entanglement of the state remains constant as do the eigenvalues of the RSPDM, $\lambda_i(t)$ (see left-hand side panel of Fig. 5.11). Before time t_s the von Neumann entropy is constant which one would expect from unitary evolution.

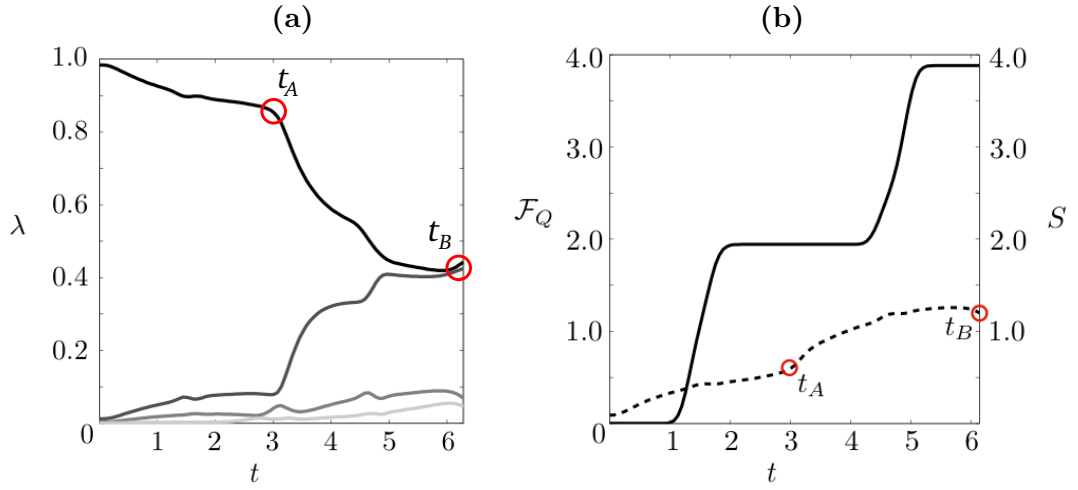


FIGURE 5.10: **(a)** Orbital occupation numbers versus time for repulsive interaction between the atoms. At time t_B the orbitals nearly become doubly degenerate meaning that both particles are in an equal superposition of being on the LHS and RHS of the trap simultaneously. **(b)** The behaviour of the Fisher information (solid) and entropy (dashed) are plotted versus time. The maximum F_Q reached is 3.883.

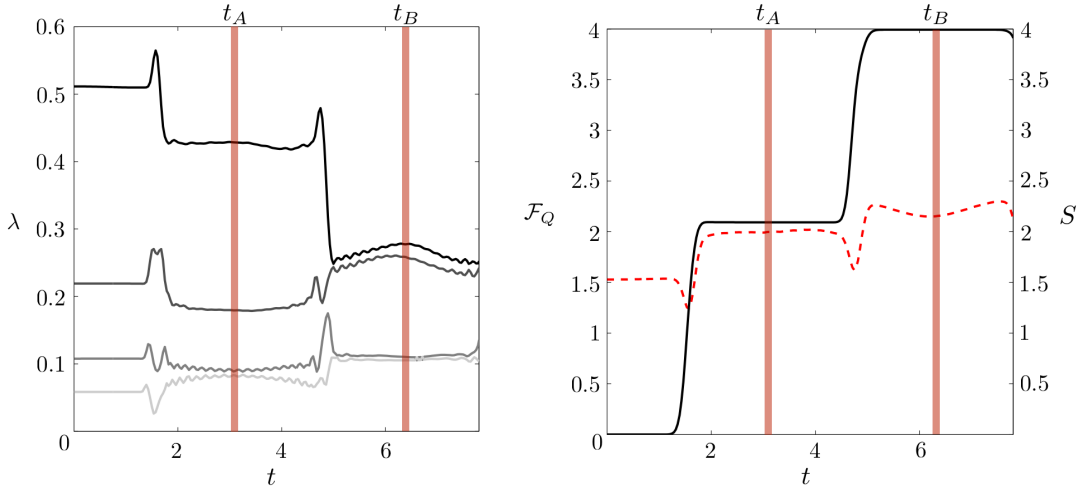


FIGURE 5.11: In the left panel the lowest four associated eigenvalues of the RSPDM are plotted. The right panel shows the quantum Fisher information (solid black line) and the von Neumann entropy (dashed red line) as a function of time.

After scattering with the barrier at t_s the evolution of the entanglement is not perfectly flat which can be attributed to the slight change in oscillation frequency Ω_δ caused by the inclusion of the barrier which becomes more pronounced after repeated collisions.

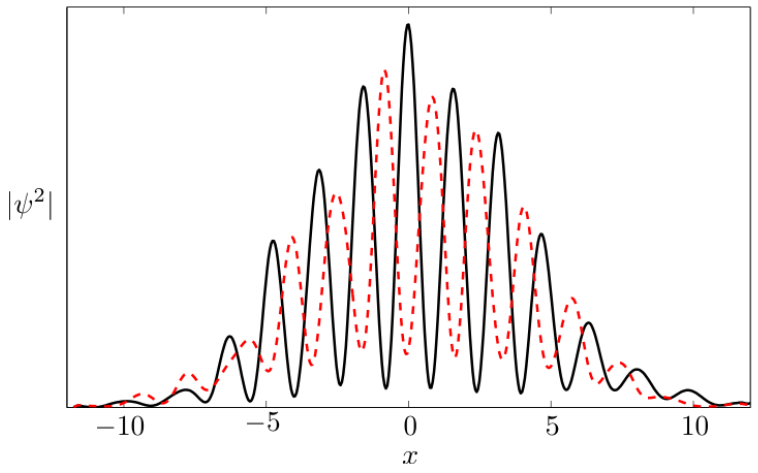


FIGURE 5.12: The beamsplitter is removed from the interferometer and the bi-localized system is allowed to recombine. Due to the coherent superposition an interference pattern is observed for $F_Q \approx 2$ (red dashed line) and $F_Q \approx 4$ (black solid line). The difference in fringe contrast is apparent.

5.4 Experimental Realization

Evidently the scheme presented here has an immediate experimental appeal as it is readily implementable. When a coherent bilocalised gas is created the detection of its state can be achieved by measuring the fringe visibility of the two particle interference [156, 169] and the interference fringe contrast is known to be maximal in the presence of a NOON state. A simulation of the interference fringes can be performed by numerically evolving the state in the basis of the free space solutions or by employing a scaling transformation [114]. This is shown in Fig. 5.12 where the solid line shows the pattern associated with the generated NOON state and the dashed line shows what one would obtain for a state at the shot noise limit, $F_Q = 2$. The difference in the fringe contrast is clearly visible.

5.5 Conclusions

We have presented a comprehensive analysis of a two particle interferometry procedure in a harmonic potential with a δ-barrier in the centre. We have shown that the inter-particle interaction has a large influence on the state created in such scattering experiments and therefore holds the potential to create metrologically useful states. By employing exact numerical diagonalization methods we were able to study the type of states dynamically created and we assessed the value of the states by studying both the entanglement content, via the von Neumann entropy, and the quantum Fisher information at the

classical turning points. The former is a useful metric for determining good states to use in metrology. Two scattering schemes were presented: after scattering from the barrier once attractively interacting particles were found to form a NOON state and for repulsively interacting particles the classical limit could not be exceeded. After a second scattering from the barrier, thus realizing a Michelson interferometer, NOON states could again be created and an interesting series of maxima and minima appeared due to an accumulated phase. When the interaction was repulsive this interferometer scheme was only successful in breaking the shot noise limit, and creating strongly non-local states with the possibility of creating NOON states, for a very restrictive range of parameters. This differs to the studies of [150] were it was shown strongly repulsive atoms could create a NOON state, as well as other useful states, in a stirred ring trap. As previously noted, although our work explicitly considers a δ-function barrier, the same results hold if one replaces it with a Gaussian barrier of finite width. In this instance the exact values of interaction strength and barrier height for optimal state generation will be slightly different to those found here, however the qualitative conclusions remain unaffected.

5.6 Outlook

The process of creating the NOON state in this system relied on imparting some initial momentum to the particles which allowed them to scatter from the barrier into a superposition state. This proceedure may be difficult to achieve in a realistic experimental setup, however one can consider a technologically slightly less complicated situation, in which both particles are initially located in an eigenstate of one half of a double well trap. Subsequent tunneling into the other well will depend on the interaction strength and the height of the barrier separating both wells. It would then be interesting to study what effect the interaction has on the tunnelling and if NOON states can possibly be created.

Chapter 6

Long distance entanglement in a linear ion chain

6.1 Introduction

The development of ultracold trapped ion systems has in recent decades led to experimental setups that allow one to carry out quantum mechanical experiments with high accuracy. Due to the intrinsic charge of the ions, systems with small numbers of particles form a crystalline structure at low energies, allowing for high fidelity laser addressing due to good spatial localisation. Ion chains are now a fore-runner for future quantum technologies and have also been proposed as the basis for quantum simulators. In fact, ion chains can be controlled in such a way, that their dynamics can be mapped onto other systems such as dipolar gases in optical lattices [6, 170], optomechanical arrays [171] and cavity arrays in circuit-QED [172].

Recently the idea of quantum reservoir engineering was introduced where, for properly designed couplings, interaction with an environment can be used to control a system and, for example, drive it into non-classical states [173–176]. These ideas have been successfuly applied to create entangled atomic ensembles [177], to perform quantum simulations with trapped ions [178] and they have been shown to provide a basis for protocols for quantum networks [179] and quantum metrology [180].

This work is the result of a collaboration during a three month research visit to the group of Prof. Morigi at the Universität des Saarlandes in Saarbrücken, Germany. I contributed to a project which was based on the knowledge of coupled oscillators and ion chains present in the group and an existing theoretical framework. I wrote and implemented code which modelled the entanglement dynamics in a linear chain of ions and this chapter represents an overview of the model and the results I contributed.

Phenomenological models describing two oscillators coupled to a common environment have shown that bath-induced entanglement generation can occur in cases where the bath is characterized by specifically designed spectra [181, 182]. An intrinsic assumption in these models is that the entangled systems are locally coupled to the same bath constituent within a microscopic description of the bath and subsequent works investigating the distance dependence of bath induced entanglement found that entanglement could only be created between neighbouring particles [183, 184]. These and similar papers have led to the belief that bath-induced entanglement generation between distant particles could not be achieved in continuous-variable systems, thereby restraining the scope of this approach. To circumvent this limitation, non-scalable strategies were developed that use finite-size effects to mediate long-distance entanglement (LDE) [185] between the end particles of one dimensional chains. Additionally, Prof. Morigi and coworkers showed that careful tuning of the systems' frequencies may lead to steady-state LDE in a chain of harmonic oscillators [186, 187] .

In this Chapter we will investigate the generation of long-distance entanglement in a physically realistic system of a linear chain of ions. Embedded in the ion chain are two defect ions of a different atomic species which are positioned symmetrically about the centre of the chain. We are interested in the entanglement generated in the continuous variable degrees of freedom of the impurities, specifically in the directions orthogonal to the axis of the ion chain. Our system of interest is therefore the transverse motion of the impurities which is subject to two environments: the transverse and axial modes of the ion chain. Due to the heavier mass of the impurities their transverse component will be only weakly coupled to the transverse motion of the ion chain and this degree of freedom will therefore only mediate a low amount of entanglement. However, for a large enough impurity mass their transverse modes can overlap with the band of axial vibrations of the rest of the ion chain and we show that by applying a standing laser field these two degrees of freedom can be coupled. The decisive ingredient for the predicted dynamics is the engineering of the defects-environment coupling, responsible for the establishment of a decoherence-free subspace. This is an area of the system's Hilbert space which is decoupled from the environment and therefore its evolution is completely unitary, allowing entanglement to be created and protected. This proposal is a completely new approach and the correlations arising from the described evolution do not a consequence of finite-size effects and are argued to occur even in the thermodynamic limit.

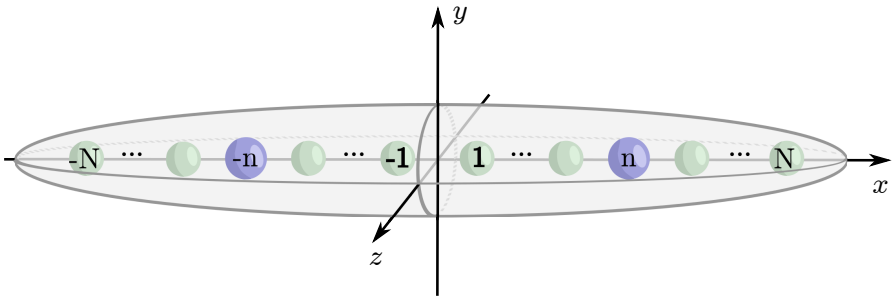


FIGURE 6.1: Sketch of the setup used for the long distance entanglement generation between the two impurities (blue) embedded in the ion chain (green). The trapping potential in the transverse directions is a lot tighter than in the axial direction ensuring a linear chain of ions.

6.2 Model

The model consists of a linear chain of $2N-2$ ions of mass m, and two impurity ions of mass M at positions $-n$ and n. The total number of ions in the chain is $\mathcal{N}=2N$ and they all have the same charge Q and interact via Coulomb repulsion. As the Coulomb force is long ranged we cannot assume only nearest neighbour coupling. The ions are confined harmonically in the axial and transverse directions with frequencies $\omega_{\parallel}$ and $\omega_{\perp}$ respectively and assuming that the transverse confinement is sufficiently large compared to the axial confinement the ions will form a linear chain along the x-axis.

The Hamiltonian of the ion chain can be written as

$$H_0=\sum_j \frac{\boldsymbol{p}_j^2}{2m_j}+U(\boldsymbol{r}_{-N},...,\boldsymbol{r}_N)\,, \tag{6.1}$$

where $\boldsymbol{r}_j=(x_j,y_j,z_j)$ and $\boldsymbol{p}_j$ are the positions and conjugate momenta. Here U accounts for the oscillators potential and the Coulomb repulsion between the ions,

$$U=\sum_j \frac{m_j}{2}\left[\omega_{\parallel}^2 x_j^2+\omega_{\perp,j}^2(y_j^2+z_j^2)\right]+\frac{Q^2}{8\pi\varepsilon_0}\sum_{j\neq i}\frac{1}{|\boldsymbol{r}_i-\boldsymbol{r}_j|}\,.$$

where $m_j=[m+(M-m)(\delta_{j,n}+\delta_{j,-n})]$ and the sums run from $-N$ to N. Throughout this chapter we will assume $\mu=M/m\approx 2.87$, corresponding to In^+ ions embedded in a Ca^+ chain [188]. Based on the standard configuration of a Paul trap [189], the axial trap frequency $\omega_{\parallel}$ depends on the static quadrupole potential and the transverse trap frequency $\omega_{\perp,j}^2=(\omega_j^r)^2-\frac{1}{2}\omega_{\parallel}^2$ on the radio frequency potential which creates the transverse confinement. The term ω_j^r depends on the frequency of the RF field and the ions mass, so at the positions of the impurities the transverse confinement will be different. The trap aspect ratio is given by $\epsilon=\sqrt{(\omega_{\perp}/\omega_{\parallel})^2+1/2}$. The classical

equilibrium positions of the ions along the axial direction can be computed by minimizing the Hamiltonian (6.2) which leads to the set of equations

$$\frac{\partial U}{\partial x_j} = m_j \omega_{\parallel}^2 x_j + \frac{Q^2}{4\pi\epsilon_0}\left(\sum_{i=-N}^{j-1}\frac{1}{(x_i-x_j)^2} - \sum_{i=j+1}^{N}\frac{1}{(x_i-x_j)^2}\right) = 0, j = -N, ..., N \ , \tag{6.2}$$

which can be re-written by scaling all lengths as $u_j l = -x_j + q_j$ with $l^3 = Q^2/(4\pi\epsilon_0 m\omega_{\parallel}^2)$. This gives

$$u_j - \sum_{i=-N}^{j-1}\frac{1}{(u_i-u_j)^2} - \sum_{i=j+1}^{N}\frac{1}{(u_i-u_j)^2} = 0 \ . \tag{6.3}$$

To avoid any finite size effects from the edges of the chain, we require the distance between the defects to be much smaller than the chain size $(x_{-n} - x_n) \ll 2N$ and their positions to be far away from the chain edges, $-N \ll x_{-n} < x_n \ll N$. For simplicity we also assume that the equilibrium positions of the ions are equally-spaced with interparticle distance $a = u_{j+1} - u_j$, which is dependent on the total number of ions $\mathcal{N}$ as $a = 2.29\mathcal{N}^{-0.596}$ [190]. Such a situation can be realised in optical lattices and also exists in the central region of long ion chains [191] and in anharmonic axial potentials [192]. The distance separating the impurities will be an integer multiple of this length such that $u_n - u_{-n} = da$, and in all further discussions involving the distance between the impurities the dimensionless parameter d will be used.

Introducing small oscillations around the equilibrium positions, q_j, and assuming these to be small enough to allow for linearisation of all forces, we find the Hamiltonian [193]

$$\mathcal{H} = \frac{m}{2}\sum_{\substack{j=-N\\ j\neq -n,n}}^{N}\dot{q}_j^2 + \frac{M}{2}\dot{q}_{-n}^2 + \frac{M}{2}\dot{q}_n^2 + \frac{1}{2}\sum_{i,j=-N}^{N}\left.\frac{\partial^2 U_x}{\partial x_i \partial x_j}\right|_{\{q_i\}=0} q_i q_j \ , \tag{6.4}$$

$$= \frac{m}{2}\sum_{\substack{j=-N\\ j\neq -n,n}}^{N}\dot{q}_j^2 + \frac{M}{2}\dot{q}_{-n}^2 + \frac{M}{2}\dot{q}_n^2 + \frac{1}{2}Q\sum_{i,j=-N}^{N}\left.A'_{ij}\right|_{\{q_i\}=0} q_i q_j \ , \tag{6.5}$$

where

$$A'_{ij} = \begin{cases} 1 + 2\sum\limits_{\substack{k=-N\\ k\neq i}}^{N}\frac{1}{|u_i-u_k|^3}, & j = i \ , \\ -2\frac{1}{|u_i-u_j|^3}, & j \neq i \ . \end{cases} \tag{6.6}$$

In the transverse direction the resulting Hamiltonian is

$$\mathcal{H} = \frac{m}{2}\sum_{\substack{j=-N\\ j\neq -n,n}}^{N} \dot{z}_j^2 + \frac{M}{2}\dot{z}_{-n}^2 + \frac{M}{2}\dot{z}_n^2 + \frac{1}{2}Q\sum_{i,j=-N}^{N} B_{ij}^{'}\Big|_{\{z_i\}=0} z_i z_j \ , \tag{6.7}$$

where B' describes $\frac{\partial^2 U_z}{\partial z_i \partial z_j}\Big|_{\{z_i\}=0}$

$$B'_{ij} = \begin{cases} \epsilon^2 - \frac{1}{2} - \sum\limits_{\substack{k=-N\\ k\neq i}}^{N} \frac{1}{|u_i-u_k|^3}, & j = i, j \neq -n \neq n \ , \\ \\ \frac{\epsilon^2}{\mu} - \frac{1}{2} - \sum\limits_{\substack{k=-N\\ k\neq i}}^{N} \frac{1}{|u_i-u_k|^3}, & j = i = -n \ \text{ or } j = i = n \ , \\ \\ \frac{1}{|u_i-u_j|^3}, & j \neq i \ . \end{cases} \tag{6.8}$$

The above Hamiltonian also holds for the y-direction, however from this point on we will only be concerned with the transverse motion of the ions in the z-direction without loss of generality. At the positions of the impurities these matrix elements are modified by the mass ratio μ and for the diagonal elements, $i = j$, at $\{-n, -n\}$ or $\{n, n\}$ we get

$$A_{ii} = A'_{ii}/\mu \, . \tag{6.9}$$

For the off diagonal terms, $i \neq j$ the following holds for $\{-n, j \neq n\}$, $\{n, j \neq -n\}$, $\{i \neq n, -n\}$ and $\{i \neq -n, n\}$

$$A_{ij} = A'_{ij}/\sqrt{\mu} \, . \tag{6.10}$$

And finally for the cross terms of both impurities $\{-n, n\}$ and $\{n, -n\}$ we have

$$A_{i,-i} = A'_{i,-i}/\mu \, . \tag{6.11}$$

The separate dynamics described by the above Hamiltonians allow us to study, independently, axial and transverse spectra by diagonalizing A and B respectively. Fig.6.2 shows the mode spectra for a distance $d = 17$ between the defects. The two degenerate normal mode frequencies of the transverse modes are separate from the continuum. These frequencies correspond to normal modes localized around the position of the two defects and appear due to the mass dependence of the transverse, radio-frequency potential. By varying the mass ratio $\mu = M/m$ or the trap aspect ratio ϵ, these localized frequencies can be tuned. For large enough separations from the continuum part of the transverse spectrum, the dynamics of these two modes decouple from the rest of the

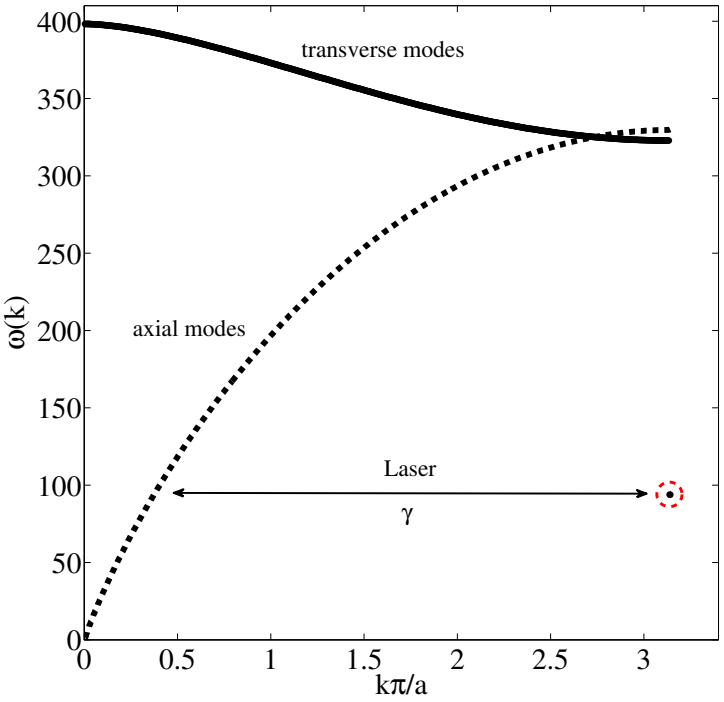


FIGURE 6.2: Transverse modes (solid line) and axial modes (dashed line) of $\mathcal{N} = 800$ ions with impurities separated by $d = 17$. The discrete wavevector is defined as $k_j = j\pi/(a(\mathcal{N}+1))$ where $j \in \{1, ..., \mathcal{N}\}$. Due to the heavier mass of the impurities their corresponding transverse modes (circled) are decoupled from the transverse band and now lie deep in the axial band.

transverse chain. In this situation when these frequencies are tuned to coincide with the axial band, we can use a standing-wave laser field to couple axial and transverse motions. Thermalization of the localized modes would then be expected due to their interaction with the axial bath.

6.2.1 Initial state preparation

At this point it is useful to introduce dimensionless coordinates such that all positions are scaled in terms of the size of the ground state $x_0 = \sqrt{\hbar/m\omega_{\|}}$,

$$\bar{x}_i = \frac{x_i}{x_0}, \tag{6.12}$$

$$\bar{z}_i = \frac{z_i}{x_0}, \tag{6.13}$$

$$\bar{p}_i = \frac{p_i}{p_0}, \tag{6.14}$$

and $p_0 = \hbar/x_0$. Our goal now will be to entangle the two defects' transverse modes through their interaction with the chain reservoir. With the defects' transverse modes decoupled from both the axial and transverse bath, the initial state of the bath can be prepared by laser cooling it to a thermal state at temperature T,

$$\rho_{th}(0) = \exp(-H_R/T)/Z \; , \tag{6.15}$$

where H_R is the reservoir Hamiltonian and $Z = \mathrm{Tr}[\exp(-H_R/T)]$ it's partition function. The initial covariance matrix of the thermal state at $t = 0$ can be written as

$$\begin{aligned}
\sigma_{xx}(0) &= \langle \bar{x} \otimes \bar{x}^T \rangle - \langle \bar{x} \rangle \otimes \langle \bar{x} \rangle^T \; , & (6.16)\\
\sigma_{pp}(0) &= \langle \bar{p} \otimes \bar{p}^T \rangle - \langle \bar{p} \rangle \otimes \langle \bar{p} \rangle^T \; , & (6.17)\\
\sigma_{xp}(0) &= \frac{1}{2}\langle \bar{x} \otimes \bar{p}^T + \bar{p} \otimes \bar{x}^T \rangle - \langle \bar{x} \rangle \otimes \langle \bar{p} \rangle^T \; , & (6.18)
\end{aligned}$$

with the explicit expressions given as

$$\begin{aligned}
\sigma_{xx}(0) &= \frac{1}{2}(\bar{V})^{-\frac{1}{2}} \coth\left(\frac{\bar{\beta}}{2}(\bar{V})^{\frac{1}{2}}\right) \; , & (6.19)\\
\sigma_{pp}(0) &= \frac{1}{2}(\bar{V})^{\frac{1}{2}} \coth\left(\frac{\bar{\beta}}{2}(\bar{V})^{\frac{1}{2}}\right) \; , & (6.20)
\end{aligned}$$

and $\sigma_{xp}(0) = 0$. The potential matrix $\bar{V}$ is constructed from the matrices A and B such that

$$\bar{V} = \frac{1}{m\omega_{\|}^2} \begin{pmatrix} A & 0 \\ 0 & B \end{pmatrix} \; , \tag{6.21}$$

and $\bar{\beta} = \hbar\omega_{\|}/(k_B T)$, where T is the temperature of the bath, and k_B is Boltzmann's constant. We have assumed that the first moments $\langle \bar{x} \rangle = 0$ and $\langle \bar{p} \rangle = 0$ vanish for the initial thermal state.

The covariance matrix elements of the defects are given explicitly by

$$\begin{aligned}
\Sigma_{11} &= \langle Z^2 \rangle - \langle Z \rangle^2 \; , & (6.22)\\
\Sigma_{22} &= \langle P^2 \rangle - \langle P \rangle^2 \; , & (6.23)\\
\Sigma_{12} &= \frac{1}{2}\langle ZP + PZ \rangle - \langle Z \rangle \langle P \rangle \; . & (6.24)
\end{aligned}$$

Again we assume initially that the first moments $\langle Z \rangle$ and $\langle P \rangle$ are zero. The defects transverse modes are prepared in identical, separable, pure squeezed states, $\rho_{-n}(s)$ and $\rho_n(s)$, with squeezing parameter s. A state is squeezed if its uncertainty in position and momentum are unequal thus forming an ellipse in phase space. The elements of the

covariance matrix for the impurities are [194]

$$\Sigma_{11}(s) = \frac{x_0^2}{2} e^{-2s} \tag{6.25}$$

$$\Sigma_{22}(s) = \frac{p_0^2}{2} e^{2s} \tag{6.26}$$

$$\Sigma_{12}(s) = 0\,. \tag{6.27}$$

The total initial state of the system is then,

$$\rho(0) = \rho_n(0) \otimes \rho_{-n}(0) \otimes \rho_{th}(0). \tag{6.28}$$

The defects' state is Gaussian and is, therefore, fully characterized by their first moments and covariance matrix [195]. The entanglement between the defects can thus be quantified by the logarithmic negativity as

$$E_N = \max\{0, -\ln(2\tilde{\nu}_-)\}\,, \tag{6.29}$$

where $\tilde{\nu}_-$ is the smallest symplectic eigenvalue of the partial transpose of the covariance matrix Σ [196, 197].

6.2.2 Coupling of transverse and axial directions

At time $t = 0$, with the inital state Eq. (6.28) prepared, a standing-wave laser field on the $x-z$ plane is applied to couple the transverse modes of each defect to the axial mode spectrum. The laser is set to off-resonantly address an optical transition of the defect ions, whose equilibrium positions lay at the antinodes of the standing-wave. The laser induced coupling between the ion's internal states and its motional states is sufficiently small so that transitions that change the motional state by more than one quanta are negligible, which corresponds to the so called Lamb-Dicke regime [198]. The dynamics of the chain is then given by $H = H_0 + H_I(t)$, where

$$H_I(t) = \frac{\bar{\gamma}(t)}{2} \left[(\bar{z}_{-n} - \bar{x}_{-n})^2 + (\bar{z}_n - \bar{x}_n)^2\right], \tag{6.30}$$

with $\bar{\gamma}(t) = \frac{\gamma}{m\omega_\parallel^2}\,\Theta(t)$ being an effective coupling strength and $\Theta(t)$ the Heaviside function. The potential energy of the impurities will be modified by the laser coupling so the matrix elements of the impurities in Eq. (6.6) and Eq. (6.8) must be altered by the addition of γ such that $A^{\gamma}_{i,i} = A'_{i,i} + \gamma$ for $i \in \{n, -n\}$ and similarly for $B'_{i,i}$. Due to this local coupling, an excitation in the defects' transverse modes will lead to an excitation in their axial direction which, coupled to the rest of the axial chain, generates a phononic

excitation in the chain. The coupling of the laser must also be included in the off diagonal terms at the positions of the impurities in the matrix $\bar{V}$ thereby coupling the axial and transverse potential matrices A and B. We then label this amended potential matrix under the influence of the laser as $\bar{V}^{\gamma}$.

6.2.3 Dynamics

The time evolution of the ion chain can now be described as a system of coupled oscillators [199]. No special assumptions are made about the interactions of the oscillators and we only require that the potential matrix has no negative eigenvalues. The canonical equations of motion can be written as

$$\dot{\mathbf{x}} = \boldsymbol{p} \;\text{ and }\; \dot{\boldsymbol{p}} = -\bar{V}^{\gamma}\mathbf{x}\,, \tag{6.31}$$

and their solutions will have the form

$$\begin{pmatrix} \mathbf{x}(t) \\ \boldsymbol{p}(t) \end{pmatrix} = \begin{pmatrix} W\cos(\Omega t)W' & W\Omega^{-1}\sin(\Omega t)W' \\ W\Omega\sin(\Omega t)W' & W\cos(\Omega t)W' \end{pmatrix} \begin{pmatrix} \mathbf{x}(0) \\ \boldsymbol{p}(0) \end{pmatrix}. \tag{6.32}$$

Here W is a matrix of the eigenvectors and $\Omega = \mathrm{diag}(\bar{\omega}_1, \ldots, \bar{\omega}_{\mathcal{N}})$ is a matrix of the eigenfrequencies of the potential matrix $\bar{V}^{\gamma}$. We label the block matrix as $\mathcal{T}(t)$ and apply it to the initial covarinace matrix at $\mathcal{V}(t=0)$ such that $\mathcal{V}(t) = \mathcal{T}(t)\mathcal{V}(0)\mathcal{T}^{T}(t)$. The initial covariance matrix is also in block form and can be written as

$$\mathcal{V}(0) = \begin{pmatrix} \sigma_{xx} & 0 \\ 0 & \sigma_{pp} \end{pmatrix}. \tag{6.33}$$

6.2.4 Spectral Density

Since the defects are placed symmetrically with respect to the trap centre, the Hamiltonian H is invariant under the exchange of the j-th and the $(2N-j+1)$-th ion ($j \in \{1, \cdots, 2N\}$) and a description in terms of centre of mass (COM) and relative coordinates for pairs of ions is well suited.

The centre of mass and relative coordinate of the impurities in the transverse direction is given by

$$\bar{Z}_{\pm} = \frac{\bar{z}_{-n} \pm \bar{z}_{n}}{\sqrt{2}}, \tag{6.34}$$

and similarly the centre of mass and relative coordinates of the bath particles in the axial direction are

$$\bar{x}^{i}_{\pm} = \frac{\bar{x}_{i} \pm \bar{x}_{-i}}{\sqrt{2}} \tag{6.35}$$

For brevity both of these can be written in matrix form

$$\mathbf{x}_\pm = S\mathbf{x} \quad \text{with} \quad S = \frac{1}{\sqrt{2}} \begin{pmatrix} \mathbb{1} & \mathbb{1} \\ \mathbb{1} & -\mathbb{1} \end{pmatrix} = S^{-1}\,, \tag{6.36}$$

and an analogous transformation for the momentum operator vectors yields $\boldsymbol{p}_\pm = S\boldsymbol{p}$.

Accordingly we obtain the following transformation of the potential part of the bath Hamiltonian

$$\mathbf{x}^T \bar{A}^{(\gamma)} \mathbf{x} = \mathbf{x}_\pm^T (S^T \bar{A}^{(\gamma)} S) \mathbf{x}_\pm = \mathbf{x}_\pm^T \bar{A}_\pm^{(\gamma)} \mathbf{x}_\pm\,, \tag{6.37}$$

where $\bar{A}^{(\gamma)}$ is the potential matrix in the axial direction under the influence of the coupling laser. If the COM and relative coordinates are decoupled, we expect to find the following block structure of the transformed potential matrix

$$\bar{A}_\pm^{(\gamma)} = S^T \bar{A}^{(\gamma)} S = \begin{pmatrix} \bar{A}_+^{(\gamma)} & 0 \\ 0 & \bar{A}_-^{(\gamma)} \end{pmatrix}. \tag{6.38}$$

The full Hamiltonian of the transverse motions of the impurities and their coupling to the bath is then given by

$$H = \frac{1}{2}(\bar{p_z}_{-n}^2 + \bar{p_z}_n^2 + \bar{z}_{-n}^2 + \bar{z}_n^2) + \frac{\mathbf{p}^2}{2m} + \frac{1}{2}\mathbf{x}^T \bar{A}^{(\gamma)} \mathbf{x} - \frac{\bar{\gamma}}{2}(\bar{z}_{-n}\bar{x}_{-n} + \bar{z}_n \bar{x}_n)\,, \tag{6.39}$$

and inserting the new coordinates and using $S_\pm \mathbf{x}_\pm = \mathbf{x}$, we can write it in COM and relative coordinates as

$$H = \frac{1}{2}(\bar{P}_-^2 + \bar{P}_+^2 + \bar{Z}_-^2 + \bar{Z}_+^2) + \frac{\mathbf{p}_-^2}{2m} + \frac{\mathbf{p}_+^2}{2m} + \frac{1}{2}(\mathbf{x}_\pm^T \bar{A}_\pm^{(\gamma)} \mathbf{x}_\pm) - \frac{\bar{\gamma}}{2}(\bar{Z}_+ \bar{x}_+^b + \bar{Z}_- \bar{x}_-^b)\,, \tag{6.40}$$

where $b = (d+1)/2$ is the position of the single impurity in the COM and relative chain. In these coordinates the action of the bath on the dynamics of the defect's collective variables can be explored through the spectral density of the environment. The spectral density informs one about the frequency weighted coupling of the COM and relative coordinates of the impurities to the environment and by diagonalizing the potential matrix $\bar{A}_\pm^{(\gamma)}$ such that $O_\pm^T \bar{A}_\pm^{(\gamma)} O_\pm = \mathrm{diag}((\bar{\omega}_1^\pm)^2, \ldots, (\bar{\omega}_N^\pm)^2)$ the eigenvalues $\bar{\omega}^\pm$ can be used to calculate the spectral density as

$$\bar{J}_\pm(\bar{\omega}) = \frac{\pi}{2} \sum_{j=1}^{N} \frac{(\bar{\gamma}_j^\pm)^2}{\bar{\omega}_j^\pm} \delta(\bar{\omega} - \bar{\omega}_j^\pm), \tag{6.41}$$

where $\bar{\gamma}^\pm = O_\pm^T \bar{\gamma}$. In this case one can ensure that either the COM or relative motion is decoupled from the environment by suitably tuning ϵ from Eq. (6.8) to coincide with

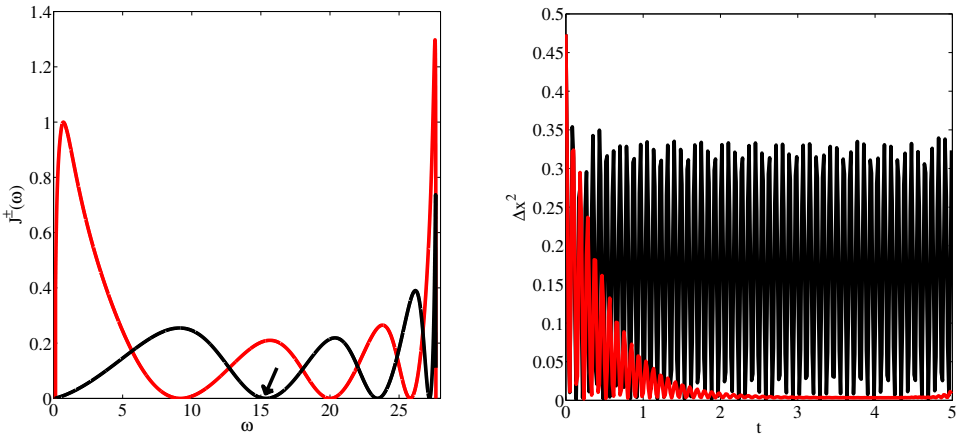


FIGURE 6.3: Left panel: The spectral density for 800 ions and impurities separated by $d = 7$ with laser coupling $\bar{\gamma} = 0.2$ is plotted for the COM (red line) and relative (black line) coordinates with time in units of $\omega_{\parallel}^{-1}$. The impurities' transverse modes are tuned to coincide with the first node of the relative spectral density $J^{-}(\omega)$ indicated by the arrow. Right Panel: Second moments of the impurities position versus time for $d = 7$ with the relative coordinate decoupled (black line) and the COM coupled to the environment (red line). The COM motion of the impurity quickly decays as it is strongly coupled to the environment while the decoupled relative motion oscillates undamped.

a node in the spectral density, $\bar{\omega}_0$, such that

$$\epsilon = \sqrt{\mu \left(\mu \bar{\omega}_0^2 + \bar{\gamma} + \frac{1}{2} + \sum_{\substack{k=-N \\ k \neq i}}^{N} \frac{1}{|u_i - u_k|^3} \right)}. \tag{6.42}$$

Conversely this will result in the other motion to be coupled to the environment and undergo thermalization. This can be observed in the second moments of the impurity ions after being coupled to the environment. In the left panel of Fig. 6.3 the spectral density for two impurites separated by $d = 7$ is plotted. There are three nodes in the spectral density for each motion, and without loss of generality the first node of the relative motion is chosen. The trap aspect ratio is then tuned so that the transverse modes of the impurities coincide with this chosen frequency. In this case the relative motion of the impurities is decoupled from the bath and its motion does not decay over time. This is shown in the right-hand side panel of Fig. 6.3 where the second moments of the impurities are plotted. The black line is the relative motion, and the red line is the COM motion which is coupled to the enviroment and thus thermalizes. In this regime part of the initial squeezing is stored in the relative motion, whilst the long distance entanglement generation is mediated by the COM motion until the steady state is reached at the thermalization point.

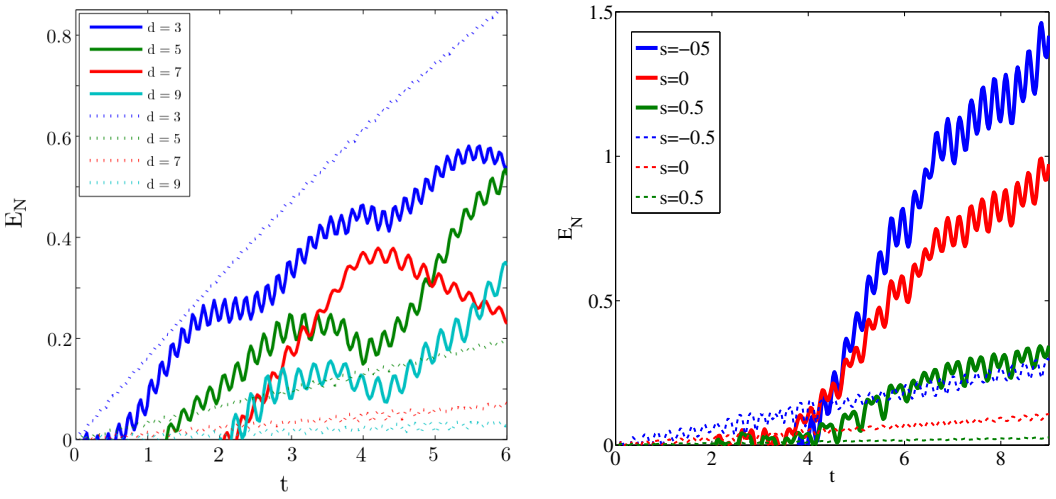


FIGURE 6.4: Left panel: Entanglement versus time for initial squeezing $s = -1$ and $T \approx 0$ for different separations between the impurities with time in units of $\omega_{\|}^{-1}$. The solid lines are the situation where the coupling laser is used to create the bath induced entanglement, $\bar{\gamma} = 0.2$, the dashed lines are the situation where no coupling laser is used, ie. $\bar{\gamma} = 0$. Right panel: Impurities are separated by $d = 7$ for squeezings of $s = -0.5, 0, 0.5$ at a temperature of $T = 5$mK. For low finite temperatures the engineered environment (solid lines) far exceeds the situation without any laser coupling (dashed line).

6.3 Entanglement generation in a short ion chain

The current state of the art in ion trapping two different species is for chain lengths of about 10 ions, and for single species chains the lengths can be longer ≈ 50 [188, 200]. The rather small size of these chains means that finite size effects due to reflections from the end of the chain will destroy the decoherence free subspace created in our system, and therefore an entanglement steady state will not be achieved. However the effect of the coupling laser can significantly enhance the generation of entanglement between the impurities on very short timescales. In the following a chain of length $N = 50$ ions is simulated with impurities symmetrically placed around the centre of the ion chain at different distances from each other. In the left panel of Fig. 6.4 the negativity as a function of time is plotted for various separations of the impurities. Time is scaled in terms of the inverse axial trap frequency $\omega_{\|}^{-1}$. The solid lines represent the effect of the environment engineering through the coupling laser which has the value $\bar{\gamma} = 0.2$ and the dashed lines represent the case for no coupling laser, $\bar{\gamma} = 0$. One can see that for $d = 3$ the coupling laser did not produce any increase in entanglement compared to the system without the laser interaction. However at larger distances the effect of the laser becomes more apparent and enhanced entanglement generation mediated through the bath becomes visible. In the right-hand side panel of Fig. 6.4 the case of

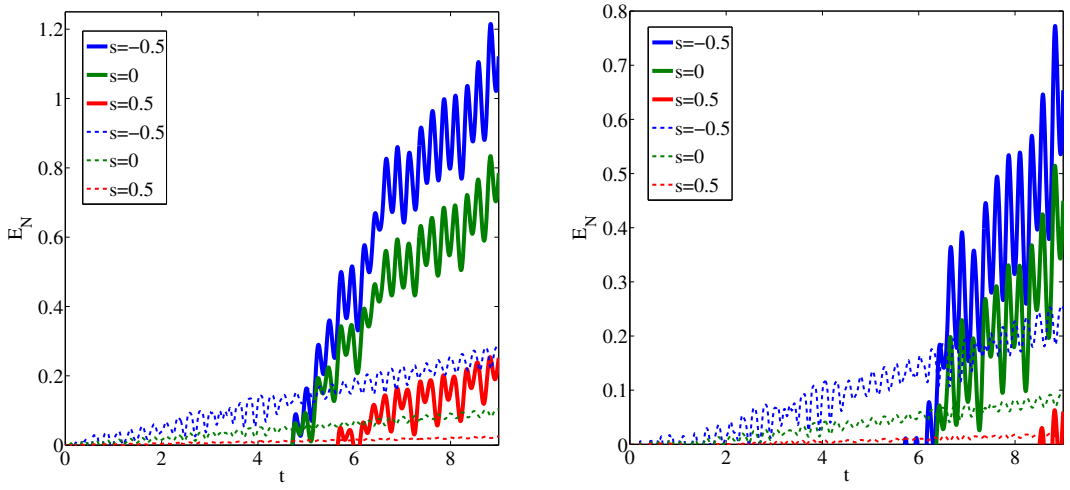


FIGURE 6.5: Entanglement versus time at $d = 7$ and for $\bar{\gamma} = 0.2$ for squeezings of $s = -0.5, 0, 0.5$ at temperatures of **(a)** 10mK **(b)** and 20mK. The dashed lines are the situation where no coupling laser is used, ie. $\bar{\gamma} = 0$.

$d = 7$ is explored for different strengths of the initial squeezing $s = -0.5, 0$ and 0.5 at a finite temperature $T = 5$mK. One can see that there is a significant increase in the entanglement generated for finite values of s, which makes the squeezing of the impurities an important entanglement resource in this scheme. It is also interesting to note that entanglement is even created for an initial squeezing of $s = 0$ which is contrary to the case if there were no ion chain between the defects.

In realistic experimental setups the temperatures reached by the ions can be higher and this must be taken into account when discussing this system. In Fig. 6.5 the effect of higher temperatures on the entanglement is investigated at $T = 10$mK and $T = 20$mK. Even though finite temperatures diminish the amount of entanglement generated the enhancement due to the coupling laser can still be observed.

6.4 Entanglement generation in a long ion chain

To investigate the creation of long distance entanglement and an entangled steady state the size of the ion chain must be quite large. This is because finite size effects occur caused by reflections from the edge of the ion chain. To negate these effects and to ensure the steady state is reached the size of the ion chain used in the following simulations is $\mathcal{N} = 800$ and $\bar{\gamma} = 0.25$. However the average entanglement reached during the steady state can be shown to be independent of the exact number of ions in the environment and this is shown in Fig. 6.6 where we plot the negativity for $\mathcal{N} = 600$ (red line),

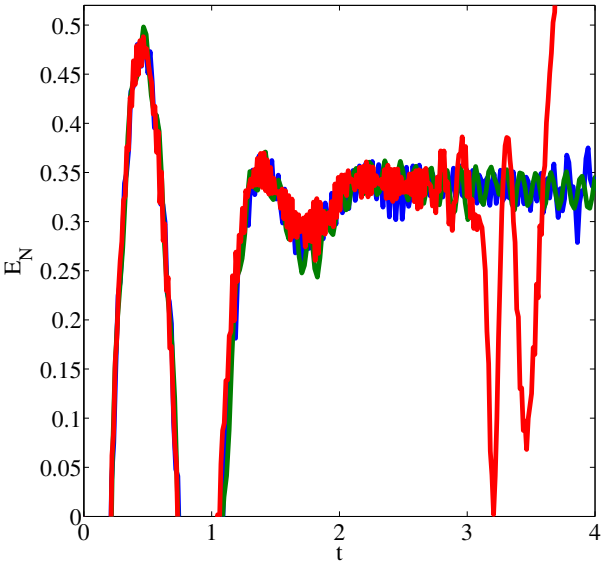


FIGURE 6.6: The negativity versus time is plotted for $\mathcal{N} = 600$ (red line), 800 (blue line) and 1000 (green line). For each curve the time is in units of $\omega_{\parallel}(\mathcal{N})^{-1}$ where $\omega_{\parallel}(\mathcal{N}) = \omega_{\rm ref}\sqrt{\log\mathcal{N}}/\mathcal{N}$ and the reference frequency is $\omega_{\rm ref} = 2\pi \times 659.6$ kHz. As can be seen the evolution of the entanglement is irrespective of chain size up until the trap revival which cause the finite size effect which is present for $\mathcal{N} = 600$ at times $t > 3$.

$\mathcal{N} = 800$ (blue line) and $\mathcal{N} = 1000$ (green line). The entanglement can be seen to reach a steady state for $t > 2$ regardless of the number of ions in the bath, and it oscillates about a (quasi) stationary state. For $t > 3$ the finite size effect can again be observed for $\mathcal{N} = 600$ as large oscillations in the negativity. This is due to reflections from the end of the ion chain which shortens the lifetime of the steady state but can be delayed by increasing the size of the chain.

In the left-hand side panel of Fig. 6.7 the negativity versus time is plotted for $d = 11$ (blue), 13 (green) and 15 (red). In this case the relative motion is decoupled and the second node of the spectral density is chosen. An entangled steady state is reached in all cases, however at different times dependent on the value of d. The mean value of the steady state averaged over the time in which it regularly oscillates also changes with d and this is shown in the right-hand side panel of Fig. 6.7 for the 2^{nd} to the 6^{th} node. There is no steady state reached for the first node and optimal entanglement can be achieved by tuning the frequency of the impurity so that it matches the frequency of a node which maximises the amount of entanglement generated.

The results for the decoupled COM motion is qualitatively equivalent to the case discussed above for the decoupled relative motion and are shown in Fig. 6.8. The frequencies of the nodes of the spectral density differ and this results in a different range of accessible nodes, 1^{st} to 5^{th}, to reach the steady state.

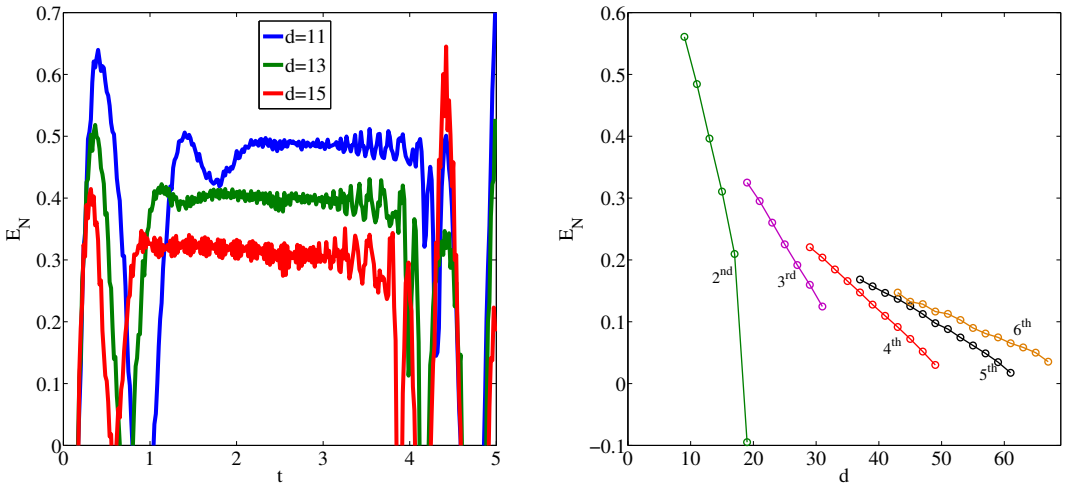


FIGURE 6.7: Entanglement between the two defects in a bath of $\mathcal{N} = 800$ ions for an initial squeezing of $s = 0.5$ and $\bar{\gamma} = 0.25$ at temperature $T \approx 0$. Left panel: Negativity versus time for $d = 11$ (blue), 13 (green) and 15 (red). The second node of the relative spectral density has been chosen in each case. Right Panel: The mean entanglement of the steady state is plotted as a function of d for different nodes of the relative coordinate's spectral density. The nodes are labelled from the 2^{nd} to the 6^{th}. No steady state is reached for the first node.

6.5 Conclusions

Bath mediated entanglement was investigated for the system of two impurity ions embedded in a linear ion chain. The transverse degrees of freedom of the impurities were coupled to the axial environment by a laser which stimulated the creation of entanglement. By choosing the correct trap aspect ratio the environment could be engineered to allow the existence of a decoherence free subspace by which entanglement between the impurities could reach a steady state. It was shown that for short ion chains the steady state was not reached but entanglement creation was enhanced by the coupling laser. This is promising for recent experiments which can create two-species ion chains using a small number of ions, $\mathcal{N} < 20$. Also the system is robust against environmental effects such as finite temperature.

The appearance of the entangled steady state could only be achieved for long ion chains $\mathcal{N} > 500$ due to finite size effects caused by the ends of the chain. However it was shown that the number of ions used in the chain does not change the mean value of the steady state.

Contrary to previous works which report that bath mediated generation of long distance entanglement could not be achieved in continuous-variable systems [183, 184], we have

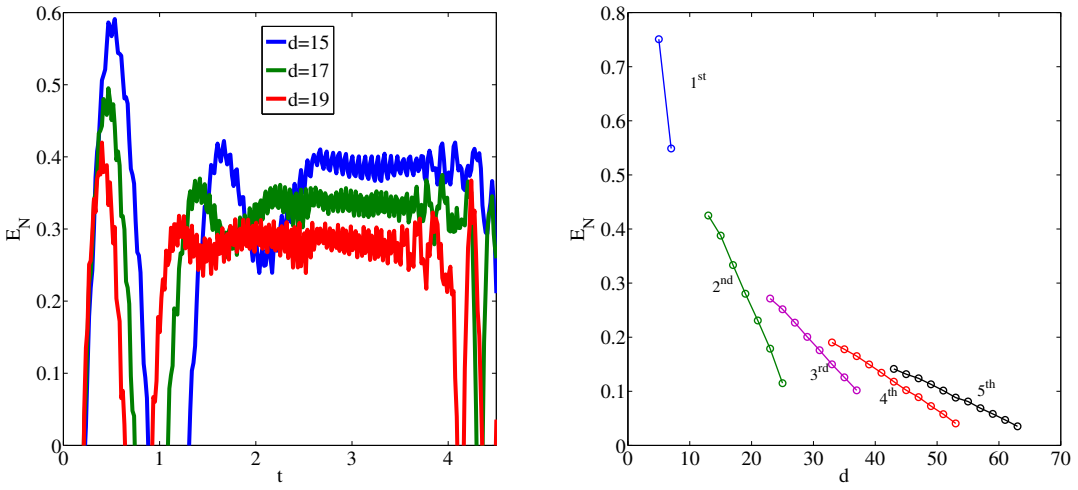


FIGURE 6.8: Entanglement of the two defects in a bath of $\mathcal{N} = 800$ ions for an initial squeezing of $s = 0.5$ and $\bar{\gamma} = 0.25$ at temperature $T \approx 0$. Left panel: Negativity versus time for $d = 15$ (blue), 17 (green) and 19 (red). The second node of the COM spectral density has been chosen in each case. Right Panel: The mean entanglement of the steady state is plotted as a function of d for different nodes of the COM coordinate's spectral density. The nodes are labelled from the 1^{st} to the 5^{th}.

shown that this is not the case and that suitable environment engineering can promote robust entanglement creation.

6.6 Outlook

It would be interesting to study the phase transition in the ion chain as it goes from linear to zig-zag configuration. This suddenly occurs as the trap aspect ratio is decreased past some critical point. The location of this critical point could be inferred through the entanglement or quantum discord between two ions of the chain.

Chapter 7

Conclusions and Outlook

In this thesis I have described varied topics in low dimensional ultracold atomic systems. In Chapter 2 I discussed in detail a problem of two bosons trapped in individual harmonic traps. In Chapter 3 the Tonks-Girardeau gas was introduced and the specific case of the gas under the influence of an impurity potential was solved. In Chapter 4 a scheme was presented to probe a Fermi gas with an impurity qubit and thereby observe the orthogonality catastrophe. In Chapter 5 the creation of coherent superpositions of many-body states was undertaken with an emphasis on creating useful states for interferometry experiments. Finally in Chapter 6 I introduced some work which I have contributed to concerning the problem of generating long distance entanglement in ion chains. In these works special emphasis was placed on their experimental realisation in modern laboratories and their tunability through the adjustable parameters of their respective Hamiltonians, something which is desirable for quantum engineering. For completeness, I briefly summarise those topics and the relevant results here.

7.1 Entanglement and non-locality between two interacting atoms

The correlations of two interacting atoms was investigated where the atoms are trapped in individual harmonic traps which are separated by a distance d. In this case the form of the Hamiltonian permitted the separation of the problem into the centre of mass and relative coordinate systems. The centre of mass Hamiltonian was that of a single atom in a harmonic potential and could be readily solved analytically. The relative coordinate system took the form of a single atom in a harmonic trap which was punctuated by a δ-function potential at a distance d from the centre of the trap. The height of the δ-function is related to the strength of the interaction between the two particles. This Hamiltonian

was shown to be exactly analytically solvable through the use of parabolic cylinder functions. The solutions of this system contained an interesting physical effect which was the existence of trap induced shape resonances, which appear as avoided crossings in the energy spectrum at specific distances between the traps. At these points the von Neumann entropy was shown to exhibit sudden increases in entanglement even for large distances between the individual traps. Consequently the non-local behaviour of the continuous variable state was calculated using the two-mode Wigner distribution. The negative volume of the Wigner function indicated the non-classicality of the state which was subsequently quantified by the non-locality as calculated by the CHSH inequality. The inequality was violated for finite trap separations, however the length scale of the observed correlations were far less than observed in the von Neumann entropy. This perceived fragility of the non-locality led to an investigation of a suitable entanglement witness under the influence of a dissipative process, and it was found that using modern detection techniques the non-classical nature of the system can be observed. Finally at finite temperature the non-classicality of the state was found to be more robust for the cases of lower interaction strengths and consequently lower non-locality. This was explained by examining the energy difference between the ground and first excited state of the system, which is larger for weakly interacting atoms and smaller for strong interactions. As the gap between these energy levels decreases the probability for the atoms to be excited to higher modes is increased, which leads to larger temperature sensitivity. This work has been published in New Journal of Physics **13** (2), 023016 (2011).

Further studies on non-classical correlations in two particle systems in higher dimensions would be fruitful, as the relation between the scattering length and interaction strength changes and trap induced shape resonances are still present. Also, the effect of angular momentum on the bipartite correlations would be an interesting extension to this study. By using an asymmetric three dimensional trap in this case one can study the effect that reducing dimensionality has on the state.

7.2 Coherence and dynamics of a Tonks-Girardeau gas

The Tonks-Girardeau gas was introduced and solved in an asymmetrically split harmonic oscillator. The trap was split by a δ-function of variable height that could be positioned at any point along the trap axis. The effect of the position of the δ-function on the total energy of the gas was investigated and was found to contain lobes at the locations of the hard-core bosons. This crystaline structure was also evident in the occupation of ground state orbital and height of the central peak of the momentum distribution. Both

of these quantities were argued to be an indication of the coherence of the gas, which was justified by carrying out a time of flight calculation of the interference fringes. The dynamics of the gas was also examined after sudden removal of the δ-function potential, which led to the disappearance and revival of the impurity's density dip. This is the matter wave analogy of the Talbot effect in optics by which the initial density of the gas is repeated at regular intervals. This work has been published in New Journal of Physics **12** (9), 093041 (2010).

Recent experiments have successfully embedded ions in ultracold gases and it would be worthwhile to investigate the effect of the ion's micromotion on the surrounding gas [118, 120]. Significant progress has been made to theoretically describe the effect of micromotion of a trapped ion on a neutral atom [121] and a logical extension would be to study the many-body response of the TG gas to such an interaction.

7.3 The orthogonality catastrophe in a Fermi gas

The effect of an impurity on the overlap between two non-interacting Fermi gases was thoroughly examined in the harmonic trap. The results showed signs of the orthogonality catastrophe (OC) in which the overlap between two many-body states becomes orthogonal as the size of the system was increased. It was found that the strength of the scattering potential set a limit on the range of the OC, with respect to the number of particles in the state. It was then proposed that by using an impurity qubit the irreversibility of a quenched Fermi gas could be calculated using the Loschmidt echo. This time dependent process is analogous to X-ray absorption experiments in solid state physics, in which one observes the OC as a power law broadening of the single particle spectral function. To witness the OC in this case the experimental procedure of Ramsey interferometry was considered, by which the probability of the impurity qubit to be in its ground state can be measured as a function of time. One can then infer from this measurement the single particle spectrum of the perturbed Fermi gas and observe the characteristic signs of the OC. This work has been published in Physical Review A **84** (6), 063632 (2011).

The behaviour of the overlap in many-body systems under the effect of both global and local perturbations of different forms is an intriguing area which has been previously un-explored. The sudden change of the trapping frequency on the state can lead to interesting results about the time evolving state of the system. One could then investigate how long it takes for the state to reach its time averaged state and if this is effected by the OC. Also it would be worth investigating does the time averaged state give a good description of the out-of-equilibrium dynamics of the system.

7.4 Effect of interparticle interaction in a free-oscillation atomic interferometer

The creation of superposition states was investigated using the free oscillation atom interferometer, which exploits the oscillatory motion of particles displaced in a harmonic trap. Atoms scatter repeatedly off a tunable barrier at the centre of the trap which acts as a beamsplitter. For the case of two atoms the system was solved using a combination of analytical solutions and the *discrete variable representation* method. The interaction strength between the two particles and the height of the barrier were tuned to find the optimal state for use in metrology, the so-called NOON state. The output states were assessed by calculating the quantum Fisher information (QFI) which is related to the variance of a measured interferometric phase. At the Heisenberg limit the QFI is maximum and this signifies the creation of a NOON state. For a large range of attractive interactions the NOON state was found to be created, however when the interactions were repulsive this parameter space was significantly reduced. The detection of NOON states was proposed by observing the interference fringes of the freely expanding state. The greater fringe visibility of the NOON state is noticable when compared to states with a lower QFI. This work has been published in Physical Review A **87**, 043630 (2013).

It is unclear if the situation in which both particles are initially located in an eigenstate of one half of a double well trap will lead to similar results. Subsequent tunneling into the other well will depend on the interaction strength and the height of the barrier separating both wells. It would then be interesting to study what effect the interaction has on the tunnelling and if NOON states can possibly be created also in this situation.

7.5 Long distance entanglement in a linear ion chain

In this Chapter the growth of entanglement mediated by a linear ion chain was introduced and the significant results discussed. The environment was engineered by a careful tuning of the trap aspect ratio, and the two impurity ions were coupled to it via a laser. By initially preparing the impurities in a squeezed state, entanglement can be generated between the transverse modes of the impurites. For small ion chains the engineered environment enhanced significantly the entanglement created between the impurities. For large chains a decoherence free subspace was found to exist if the frequencies of the impurities were tuned to coincide with the nodes of the bath's spectral function. This entangled steady state was observed at both short and large impurity distances using a variety of environmental settings. The system was also shown to be resilient against

temperature and should allow observation of bath mediated entanglement in modern experiments. This work has been published in Physical Review A **87**, 050304(R) (2013).

It would be interesting to study the phase transition in the ion chain as it goes from linear to zig-zag configuration. This occurs as the trap aspect ratio is decreased past some critical point. By calculating the entanglement or quantum discord between two ions of the chain the location of this critical point could be inferred.

Bibliography

[1] A. Einstein, Annalen der Physik **17** (6): 132148 (1905)

[2] M. Planck, Ann. Phys. **309** (3): 553-63 (1901)

[3] L. de Broglie, *Recherches sur la thorie des quanta* (1924)

[4] F. Serwane, G. Zürn, T. Lompe, T. T. Ottenstein, A. N. Wenz and S. Jochim, Science **332**, 6027 (2011)

[5] M. Greiner, O. Mandel, T. Esslinger, T.W. Hänsch and I. Bloch, Nature **415**, 39 (2002).

[6] I. Bloch, J. Dalibard and W. Zwerger, Rev. Mod. Phys. **80**, 885 (2008).

[7] M. Girardeau, J. Math. Phys. **1**, 516 (1960).

[8] B. Paredes, A. Widera, V. Murg, O. Mandel, S. Fölling, I. Cirac, G.V. Shlyapnikov, T.W. Hänsch and I. Bloch, Nature **429**, 277 (2004).

[9] A. Y. Cherny and J. Brand, Phys. Rev. A **73**, 023612 (2006)

[10] T. Kinoshita, T. Wenger and D.S. Weiss, Science **305**, 1125 (2004).

[11] W. Alt, D. Schrader, S. Kuhr, Martin Müller, V. Gomer, and D. Meschede, Phys. Rev. A **67**, 033403 (2003)

[12] N. Schlosser, G. Reymond, I. Protsenko and P. Grangier, Nature **411**, 1024–1027 (2001)

[13] J. Barrett, N. Linden, S. Massar, S. Pironio, S. Popescu, and D. Roberts, Phys. Rev. A **71**, 022101 (2005)

[14] C. H. Bennett, G. Brassard, C. Crépeau, R. Jozsa, A. Peres, and W. K. Wootters, Phys. Rev. Lett. **70**, 1895–1899 (1993)

[15] Y. I. Manin, Sov. Radio. 13–15, (1980)

[16] R. P. Feynman, *International Journal of Theoretical Physics*, **21**, (6), 467–488 (1982)

[17] D. Deutsch, *Proceedings of the Royal Society of London*, Series A, Mathematical and Physical Sciences **400** (1818), 97-117 (1985)

[18] W. Pauli, Phys. Rev. **58**, 716–722 (1940)

[19] E. Fermi, Rendiconti Lincei **3** 145-9 (1926)

[20] P. A. M. Dirac, Proceedings of the Royal Society, Series A **112**, 762, 66177 (1926)

[21] M. H. Anderson, J. R. Ensher, M. R. Matthews, C. E. Wieman, E. A. Cornell, Science **269** 5221. 198-201 (1995)

[22] K. B. Davis, M. O. Mewes, M. R. Andrews, N. J. van Druten, D. S. Durfee, D. M. Kurn, and W. Ketterle, Phys. Rev. Lett. **75**, 3969-3973 (1995)

[23] M. Ueda, *Fundamentals and New Frontiers of Bose-Einstein Condensation*, World Scientific (2010)

[24] M. R. Andrews, C. G. Townsend, H. J. Miesner, D. S. Durfee, D. M. Kurn, W. Ketterle, Science **275** 5300, 637–641 (1996)

[25] D. S. Jin, J. R. Ensher, M. R. Matthews, C. E. Wieman, and E. A. Cornell, Phys. Rev. Lett. **77**, 420423 (1996)

[26] M. R. Matthews, B. P. Anderson, P. C. Haljan, D. S. Hall, C. E. Wieman, and E. A. Cornell, Phys. Rev. Lett. **83**, 24982501 (1999)

[27] E. A. Donley, N. R. Claussen, S. L. Cornish, J. L. Roberts, E. A. Cornell and C. E. Wieman, Nature **412**, 295–299 (2001)

[28] C. Becker, S. Stellmer, P. Soltan–Panahi, S. Dörscher, M. Baumert, E. M. Richter, J. Kronjäger, K. Bongs and K. Sengstock, Nature Physics **4**, 496 – 501 (2008)

[29] Z. Dutton, N. S. Ginsberg, C. Slowe and L. Vestergaard Hau, Europhysics News **35** 2, 33 (2004)

[30] D. Jaksch, P. Zoller, Annals of Physics **315**, 1: 5279 (2005)

[31] R. Schmeid, T. Roscilde, V. Murg, D. Porras and J. I. Cirac, New J. Phys. **10** 045017 (2008)

[32] I. Buluta and F. Nori, Science **326**, 5949 (2009)

[33] P. W. Graham, J. M. Hogan, M. A. Kasevich, and S. Rajendran, Phys. Rev. Lett. **110**, 171102 (2013)

[34] Th. M. Nieuwenhuizen, EPL **83**, 10008 (2008)

[35] H. Friedrich, *Theoretical Atomic Physics* (Springer, (2003)).

[36] M. Fattori, G. Roati, B. Deissler, C. DErrico, M. Zaccanti, M. Jona–Lasinio, L. Santos, M. Inguscio, and G. Modugno, Phys. Rev. Lett. **101**, 190405 (2008).

[37] J. Stuhler, A. Griesmaier, T. Koch, M. Fattori, T. Pfau, S. Giovanazzi, P. Pedri, and L. Santos, Phys. Rev. Lett. **95**, 150406 (2005)

[38] C. Chin, R. Grimm, P. Julienne, Rev. Mod. Phys. **82**, 1225 (2010).

[39] O. Mandel, M. Greiner, A. Widera, T. Rom, T.W. Hänsch and I. Bloch, Phys. Rev. Lett. **91**, 010407 (2003)

[40] I. Bloch J. Phys. B: At. Mol. Opt. Phys. **38** S629 (2005)

[41] D. S. Petrov, G. V. Shlyapnikov, and J. T. M. Walraven, Phys. Rev. Lett. **85**, 37453749 (2000)

[42] D. M. Gangardt and G. V. Shlyapnikov, Phys. Rev. Lett. **90**, 010401 (2003)

[43] E. H. Lieb and W. Liniger, Phys. Rev. **130** 16051616 (1963)

[44] K. Huang and C. N. Yang, Phys. Rev. **105**, 767 (1957).

[45] M. Olshanii, Phys. Rev. Lett. **81**, 938 (1998).

[46] K. Günter, T. Stöferle, H. Moritz, M. Köhl, and T. Esslinger, Phys. Rev. Lett. **95**, 230401 (2005)

[47] H. Moritz, T. Stöferle, K. Günter, M. Köhl, and T. Esslinger, Phys. Rev. Lett. **94**, 210401 (2005)

[48] M.D. Girardeau, E.M. Wright, and J.M. Triscari, Phys. Rev. A **63**, 033601 (2001).

[49] G.J. Lapeyre, Jr., M.D. Girardeau, and E.M. Wright, Phys. Rev. A **66**, 023606 (2002).

[50] P. A. M. Dirac, *Proceedings of the Cambridge Philosophical Society*, **26** 376 (1930)

[51] F.G. Tricomi, *Integral Equations*, Wiley, New York, (1967)

[52] P.J. Forrester, N.E. Frankel, T.M. Garoni and N.S. Witte, Phys. Rev. A **67**, 043607 (2003)

[53] S. Bose, Phys. Rev. Lett. **91**, 207901 (2003)

[54] T. J. Osborne and M. A. Nielsen, Phys. Rev. A **66**, 032110 (2002)

[55] R. Raussendorf and H. J. Briegel, Phys. Rev. Lett. **86**, 51885191 (2001)

[56] S. Olmschenk, K. C. Younge, D. L. Moehring, D. N. Matsukevich, P. Maunz, and C. Monroe, Phys. Rev. A. **76**, 052314 (2007)

[57] B. B. Blinov, D. Leibfried, C. Monroe and D. J. Wineland, *Quantum Information Processing*, **3**, 15 (2004)

[58] M. D. Kim, D. Shin, and J. Hong, Phys. Rev. B **68**, 134513 (2003)

[59] P. J. Lee, M. Anderlini, B. L. Brown, J. Sebby–Strabley, W. D. Phillips, and J. V. Porto, Phys. Rev. Lett. **99**, 020402 (2007)

[60] J. Chan, T. P. M. Alegre, A. H. Safavi–Naeini, J. T. Hill, A. Krause, S. Gröblacher, M. Aspelmeyer, O. Painter, Nature **478**, 89 (2011)

[61] S. Gigan, H. R. Böhm, M. Paternosto, F. Blaser, G. Langer, J. B. Hertzberg, K. C. Schwab, D. Bauerle, M. Aspelmeyer, and A. Zeilinger, Nature **444**, 67 (2006).

[62] C. E. Shannon, *A Mathematical Theory of Communication*, Bell System Technical Journal **27** (3): 379423, (1948).

[63] J. von Neumann, *Mathematische Grundlagen der Quantenmechanik*, Berlin: Springer (1995)

[64] H. Mack and M. Freyberger, Phys. Rev. A **66**, 042113 (2002).

[65] M. Bußhardt and M. Freyberger, Phys. Rev. A **75**, 052101 (2007).

[66] B. Sun, D. Zhou and L. You, Phys. Rev. A. **73**, 012336 (2006).

[67] D. S. Murphy, J. F. McCann, J. Goold, and Th. Busch, Phys. Rev. A. **76**, 053616 (2007).

[68] M. A. Nielsen, and I. Chuang, *Quantum computation and quantum information*, Cambridge: Cambridge Univ. Press. (2001)

[69] R. F. Werner, Phys. Rev. A **40**, 42774281 (1989)

[70] J. Bell, Physics **1** (3), 195200 (1964).

[71] A. Einstein, B. Podolsky and N. Rosen, Physical Review **47** (10): 777780 (1935)

[72] J. F. Clauser, M.A. Horne, A. Shimony and R. A. Holt, Phys. Rev. Lett. **23**, 880–884 (1969)

[73] D. Bouwmeester, J. Pan, K. Mattle, M. Eibl, H. Weinfurter and A. Zeilinger, Nature **390**, 575–579 (1997)

[74] A. K. Ekert, Phys. Rev. Lett. **67**, 661663 (1991)

[75] A. Aspect, P. Grangier, and G. Roger, Phys. Rev. Lett. **47**, 460463 (1981)

[76] M. A. Rowe, D. Kielpinski, V. Meyer, C. A. Sackett, W. M. Itano, C. Monroe and D. J. Wineland, Nature **409**, 791–794 (2001)

[77] W. Tittel, J. Brendel, H. Zbinden, and N. Gisin, Phys. Rev. Lett. **81**, 35633566 (1998)

[78] B. Wittmann, S. Ramelow, F. Steinlechner, N. K. Langford, N. Brunner, H. M. Wiseman, R. Ursin and A. Zeilinger, New J. Phys. **14** 053030

[79] A. J. Bennet, D. A. Evans, D. J. Saunders, C. Branciard, E. G. Cavalcanti, H. M. Wiseman, and G. J. Pryde, Phys. Rev. X **2**, 031003 (2012)

[80] R. García–Patrón, J. Fiurcek, N. J. Cerf, J. Wenger, R. Tualle–Brouri, and Ph. Grangier, Phys. Rev. Lett. **93**, 130409 (2004)

[81] M. Krych and Z. Idziaszek, Phys. Rev. A **80**, 022710 (2009).

[82] J. Goold, M. Krych, T. Fogarty, Z. Idziaszek and Th. Busch, New J. Phys. **12** 093041 (2010).

[83] M. Abramowitz and I. Stegun, *eds.*, *Handbook of Mathematical Functions* (Dover, 1972).

[84] W. P. Schleich, *Quantum Optics in Phase Space*, Wiley–VCH (2001).

[85] E. P. Wigner, Phys. Rev **40**, 749 (1932).

[86] A. Kenfack and K. Życzkowski, J. Opt. B: Quantum Semiclass. Opt. **6**, 396 (2004).

[87] R. Horodecki, P. Horodecki, M. Horodecki and K. Horodecki, Rev. Mod. Phys. **81**, 865942 (2009)

[88] S. L. Braunstein and P. van Loock, Rev. Mod. Phys. **77**, 513 (2005).

[89] A. Royer, Phys. Rev. A **15**, 449 (1977).

[90] K. Banaszek and K. Wodkiewicz, Phys. Rev. A **58**, 4345 (1998); Phys. Rev. Lett. **82** 2009 (1999).

[91] L. Förster, M. Karski, J. M. Choi, A. Steffen, W. Alt, D. Meschede, A. Widera, E. Montano, J.H. Lee, W. Rakreungdet, and P. S. Jessen, Phys. Rev. Lett. **103**, 233001 (2009).

[92] L. G. Lutterbach and L. Davidovich, Phys. Rev. Lett. **78**, 2547 (1997).

[93] A. S. Parkins and E. Larsabal, Phys. Rev. A **63**, 012304 (2000); M. Paternostro, M. S. Kim, and P. L. Knight, Phys. Rev. A **71**, 022311 (2005).

[94] C. Monroe, D. M. Meekhof, B. E. King, and D. J. Wineland, Science **272**, 1131 (1996).

[95] D. Leibfried, R. Blatt, C. Monroe, and D. Wineland, Rev. Mod. Phys. **75**, 281 (2003).

[96] S. W. Lee, H. Jeong and D. Jaksch, Phys. Rev. A. **81**, 012302 (2010).

[97] M. Girardeau and A. Minguzzi, Phys. Rev. A **79**, 033610 (2009).

[98] C. Schenke, A. Minguzzi, F. W. J. Hekking, Phys. Rev. A **85**, 053627 (2012)

[99] S. Palzer, C. Zipkes, C. Sias and M. Köhl, Phys. Rev. Lett. **103**, 150601 (2009).

[100] Th. Busch and G. Huyet, J. Phys. B: At. Mol. Opt. **36**, 2553 (2003).

[101] H. Fu and A.G. Rojo, Phys. Rev. A **74**, 013620 (2006).

[102] J. Goold and Th. Busch, Phys. Rev. A **77**, 063601 (2008).

[103] J. Goold, D. O'Donoghue and Th. Busch, J. Phys. B: At. Mol. Opt. **41**, 215301 (2008).

[104] J. Goold, H. Doerk, Z. Idziaszek, T. Calarco and Th. Busch, Phys. Rev.A **81**, 041601 (2010).

[105] T. Kinoshita, T. Wenger and D.S. Weiss, Nature **440**, 900 (2006).

[106] H. Moritz, T. Stöferle, M. Köhl, and T. Esslinger, Phys. Rev. Lett. **91**, 250402 (2003).

[107] M. Olshanii, Phys. Rev. Lett. **81**, 938 (1998).

[108] M. Girardeau and E.M. Wright, Phys. Rev. Lett. **84**, 5239 (2000).

[109] J. Friedel, Nouvo Cimento **7**, 287 (1958).

[110] George E. Simion and Gabriele F. Giuliani, Phys. Rev. B **72**, 045127 (2005)

[111] T. R. Taha and M. J. Ablowitz, J. Comput. Phys. **55** (2): 203230 (1984)

[112] R.P. Feynman and A.R. Hibbs, *Quantum Mechanics and Path Integrals*, McGraw–Hill, New York, (1965)

[113] R. Pezer and H. Buljan, Phys. Rev. Lett. **98**, 240403 (2007).

[114] A. Minguzzi, D. M. Gangardt, Phys. Rev. Lett. **94**, 240404 (2005)

[115] X. Yin, Y. Hao, S. Chen, and Z. Zhang, Phys. Rev. A **78**, 013604 (2008).

[116] K. Lelas, D. Jukić and H. Buljan, Phys. Rev. A **80**, 053617 (2009).

[117] X. Lü, X. Yin and Y. Zhang, Phys. Rev. A **81**, 043607 (2010).

[118] C. Zipkes, L. Ratschbacher, C. Sias and M. Köhl, New J. Phys. **13** 053020 (2011)

[119] S. Schmid, A. Härter and J. H. Denschlag, Phys. Rev. Lett. **105**, 133202 (2010).

[120] A. Härter, A. Krükow, A. Brunner, and J. Hecker Denschlag, arXiv:1302.6157 (2013)

[121] L. H. Nguyen, A. Kalev, M.D. Barrett, and B.G. Englert, Phys. Rev. A **85**, 052718 (2012)

[122] A. Schirotzek, C.H. Wu, A. Sommer, and M.W. Zwierlein, Phys. Rev. Lett. **102**, 230402 (2009).

[123] S. Nascimbéne, N. Navon, K.J. Jiang, L. Tarruell, M. Teichmann, J. McKeever, F. Chevy, and C. Salomon, Phys. Rev. Lett. **103**, 170402 (2009).

[124] C. Weber, *et al.*, Phys. Rev. A **82**, 042722 (2010).

[125] S. Will, *et al.*, Phys. Rev. Lett. **106**,115305 (2011).

[126] C. Zipkes, S. Palzer, C. Sias and M. Köhl, Nature **464**, 388 (2010).

[127] P. W. Anderson, Phys. Rev. Lett. **18**, 1049 (1967).

[128] P. Nozières and C. T. De Dominicis, Phys. Rev. **178**, 1097 (1969).

[129] J. T. Grant, D. Briggs, *Surface Analysis by Auger and X–ray Photoelectron Spectroscopy*, Chichester: IM Publications, (2003)

[130] G.D. Mahan, *Many Particle Physics*, Springer, (2000).

[131] P. Zanardi and N. Paunković, Phys. Rev. E. **74**, 031123 (2006).

[132] F. M. Cucchietti, D. A. R. Dalvit, J. P. Paz, and W. H. Zurek, Phys. Rev. Lett. **91**, 210403 (2003).

[133] H. T. Quan, Z. Song, X. F. Liu, P. Zanardi, and C. P. Sun, Phys. Rev. Lett. **96**, 140604 (2006).

[134] D. L. Shepelyansky, Physica D, **8**, p. 208 (1983).

[135] F. M. Cucchietti, H. M. Pastawski, and R. A. Jalabert, Phys. Rev. B, **70**, p. 035311 (2004).

[136] N. Ares and D. A. Wisniacki, Phys. Rev. E, **80**, p. 046216 (2009).

[137] Th. Busch, B. G. Englert, K Rzazewski and M Wilkens, Found. Phys. **28** 549 (1998)

[138] Th. Busch and G. Huyet, J. Phys. B: At. Mol. Opt. **36** 2553 (2003) ; J. Goold, D. O'Donoghue and Th. Busch, J. Phys. B: At. Mol. Opt. **41** 215301 (2008).

[139] M. Bruderer and D. Jaksch, New J. Phys. **8**, 87 (2006).

[140] A. Recati, *et al.*, Phys. Rev. Lett. **94**, 040404 (2005).

[141] S. Campbell, M. Paternostro, S. Bose, and M. S. Kim, Phys. Rev. A **81**, 050301(R) (2010).

[142] G. De Chiara, T. Calarco, S. Fishman, and G. Morigi, Phys. Rev. A. **78**, 043414 (2008).

[143] J. Catani, *et al.*, arXiv:1106.0828 (2011).

[144] K. Lelas, T. Ševa and H. Buljan, arXiv:1104.2675, (2011).

[145] M. W. Mitchell, J. S. Lundeen and A.M. Steinberg, Nature **429**, 161–164 (2004).

[146] P. Walther et al, Nature **429**, 158–161 (2004).

[147] J. G. Rarity et al, Phys. Rev. Lett. **65**, 1348 (1990).

[148] I. Afek, O. Ambar and Y. Silberberg, Science **328**, 879 (2010).

[149] Y. J. Wang, D. Z. Anderson, V. M. Bright, E. A. Cornell, Q. Diot, T. Kishimoto, M. Prentiss, R. A. Saravanan, S. R. Segal, and S. Wu, Phys. Rev. Lett. **94**, 090405 (2005).

[150] J. J. Cooper, D. W. Hallwood, J. A. Dunningham and J. Brand, Phys. Rev. Lett. **108** 130402 (2012); J. A. Dunningham, J. J. Cooper and D. W. Hallwood, arXiv:1102.0164, To Appear AIP Proceedings (2012).

[151] C. Schenke, A. Minguzzi, F. W. J. Hekking, Phys. Rev. A **84**, 053636 (2011)

[152] F. Baumgärtner, R. J. Sewell, S. Eriksson, I. Llorente–Garcia, J. Dingjan, J. P. Cotter, and E. A. Hinds, Phys. Rev. Lett. **105**, 243003 (2010).

[153] Y. Shin, M. Saba, T. A. Pasquini, W. Ketterle, D. E. Pritchard, and A. E. Leanhardt, Phys. Rev. Lett. **92**, 050405 (2004).

[154] B. Gertjerenken, T. P. Billam, L. Khaykovich, and C. Weiss, arXiv:1208.2941v2

[155] J. L. Helm, T. P. Billam, and S. A. Gardiner, Phys. Rev. A. **85** 053621 (2012)

[156] C. Weiss and Y. Castin, Phys. Rev. Lett. **102** 010403 (2009)

[157] A. I. Streltsov, O. E. Alon, and L. S. Cederbaum, Phys. Rev. A. **80** 043616 (2009)

[158] R. H. Leonard and C. A. Sackett, Phys. Rev. A. **86** 043613 (2012).

[159] M. Horikoshi and K. Nakagawa, Phys. Rev. Lett. **99** 180401 (2007).

[160] R. P. Kafle, D. Z. Anderson and A. A. Zozulya, Phys. Rev. A. **84**, 033639 (2011).

[161] A.D. Martin and J. Ruostekoski, New J. Phys. **14** 043040 (2012)

[162] S. L. Braunstein and C. M. Caves, Phys. Rev. Lett. **72**, 3439 (1994).

[163] U. Dorner, R. Demkowicz–Dobrzanski, B. J. Smith, J. S. Lundeen, W. Wasilewski, K. Banaszek, I. A. Walmsley, Phys. Rev. Lett. **102** 040403 (2009)

[164] D. S. Murphy, J. F. McCann, J. Goold, and Th. Busch, Phys. Rev. A. **76**, 053616 (2007)

[165] M. Olshanii, Phys. Rev. Lett. **81** 938 (1998)

[166] C. Chin, R. Grimm and P. Julienne, Rev. Mod. Phys. **82** 1225 (2010)

[167] D. Baye and P.–H. Heenen, J. Phys. A: Math. Gen. **19**, 2041 (1986).

[168] J. Light and J. T. Carrington, Adv. Chem. Phys. **114**, 263 (2000).

[169] J. Goold, Libby Heaney, Th. Busch, and V. Vedral, Phys. Rev. A **80**, 022338 (2009)

[170] T. Lahaye, C. Menotti, L. Santos, M. Lewenstein and T. Pfau, Rep. Prog. Phys. **72**, 126401 (2009).

[171] M. Ludwig, K. Hammerer, and F. Marquardt, Phys. Rev. A **82**, 012333 (2010).

[172] J. Koch, A. A. Houck, K. L. Hur, S. M. Girvin, Phys. Rev. A **82**, 043811 (2010).

[173] S. Diehl, A. Micheli, A. Kantian, B. Kraus, H. P. Büchler, and P. Zoller, Nat. Phys. **4**, 878 (2008).

[174] F. Verstraete, M. M. Wolf, and J. I. Cirac, Nat. Phys. **5**, 633 (2009).

[175] S. Pielawa, L. Davidovich, D. Vitali, and G. Morigi, Phys. Rev. A **81**, 043802 (2010).

[176] C. A. Muschik, E. S. Polzik, and J. I. Cirac, Phys. Rev. A **83**, 052312 (2011).

[177] H. Krauter, C. A. Muschik, K. Jensen, W. Wasilewski, J. M. Petersen, J. I. Cirac, and E. S. Polzik, Phys. Rev. Lett. **107**, 080503 (2011).

[178] J. T. Barreiro, M. Mller, P. Schindler, D. Nigg, T. Monz, M. Chwalla, M. Hennrich, C. F. Roos, P. Zoller, R. Blatt, Nature **470**, 486 (2011).

[179] K. G. H. Vollbrecht, C. A. Muschik, and J. I. Cirac, Phys. Rev. Lett. **107**, 120502 (2011).

[180] G. Goldstein, P. Cappellaro, J. R. Maze, J. S. Hodges, L. Jiang, A. S. Sørensen, and M. D. Lukin, Phys. Rev. Lett. **106**, 140502 (2011).

[181] D. Braun, Phys. Rev. Lett. **89**, 277901 (2002)

[182] J. P. Paz and A. J. Roncaglia, Phys. Rev. Lett. **100**, 220401 (2008)

[183] J. Anders, Phys. Rev. A **77**, 062102 (2008).

[184] T. Zell, F. Queisser, and R. Klesse, Phys. Rev. Lett. **102**, 160501 (2009).

[185] M. B. Plenio, J. Hartley and J. Eisert, New J. Phys. **6** 36 (2004)

[186] A. Wolf, G. De Chiara, E. Kajari, E. Lutz, and G. Morigi, Europhys. Lett. **95**, 60008 (2011).

[187] E. Kajari, A. Wolf, E. Lutz, and G. Morigi, Phys. Rev. A **85**, 042318 (2012).

[188] K. Hayasaka, Appl. Phys. B **107**, 965 (2012).

[189] M. J. Raizon et al., Phys. Rev. A **45**, 6493 (1992).

[190] T. P. Meyrath and D. F.V. James, Phys. Lett. A **240** (1998) 37–42.

[191] D. H. E. Dubin, Phys. Rev. E **55**, 4017 (1997).

[192] G.-D. Lin, S.-L. Zhu, R. Islam, K. Kim, M.-S. Chang, S. Korenblit, C. Monroe and L.-M. Duan, EPL **86** 60004 (2009).

[193] D. Kielpinski, B. E. King, C. J. Myatt, C. A. Sackett, Q. A. Turchette, W. M. Itano, C. Monroe, D. J. Wineland, and W. H. Zurek, Phys. Rev. A **61**, 032310 (2000), and references therein.

[194] S. L. Braunstein, Phys. Rev. A **71**, 055801 (2005).

[195] G. Adesso, I. Fuentes–Schuller and M. Ericsson, Phys. Rev. A. **76**, 062112 (2007)

[196] G. Vidal and R. F. Werner, Phys. Rev. A **65**, 032314 (2002).

[197] M. B. Plenio, Phys. Rev. Lett. **95**, 090503 (2005).

[198] D. Leibfried, R. Blatt, C. Monroe, and D. Wineland, Rev. Mod. Phys. **75**, 281 (2003). D. J. Wineland, C. Monroe, W. M. Itano, D. Leibfried, B. E. King, and D. M. Mekhof, J. Res. Natl. Inst. Stand. Technol. **103**, 259 (1998)

[199] G. W. Ford, M. Kac and P. Mazur, J. Math. Phys. **6**, 504 (1965).

[200] F. Splatt, M. Harlander, M. Brownnutt, F Zähringer, R. Blatt and W Hänsel, New J. Phys. **11** 103008 (2009)